Novel Absorber Engineering Techniques to Enhance the Efficiency of Perovskite Solar Cells

Thesis submitted in partial fulfillment of the requirements for the award of the degree of

Doctor of Philosophy

by

J Lakshmi Prasanna

(Regd. No. 720062)

Under the Supervision of

Dr. Ekta Goel

Assistant Professor, Dept. of ECE

&

Dr. Amarjit Kumar

Assistant Professor, Dept. of ECE

Department of Electronics & Communication Engineering

NATIONAL INSTITUTE OF TECHNOLOGY WARANGAL – 506004, T.S, INDIA

July-2024

Approval Sheet

This Thesis entitled Novel Absorber Engineering Techniques to Enhance the Efficiency of Perovskite Solar Cells

by

(J. Lakshmi Prasanna)

is approved for thedegree of Doctor of Philosophy

Examiners

_____

_____

_____

Supervisor (s)

Dr. Ekta Goel

&

Dr. Amarjit Kumar

Chairman

Dr. Vakula

Date:

DECLARATION

This is to certify that the work presented in the thesis entitled "Novel Absorber Engineering Techniques to Enhance the Efficiency of Perovskite Solar Cells" is a bonafide work done by J. Lakshmi Prasanna under the supervision of Dr. Ekta Goel & Dr. Amarjit Kumar and was not submitted elsewhere for the award of any degree.

I declare that the content presented in this written submission reflects my own thoughts expressed in my own language. In instances where I have incorporated the ideas or words of others, I have diligently provided proper citations and references to acknowledge the original sources. Additionally, I confirm my commitment to upholding the principles of academic honesty and integrity throughout this work. I have not misrepresented, falsified, or fabricated any information, including ideas, data, facts, or sources. I acknowledge that any violation of these principles may lead to disciplinary measures by the Institute and could also result in penalties from sources that were not appropriately cited or for which proper permission was not obtained when required.

J. Lakshmi Prasanna

720062

Date: _____

ACKNOWLEDGEMENT

*First and foremost, I want to dedicate my honest prayer to **lord Karthikeyan** who has given me the strength, knowledge, ability and opportunity to undertake this research study and to complete it satisfactorily. I am humbled and exceedingly joyful as a witness to his countless blessings.*

*Initially, I would like to express my immense gratitude and sincere thanks to my supervisor **Dr. Ekta Goel,** Assistant Professor and Co-supervisor **Dr. Amarjit Kumar,** Assistant Professor for their continuous support, motivation and valuable guidance. Their immense knowledge and guidance helped me a lot to carry out my research work. Without their precious and wholehearted support, the successful completion of this research work would not have been possible. The insightful discussions with them always provided me with great enthusiasm.*

*I extend heartfelt thanks to **Prof. D. Vakula**, the Head of the Department, Electronics and Communication Engineering for her invaluable guidance and unwavering commitment to academic excellence throughout my research and thesis completion. Her insightful feedback, encouragement, initiation and leadership greatly enriched my learning experience, influencing the direction of my work. I am profoundly grateful for her efforts in creating an intellectually stimulating environment, motivating me to pursue excellence in this academic endeavor.*

*I extend sincere thanks to former HOD **Prof. P. Sreehari Rao** for fostering an environment of academic excellence during his tenure as the Head of the Department. His leadership and guidance had a profound impact on the quality of my research. I also acknowledge **Prof. Anjaneyulu L**, former HOD for his valuable contributions, mentorship, and dedication to academic growth. I am truly grateful for their impactful influence.*

*I wish to extend my sincere gratitude to my Doctoral scrutiny Committee (DSC) members **Prof. P. Sreehari Rao,** Professor**, Prof. V Narendar,** Assistant Professor and Prof. Palash Mishra, Assistant Professor, Dept. of EED for their valuable suggestions and fruitful discussions during the entire period of my research and for providing me with all the necessary suggestions.*

*I would also like to thank all the faculty members, laboratory staff, librarians and office staff for their kind cooperation and encouragement during this journey. My thanks and deep appreciations also go to all staff members of the Department of Electronics and communication Engineering for their kind co-operation. I would like to express my special thanks to my co scholar **Mr. Murali**, for his constant encouragement and timely help.*

*I have great pleasure in acknowledging my colleague **Dr. Atul Kumar**, Assistant Professor, ECE, KLEF for this motivation, support, and encouragement. I wish to extend my special thanks for providing a nice, friendly and peaceful research environment.*

*I would like to express my heart-felt gratitude to my beloved parents **Shri. J Gurunadh and Smt. Geetha** for their constant support and love throughout my life. I am always indebted to my fiancé **P. Kumar** for his consistent support. My most profound appreciation towards my sister **Mrs. Rani** Prasanna and my brother-in-law **Mr. Prasad** for their continuous support and encouragement.*

*At this special moment, where mere words seem inadequate, I extend my heartfelt gratitude to a cherished well-wisher, a trusted friend, an invaluable mentor, and a steadfast supporter and my Guru—**Dr. Rauri Santhosh**. His unwavering presence and consistent support have been the pillars behind me, standing strong at every crucial juncture. My deepest thanks to him for being the guiding force that has propelled me forward.*

Date: ***(J Lakshmi Prasanna)***

DEDICATED TO Dr. RAURI SANTHOSH

Table of Contents

List of Figures

List of Tables

Abstract

In recent years, perovskite solar cells have emerged as a promising technology in the field of photovoltaics. However, their efficiency is hindered by various factors that necessitate a comprehensive investigation. This research focuses on absorber engineering, bandgap grading optimization, and the application of machine learning algorithm. By doing so, this study aims to significantly contribute to the advancement of perovskite solar cell technology. This comprehensive thesis undertakes a multifaceted exploration of perovskite solar cells (PSCs), to address crucial challenges and enhance efficiency. The initial investigation reveals performance-limiting parameters in contemporary PSCs, emphasizing deficits in fill factor (FF) and open-circuit voltage (V_{OC}). Absorber characteristics and device optimizations, such as carrier concentration control and shunt resistance considerations, result in a significantly improved device with enhanced V_{OC}, FF, and power conversion efficiency (PCE).

A subsequent theoretical study focuses on configurational optimization of heterojunction PSCs to minimize internal recombination, employing various design alterations. The optimized device exhibits noteworthy enhancements in PCE, FF, and V_{OC} compared to benchmark configurations. Moving forward, a proposed bandgap grading profile seeks to maximize spectrum absorption in perovskite absorber material, targeting the Shockley-Queisser (SQ) limit. Analyzing linear bandgap grading profiles, the research identifies an optimal range for efficiency, emphasizing a well-optimized small bandgap grading range to achieve 31% power conversion efficiency. Continuing the exploration, a novel double absorber layer structure is introduced, incorporating 12 different absorber layer combinations. This approach expands spectral absorption, mitigates thermalization losses, and achieves an impressive efficiency exceeding 35%. To deepen insights, a dataset of 3490 samples characterizing perovskite structures is generated. Leveraging machine learning with the Random Forest algorithm, a predictive model classifies structures and offers valuable insights into optimized PSC design.

Overall, this thesis contributes significantly to the advancement of PSC technology, offering novel solutions, theoretical insights, and practical design guidelines. The findings promise higher PCE and improved overall performance, propelling PSCs toward their potential as a leading photovoltaic technology in the renewable energy landscape.

CHAPTER 1

INTRODUCTION

1.1 Background

Global warming due to fossil fuel consumption is one of the alarming issues which cannot be ignored or refuted. As of the year 2020, temperatures around the globe are soaring above 40°C in several regions, leading to severe heat waves and their associated health risks [1]. The Asian countries have witnessed an increase in extreme weather events, including intense rainfall, cyclones, and flooding in various parts. These changes in weather patterns align with the established scientific consensus that attributes such events to climate change, which is exacerbated by human activities and their impact on the environment [2]. It is crucial to address these issues through sustainable practices and mitigation strategies to safeguard the well-being of global population and its ecosystems.

National Geographic estimates the usage of 320 billion kWh of energy every day, most of which is supplied by the burning of fossil fuels [3]. According to the International Energy Agency (IEA), as of 2020, fossil fuels account for approximately 80% of global energy consumption. This includes supplying around 65% of global electricity generation [4]. They have long been identified as the primary contributor to climate change. While the sun's impact on a polluted atmosphere can be detrimental to a "greenhouse" Earth, it also holds the key to liberating ourselves from fossil fuel dependence. In recent decades, significant progress has been made in the development of novel types of new and renewable energies. These include wind energy, solar energy, nuclear energy, and geothermal energy [5].

Solar energy is a preferred alternative due to its sustainability, independence from geological factors, and low-cost maintenance, making it a safer and more viable option. This vast reservoir of solar energy available on earth surpasses all other finite and renewable resources [6-8]. However, solar irradiance is not always uniformly available globally. It depends on factors such as the time of day, local weather conditions, and seasonal variations. Yet, when combined with other renewable energy sources, it paves way for advancements in energy storage technologies, which includes solar modules [9, 10]. These solar modules have the capacity to contribute significantly to societal energy needs as a wide range of photovoltaic (PV) devices. Silicon solar cells, the most widely used solar energy harvester, dominate the PV market due to their

high power conversion efficiency (PCE) of approximately 26% for commercial silicon solar cells, extended operating lifespan of up to 25 years, and low maintenance requirements [11].

1.2 Evolution of photovoltaic devices

The evolution of photovoltaic devices in terms of generation has been marked by significant advancements and milestones that have shaped the industry. This progress can be traced through various generations of solar cell technologies. Fig. 1.1 depicts the evolution of photovoltaic devices across different generations from 1970 till 2020.

The first-generation photovoltaic devices were based on crystalline silicon (c-Si) technology, which remains the dominant solar cell technology today. These devices have seen continuous improvements in efficiency and manufacturing processes over the years. Initial breakthroughs in c-Si technology include the development of the first practical solar cell by Bell Labs in 1954 [12]. Subsequent advancements in c-Si solar cells involved the use of p-n junctions and anti-reflective coatings, resulting in increased efficiency and performance [13]. The efficiency of first-generation c-Si solar cells has steadily improved, with the current record exceeding 26%[14]. Research efforts have also focused on reducing the costs associated with c-Si solar cells, making them more economically viable for large-scale deployment [15].

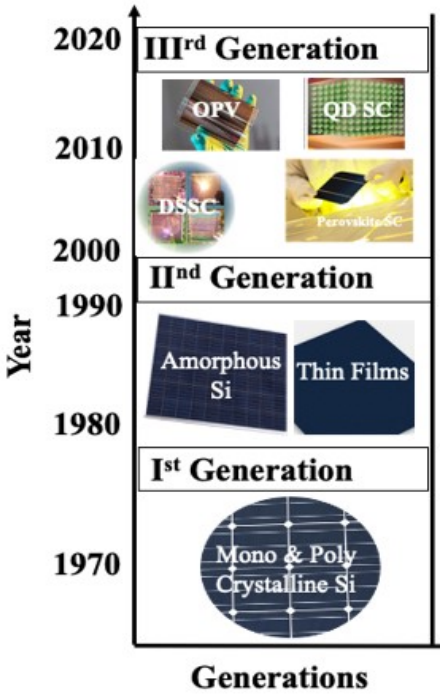

Figure 1.1 Timeline for PV generations with various photovoltaic devices. The timeline highlights the evolution from first-generation silicon solar cells to third-generation and emerging technologies, emphasizing key milestones and advancements in photovoltaic devices over the years.

Second-generation photovoltaic devices encompass thin-film solar cell technologies, including amorphous silicon (a-Si), copper indium gallium selenide (CIGS) cells and cadmium telluride (CdTe). Thin-film solar cells offer advantages such as lower production costs, flexibility, and potential for high-throughput manufacturing [16]. Amorphous silicon solar cells were among the first successful thin-film technologies, with commercial production starting in the 1980s [17]. CdTe solar cells gained prominence due to their superior efficiency and minimal manufacturing costs. They have become a major player in utility-scale installations [18]. CIGS solar cells have also shown promising efficiency levels and have benefited from advancements in deposition techniques[19]. The second generation of solar cells has contributed to the diversification of photovoltaic technologies and expanded the range of applications.

Third-generation photovoltaic devices focus on advanced concepts and materials beyond traditional silicon-based technologies. These include emerging technologies like perovskite solar cells, quantum dot solar cells and organic solar cells. Perovskite solar cells have procured significant attention for their high efficiency potential, rapid progress, and low-cost fabrication processes [14]. Organic solar cells, based on organic semiconductors, offer advantages such as lightweight, flexibility, and potential for low-cost manufacturing [20]. Quantum dot solar cells utilize nanoscale semiconductor particles to enhance light absorption and charge transport, showing promise for high-efficiency devices [21]. The third generation represents a frontier of research and development in photovoltaics, with ongoing efforts to overcome stability, scalability, and commercialization challenges.

Apart from the aforementioned generations, photovoltaic devices also explore advanced concepts and materials such as multi-junction solar cells, tandem solar cells, and advanced nanomaterials. Multi-junction solar cells, composed of multiple semiconductor layers, enable higher efficiency by capturing a broader spectrum of sunlight [22]. Tandem solar cells combine different materials with complementary absorption properties, aiming to achieve even higher efficiency levels [23]. Advanced nanomaterials, such as perovskite nanocrystals and carbon nanotubes, offer new avenues for improving performance and device architectures [24]. These photovoltaic devices focus on pushing the limits of efficiency, exploring novel materials, and integrating technologies like energy storage and smart grids.

The efficiency improvement of different generations of solar cells is depicted in Fig. 1.2. Monocrystalline silicon solar cells are the most common type of solar cells with high efficiencies typically ranging from 15 to 25% [25]. These cells are made from single-crystal

silicon wafers. Polycrystalline silicon solar cells made from multiple silicon crystals have slightly lower efficiencies compared to monocrystalline cells, typically ranging from 13 to 20% [26]. Thin-film solar cells are made from various materials, including amorphous silicon (a-Si), cadmium telluride (CdTe), and copper indium gallium selenide (CIGS). Their efficiencies range from around 10 to 22% depending on the specific material [27]. Multi-junction solar cells are composed of multiple layers of different semiconductor materials to capture a broader range of the solar spectrum. They are primarily used in concentrator photovoltaics (CPV) and have achieved record efficiencies exceeding 46% [28].

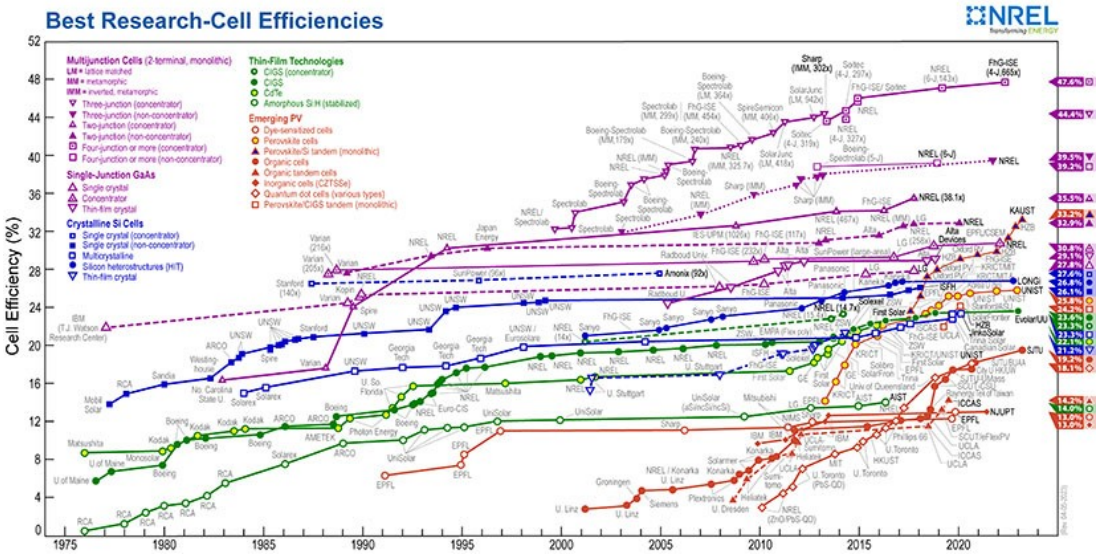

Figure 1.2 Best research-cell efficiencies of various solar cells depicting the peak efficiencies reached by different solar cell technologies, highlighting improvements and breakthroughs in research-cell performance [14].

Organic solar cells are based on organic molecules or polymers that can absorb sunlight and convert it into electricity. They have achieved efficiencies up to around 18% and offer potential for low-cost and flexible applications [29]. Quantum dot solar cells utilize quantum dots, nanoscale semiconductor particles, to capture and convert sunlight. Their efficiencies range from 8 to 13% but are actively being researched for further improvements [30, 31]. Perovskite solar cells are a rapidly emerging technology with great potential. They are made from hybrid organic-inorganic perovskite materials and have achieved efficiencies exceeding 25%. Ongoing research aims to further improve their stability and scalability [14].

However, perovskite solar cells (PSCs) are currently gaining momentum in the PV market as they possess unique properties. These include tunable bandgaps ranging from 1.35 to 2.3 eV [32], a high absorption coefficient (1.5×10^4 cm^{-1} at 550 nm for methylammonium lead iodide ($MAPbI_3$) compared to 6×10^3 cm^{-1} for crystalline silicon) [33, 34], high carrier mobility

ranging from 2 to 66 $cm^2 V^{-1} s^{-1}$ (compared to $10^{-5} \sim 10^{-4} V^{-1} s^{-1}$ for organic materials) [35, 36], and a long carrier diffusion length reaching up to 10 μm (compared to approximately 200 nm for organic semiconductors) [37, 38]. Importantly, the low-temperature fabrication processes (~100 °C) of PSCs make them suitable for a wide variety of applications.

1.3 Perovskite solar cell

Perovskite solar cells represent a novel and highly promising class of emerging photovoltaic technologies that have evolved from conventional, dye-sensitized solar cells (DSSCs) and quantum dot-sensitized solar cells (QDSSCs) [24, 35, 39-42]. PSCs have shown remarkable improvements in power conversion efficiency, reaching levels that rival traditional silicon-based solar cells as depicted in Fig 1.3. Early-stage perovskite solar cells achieved relatively low efficiencies, but through continuous research and development, PCEs above 25% have been achieved in the laboratory [43, 44]. Researchers have employed various strategies, including composition engineering, interface optimization, and device architecture design, to enhance the efficiency of perovskite solar cells [44].

Stability has been a critical challenge for PSCs, as they are sensitive to moisture, heat, and light. However, significant progress has been made in stabilizing perovskite materials and improving the long-term performance of devices. Encapsulation techniques, interface engineering, and materials engineering approaches have shown promise in enhancing the stability and reliability of perovskite solar cells [45-47]. Scalability is a crucial aspect for the practical implementation of perovskite solar cells. Researchers are actively exploring large-area deposition techniques, roll-to-roll manufacturing processes, and printing methods to enable cost-effective and scalable fabrication of PSCs. These efforts aim to transition PSCs from the laboratory to commercial-scale production [48].

1.3.1 Structure of Perovskite Material

Perovskite, derived from the mineral form $CaTiO_3$, defines a class of compounds with an ABX_3 stoichiometry, where A and B are cations and X represents an anion. Within the ABX_3 crystal structure, each unit cell consists of BX_6 octahedra sharing corners, while the A component occupies the cube octahedral cavity. In solar cells, perovskites used as absorber materials are commonly referred to as "hybrid" due to their organic and inorganic composition. Hybrid perovskites feature a monovalent organic cation (e.g. $CH_3NH_3^+$ or $(NH_2)_2)CH^+)$) as the A moiety, a divalent cation (Pb^{2+}, Sn^{2+}) from group IV as the B component, and a halide anion

(such as Cl^-, Br^-, I^-) denoted as X. Fig 1.3 illustrates the crystal structure of $CH_3NH_3PbX_3$ perovskites [49].

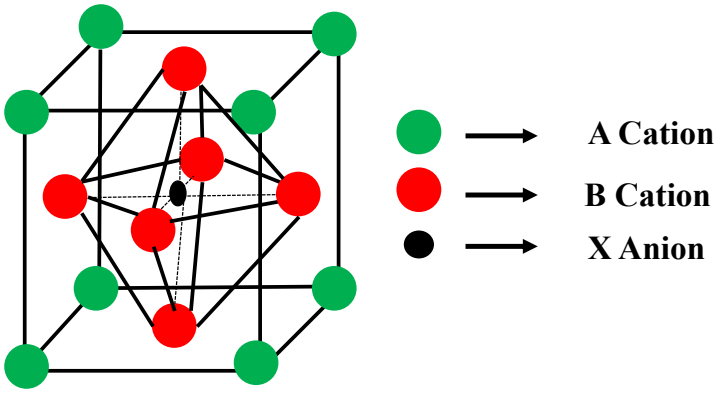

Figure 1.3 Basic structure of perovskite material depicting the crystal structure ABX_3 where "A" represents large cation, "B" represents metal cation and X represents halide anion.

Recently, there has been growing interest in mixed composition perovskites, where alternative elements or molecules of similar size partially or completely substitute the A, B, and/or X-sites [50, 51]. However, methylammonium lead iodide ($CH_3NH_3PbI_3$) or MAPI remains the most extensively studied hybrid perovskite for solar cell applications.

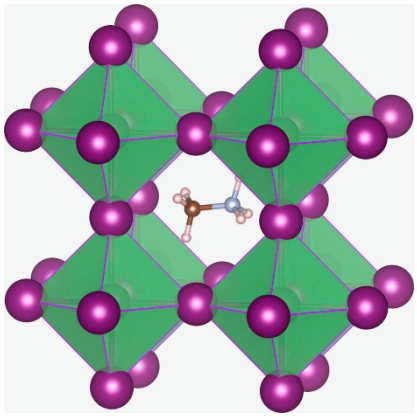

Figure 1.4 Basic crystal structure of methylammonium lead iodide $MAPbI_3$ Perovskite with methylammonium (MA) cations at the A sites, lead (Pb) cations at the B sites, and iodide (I) anions at the X sites, forming a three-dimensional network.

The $MAPbI_3$ perovskite material has a crystal structure that follows the perovskite arrangement as depicted in Fig. 1.4. It consists of a three-dimensional network of corner-sharing PbI_6 octahedra. In this structure, the lead (Pb) cations are surrounded by six iodine (I) anions, forming octahedral coordination. The methylammonium (MA) organic cations are located in the cuboctahedral cavity created by the arrangement of the PbI_6 octahedra. The methylammonium cations are positioned in a staggered configuration, allowing them to occupy the voids between the PbI_6 octahedra. Within this inorganic framework, the methylammonium

(MA) organic cations are situated. The MA cations are positioned in the cuboctahedral cavities formed by the arrangement of the PbI_6 octahedra [52, 53]. The organic cations have a staggered configuration, which allows them to occupy the voids between the inorganic octahedra. The presence of organic cations within the perovskite structure contributes to its hybrid nature. This organic-inorganic interaction plays a vital role in stabilizing the crystal lattice and influencing the optoelectronic properties of the material. Organic cations contribute to the absorption of light and the formation of excitons, which are essential for the efficient conversion of light into electrical energy.

The alternating layers of inorganic PbI_6 octahedra and organic MA cations create a well-ordered and periodic structure in $MAPbI_3$ perovskite. This structure is crucial for maintaining the stability and efficiency of the material as a solar cell absorber. The specific arrangement of the inorganic and organic components in the crystal lattice determines the electronic band structure and the ability of the perovskite to efficiently capture and convert photons into electrical charges. Organic cations contribute to the hybrid nature of the perovskite, as they are interspersed within the inorganic framework. The organic-inorganic interaction plays a crucial role in stabilizing the structure and influencing the optoelectronic properties of the perovskite material[54, 55].

The structure of $MAPbI_3$ perovskite consists of alternating layers of inorganic PbI_6 octahedra and organic methylammonium cations, forming a stable and well-defined crystal lattice. This unique structure contributes to the exceptional photovoltaic properties exhibited by $MAPbI_3$ perovskite, making it a promising material for solar cell applications.

1.3.2 Working principle of perovskite solar cell

PSCs have a fundamental structure that involves a light-harvesting perovskite layer positioned between electron and hole selective layers. Early-stage PSCs typically follow the n-i-p structure, which includes a substrate, cathode, electron transport layer (ETL), perovskite photoactive layer, hole transport layer (HTL), and anode. This n-i-p structure is commonly referred to as the normal, conventional, or regular structure in the field of PSCs. Significant progress has been made in the development of n-i-p structured devices, especially when based on mesoscopic structures [56].

Conventional n-i-p planar structures have been extensively studied, starting from dye-sensitized solar cells that utilize mesoscopic TiO_2 as the ETL and spiro-OMeTAD as the HTL [57, 58]. Unlike mesoporous materials, the n-i-p planar structure primarily employs inorganic

materials such as compact TiO_2, SnO_2, or ZnO as the ETL, and organic materials like Spiro-OMeTAD and PTAA as the HTL [59-62]. The p-i-n planar structured PSCs have emerged from organic solar cells and make use of traditional organic HTL materials like PEDOT:PSS, as well as fullerene derivative ETL materials such as PCBM and C_{60} [63, 64]. Furthermore, inorganic semiconductor materials such as NiO, CuO, VOx, MoOx have been employed as HTL, and TiOx, SnO_2 as ETL charge transport layers [65].

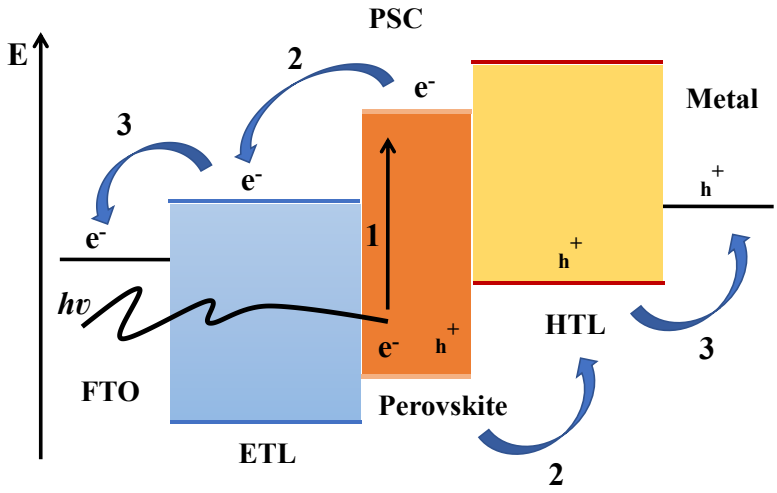

Figure 1.5 Operational mechanism of PSCs: (1) Light absorption. (2) generation of electrons and holes. (3) charge transport and collection [66].

Perovskite solar cells (PSCs) operate based on a working mechanism similar to general solar cells, involving several photovoltaic processes as depicted in Fig.1.5. These processes include the harvesting of light energy, the generation of free electrons and holes, the transport of charges through drift and diffusion, and the collection of charges as depicted in Fig 1.5 [66]. To ensure the efficiency of these working processes, the device structure has evolved from the initial PSCs that were inspired by the architecture of dye-sensitized solar cells, which achieved a modest power conversion efficiency (PCE) of 3.8% in 2009 [39].

While various materials have been investigated [67], the most successful and extensively studied configuration, as illustrated in Fig 1.6 (a), includes a titanium dioxide (TiO_2) layer grown on a fluorine-doped tin oxide (FTO)/glass substrate. The TiO_2 layer often serves as a mesoporous scaffold atop a compact layer. Following this, the perovskite layer, commonly known as methylammonium lead iodide ($CH_3NH_3PbI_3$ or $MAPbI_3$), is deposited, followed by the 2,2′(7,7′)-tetrakis-(N,N-di-p-methoxyphenyl-amine)9,9′-spirobifluorene (spiro-OMeTAD) layer. Metallic electrodes, frequently made of gold to enhance load (R_{Load}) connectivity, have been utilized, although alternative nonprecious metals have been explored as well [68].

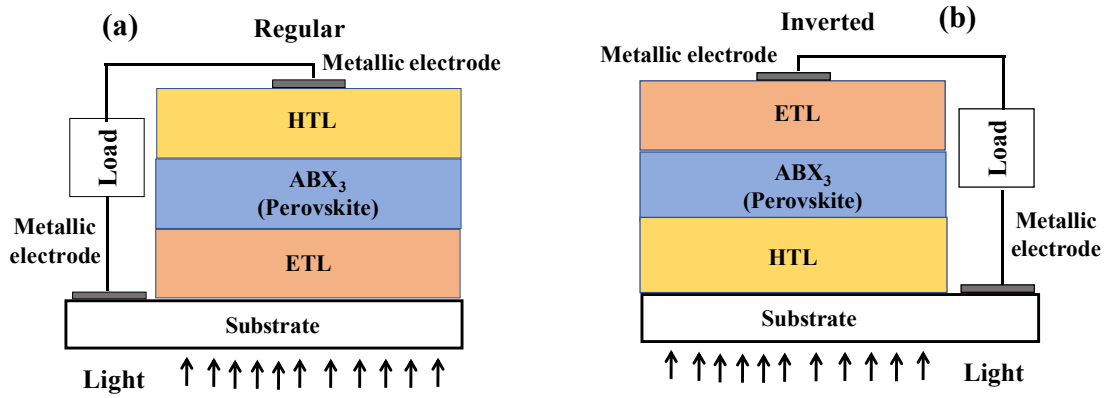

Figure 1.6 Basic structure of perovskite solar cell in a) regular and b) inverted configurations.

In this "regular" structure as depicted in Fug. 1.6 (a), incident light passes through the glass and transparent conducting oxide (TCO) substrate, traverses the electron-transport layer (ETL) before being absorbed by the perovskite layer, ultimately reaching the hole-transport layer (HTL) at the end of its optical pathway. This sequential arrangement ensures efficient light absorption and enables the generation of electron-hole pairs within the perovskite material. These charge carriers then migrate towards their respective selective contacts, the ETL and HTL. Subsequently, the extracted electrons and holes contribute to the generation of electrical power in the external circuit Ultimately, the electrons and holes are collected at their respective contacts, releasing their energy into an external circuit for utilization. This design allows for efficient photon absorption, charge separation, and charge collection, leading to high-performance perovskite solar cells with great potential for renewable energy generation. In the inverted structure as depicted in Fig. 1.6 (b), light traverses through glass, TCO, and HTL before reaching the perovskite layer, altering the optical pathway for efficient energy conversion.

However, regardless of the specific configuration, the perovskite material $MAPbI_3$ has proven to be the most representative and widely studied for photovoltaic applications. As outlined by Stoumpos et al. [53], $MAPbI_3$ adopts a high-temperature cubic phase, where the organic cation methyl ammonium ($CH_3NH_3^+$ or MA) represents the A-site in the perovskite formula, while lead and halogen occupy the B and X positions, respectively, resulting in the crystalline structure shown in Fig. 1.3. Notably, $MAPbI_3$ possesses an optimal direct bandgap ($E_g \approx 1.6$ eV) [52, 53, 69, 70].

The estimated theoretical power conversion efficiency (PCE) for a single junction solar cell based on a 500 nm thick $MAPbI_3$ layer is calculated to be approximately 31%, accompanied

by a short-circuit current density (Jsc) of approximately 26 mA cm^{-2}, an open-circuit voltage (Voc) of approximately 1.3 V, and a fill factor (FF) of around 91% [71].

1.3.2.1 Light absorption

In perovskite solar cells (PSCs), the phenomenon of light absorption plays a fundamental role in the conversion of solar energy into electrical energy. The perovskite absorber layer, typically composed of organic-inorganic hybrid materials, is responsible for absorbing photons from the incident sunlight and generating electron-hole pairs (excitons). The absorption of light in the perovskite layer occurs due to the presence of metal halide complexes and organic molecules within the material structure. These components exhibit strong light-harvesting properties, allowing for efficient absorption and utilization of a wide range of solar wavelengths. The absorption process begins when photons with energies corresponding to the bandgap of the perovskite material interact with the absorber layer. Upon absorption, the photons excite the electrons from the valence band to the conduction band, creating electron-hole pairs. The energy of the absorbed photons determines the amount of energy carried by the generated electron-hole pairs. The absorption properties of perovskite materials are influenced by factors such as the composition of the absorber layer, film thickness, and crystal structure. Optimizing these parameters allows for enhanced light absorption and improved overall device performance.

The energy absorption and photovoltaic effect in a perovskite solar cell occur primarily in the active layer. To enhance the optical absorption capability, calculations generally focus on the active layer [72]. The wavelength range considered for the calculations is from 280 to 2000 nm, covering the highest energy band of the solar spectrum. The area integral of power flow is calculated on the interfaces of the active layer, taking into account the wavelength (λ) and the difference in integral power flow between the input interface (P_{input}) and the output interface (P_{output}) of the PSC. The absorbed amount of the active layer is determined by calculating the difference between the power flow at the input and output interfaces. This value represents the absorbed amount of the active layer. The total absorption ($A_{(\lambda)}$) of the active layer is obtained by dividing this absorbed amount by the total incident solar light (P_0) using Eq. (1.1).

$$A_{(\lambda)}=\frac{P_{input}-P_{output}}{P_0} \tag{1.1}$$

Incident power for modeling area is given by Maxwell's Eq. (1.2)

$$P_{0=} c.n.\varepsilon_0.b \quad (1.2)$$

where c is light speed, n is refractive index of air, ε_0 is permittivity of free space, and b is the size of modelling area along z direction. For standard solar spectrum (AM1.5), $S_{(\lambda)}$is a curve to characterise the change of solar power flux at various wavelengths (unit W/m^2 /nm), it can be transferred to solar photon flux density, $\emptyset_s(\lambda)$, to define as the number of photons in unit time and volume (/m^2 /s) using Eq. (1.3)

$$\emptyset_s(\lambda) = S(\lambda).\frac{\lambda}{hc} \quad (1.3)$$

where h is the plank constant. Combining total absorption, $A(\lambda)$, and solar photon flux density, $\emptyset_s(\lambda)$, a factor called total absorption flux, A_{photon}, is given by Eq. (1.4)

$$A_{photon} = \frac{\int A(\lambda)\emptyset_s(\lambda)d\lambda}{\int \emptyset_s(\lambda)d\lambda} \quad (1.4)$$

It is a ratio of two integral areas, can evaluate the final absorption of certain layers in complete wavelength band. Larger factor means solar cells can store more photons from solar in unit area and time.

Perovskite materials demonstrate remarkable efficiency in absorbing high-energy photons within the ultraviolet and visible spectrum. However, their absorption capabilities significantly decrease beyond 780 nm, rendering perovskites virtually transparent to the near-infrared spectrum. This is significant because the near-infrared spectrum encompasses more than half of the total available solar energy.

1.3.2.2 Charge Generation

In perovskite solar cells (PSCs), the charge generation process plays a crucial role in converting absorbed light energy into electrical current. This phenomenon occurs within the perovskite absorber layer, where photons are absorbed and excitons (electron-hole pairs) are generated. When photons with energies matching or exceeding the bandgap of the perovskite material interact with the absorber layer, they are absorbed, exciting electrons from the valence band to the conduction band. This results in the creation of electron-hole pairs, where the electron is in the conduction band and the hole remains in the valence band. Charge separation then occurs through injection of photo-generated electrons into ETL and injection of holes into HTL as depicted in Fig. 1.7.

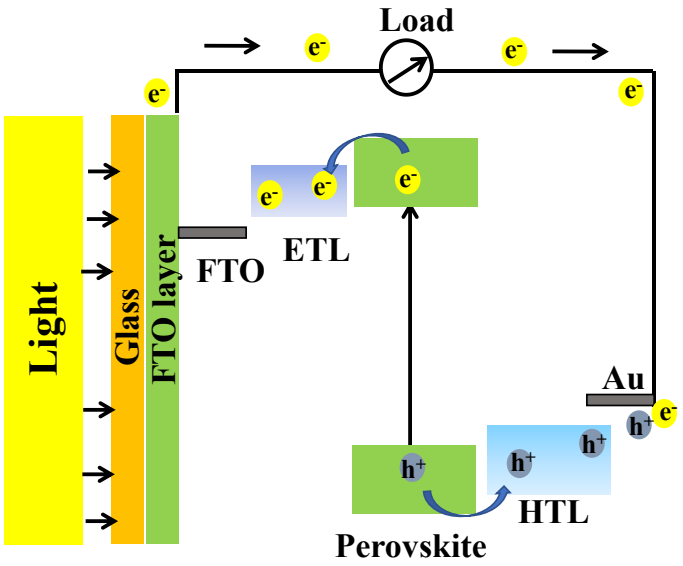

Figure 1.7 Charge transport in a perovskite solar cell showing the mechanisms of charge generation, separation, and transport within a perovskite solar cell.

The efficiency of charge generation in PSCs is influenced by several factors, including the composition and purity of the perovskite material, the crystalline structure, the film morphology, and the interfaces between the perovskite layer and the adjacent charge transport layers. Optimizing these factors is crucial for maximizing charge generation and, consequently, the overall device performance. Understanding the charge generation mechanism in PSCs is essential for designing efficient materials and device architectures. Researchers have extensively studied this phenomenon through a combination of experimental techniques, such as transient absorption spectroscopy and time-resolved photoluminescence measurements, as well as theoretical models and simulation.

1.3.2.3 Charge separation and collection

Charge separation is a crucial step in the operation of perovskite solar cells (PSCs) that aims to prevent the recombination of electron-hole pairs (excitons) and facilitate the efficient flow of charge carriers [73]. This process is typically achieved through the interface between the perovskite absorber layer and the adjacent charge transport layers, namely the electron transport layer (ETL) and the hole transport layer (HTL). The ETL plays a critical role in collecting the photo-generated electrons from the perovskite layer and facilitating their transport towards the electrode [74]. Commonly used ETL materials in PSCs include metal oxides such as titanium dioxide (TiO_2), zinc oxide (ZnO), or fullerene derivatives like [6,6]-

phenyl-C61-butyric acid methyl ester (PCBM). These materials have good electron mobility and energy band alignment with the perovskite absorber.

The HTL, on the other hand, is responsible for collecting the photo-generated holes and directing them towards the opposite electrode. HTL materials commonly employed in PSCs include organic small molecules, conjugated polymers, or organic-inorganic hybrids. Examples include poly(3,4-ethylenedioxythiophene):poly(styrenesulfonate) (PEDOT:PSS), Spiro-OMeTAD, or poly(triarylamine).

The charge separation process can be understood based on the energy level alignment at the perovskite/ETL and perovskite/HTL interfaces as depicted in Fig. 1.5. In an ideal scenario, the energy level of the conduction band minimum (CBM) of the ETL is higher than the energy level of the CBM of the perovskite layer. This energy offset facilitates the transfer of electrons from the perovskite layer to the ETL, preventing their recombination with holes. Similarly, the energy level of the valence band maximum (VBM) of the HTL should be higher than the VBM of the perovskite to ensure efficient hole extraction [48, 66, 73]. The interfacial properties and band alignment between the perovskite layer and the charge transport layers are crucial for achieving effective charge separation. Interfaces with suitable energy level alignment, proper energy offsets, and minimized interfacial defects or traps can promote efficient charge separation and suppress charge recombination.

1.3.3 Losses in perovskite solar cell

1.3.3.1 Recombination Losses

In perovskite solar cells (PSCs), recombination losses refer to the processes that lead to the recombination of charge carriers (electrons and holes) before they can contribute to the generation of electrical current. Recombination can occur when electrons and holes encounter each other and recombine, releasing the energy they gained during light absorption.

Generalized recombination dynamics of the photo-generated carriers, including radiative, defect-assisted, and direct and indirect Auger recombination.

There are several types of recombination losses that can occur in PSCs as depicted in Fig. 1.8 and are discussed below.

1. Radiative Recombination: This type of recombination occurs when charge carriers recombine and emit photons. In an ideal scenario, radiative recombination would contribute to the generation of light, which could be harnessed for increased efficiency. However, in

many PSCs, non-radiative recombination processes dominate over radiative recombination, leading to energy loss.

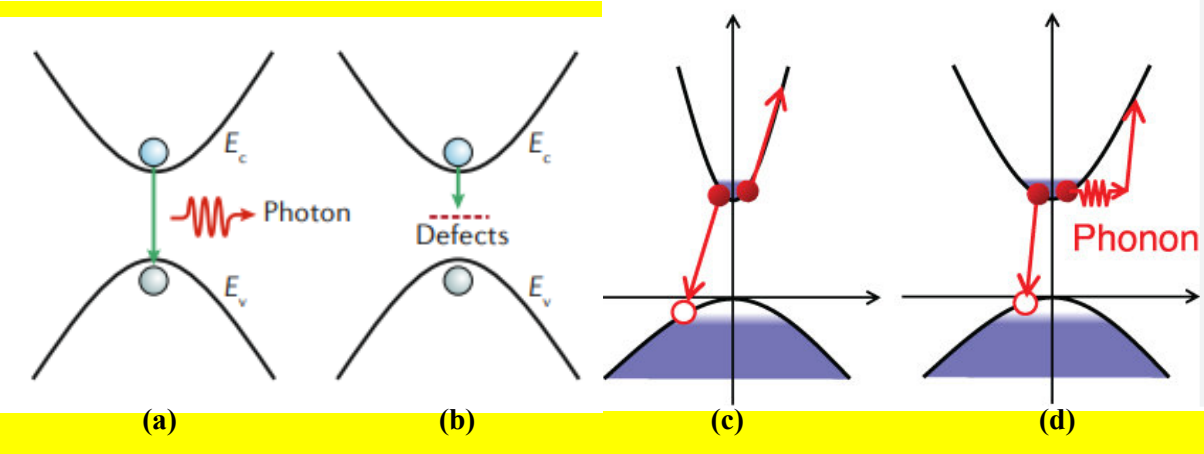

Figure 1.8 Different types of recombination in perovskite solar cell (a) Radiative recombination, (b) Defect-assisted recombination, (c) Auger direct recombination and (d) Auger indirect recombination.

2. Defect-Assisted Recombination: In this process, charge carriers (electrons and holes) recombine non-radiatively, resulting in the loss of energy. These defects can occur in the perovskite layer, at interfaces between layers, or within the transport layers.

3. Auger Recombination: Auger recombination occurs when a charge carrier recombines with another charge carrier, transferring its energy to the third carrier instead of emitting a photon. This process is particularly relevant at high carrier densities and can be a significant source of recombination losses in PSCs. Auger recombination occurs in two main forms: direct and indirect.

- Direct Auger recombination: In this process the recombination energy is directly transferred to another electron in the conduction band, exciting it to a higher energy state without involving intermediary states or phonons. This type is more common in direct bandgap materials
- Indirect Auger recombination: This process involves the assistance of a phonon to conserve momentum. This process is more typical in indirect bandgap materials and, while generally less frequent than direct Auger recombination, still contributes to efficiency losses in devices.

Carrier-recombination process includes radiative and non-radiative recombination as depicted in Fig 1.8 compete with each other. The whole recombination process can be described by Eq.(1.5).

$$\frac{dn}{dt} = -k_1 n - k_2 n^2 - k_3 n^3 \quad (1.5)$$

where k_1, k_2 and k_3 are the first-order, second-order and third-order rate constants associated with defect-assisted (monomolecular), radiative (bimolecular) and Auger (three-body) recombination processes, respectively, and n is the photo-generated carrier density.

Non-radiative recombination losses in perovskite solar cells arises from defect-assisted recombination and Auger recombination. Defect-assisted recombination is influenced by the energy levels and densities of defects present in the perovskite material. On the other hand, Auger recombination becomes more significant in perovskite absorbers with high carrier concentrations exceeding 10^{17} cm^{-3}. Defect-assisted recombination and interface-induced recombination are the primary pathways for non-radiative recombination in perovskite solar cells. Interface-induced recombination in perovskite solar cells arises from several factors, including mismatched energy level alignment, surface defects, and charge-carrier back transfer. This phenomenon represents a significant source of non-radiative recombination losses.

In an ideal scenario, a well-designed interface should facilitate the selective extraction of majority carriers while blocking the minority carriers. This is typically achieved through the presence of a large Schottky barrier at the heterojunction, along with minimal defects and surface states. However, in practice, achieving such a perfect interface is challenging. For instance, if the energy barrier for electrons at the perovskite/electron-extraction layer interface exceeds 200 meV, the extraction of electrons can be impeded. Similarly, even a finite energy barrier for holes at the perovskite/hole-extraction layer interface can lead to band bending near the contacts, resulting in a significant increase in recombination rates.

Both of these factors contribute to interfacial recombination currents in complete perovskite solar cells, leading to deviations in open-circuit voltage (Voc) values from the expected difference between the electron Fermi level (EFn) and the hole Fermi level (EFp). Additionally, the presence of undesirable surface defects and surface states further exacerbates non-radiative recombination at the interfaces. Improving interface engineering and minimizing surface defects and states are crucial for reducing interface-induced recombination losses in perovskite solar cells, ultimately leading to improved device performance and efficiency. Addressing interface-induced recombination in perovskite solar cells is crucial for achieving high-efficiency devices. This phenomenon significantly impacts the performance of the solar cells and can lead to decreased open-circuit voltage (Voc) and reduced overall power conversion efficiency.

1.4 Simulation Techniques for Photovoltaic Device Optimization

Simulation is an imperative technique to thoroughly visualize physical operation and study its various effects on the device performance. For photovoltaics PSC devices simulation, different simulation models are available. SCAPS (Solar Cell Capacitance Simulator) is a one-dimensional simulation software designed by Mark Burgelman et al. at the University of Gent, Belgium [75]. It is unrealistic and a squander of effort to develop a commercial solar cell directly without theoretical or simulation study. Simulation optimizes solar cell efficiency by decreasing effort, time, and cost besides analyzing layer features. For a device to behave like a tangible counterpart, the input parameters required for modeling the device must be enumerated carefully. Perovskite-based solar cell modeling using SCAPS-1D simulators is widely reported in the literature [76].

1.4.1 Introduction to SCAPS

SCAPS, which stands for Solar Cell Capacitance Simulator, is a computational tool used in the field of photovoltaics for simulating the behavior of solar cells. It is a software package that employs advanced numerical methods to model the electrical characteristics of solar cells based on their material properties, device structure, and operating conditions. SCAPS is widely utilized by researchers and engineers to predict the performance of various types of solar cells, aiding in the design and optimization of photovoltaic devices for enhanced efficiency and functionality [75, 77]. The simulator incorporates a comprehensive material database, allowing users to input specific semiconductor properties, and it provides detailed outputs, including current-voltage curves, efficiency calculations, and carrier distribution profiles, enabling a deep understanding of solar cell behavior under different conditions. SCAPS has proven to be a valuable tool in advancing the development and efficiency of solar energy conversion technologies.

SCAPS plays a pivotal role in the field of solar cell research and development by offering a reliable means to investigate the intricate physics governing the performance of photovoltaic devices. With its user-friendly interface, researchers can easily define material properties, device parameters, and environmental conditions to perform comprehensive simulations. This capability makes SCAPS instrumental in optimizing solar cell designs and understanding the limitations that affect their efficiency. One of the key strengths of SCAPS is its ability to model a wide range of semiconductor materials, including the rapidly evolving perovskite and organic semiconductors. As these materials hold immense promise for next-generation solar cells, SCAPS allows researchers to explore their potential and design efficient devices.

SCAPS also aids in predicting solar cell behavior under real-world conditions, including variations in temperature, light intensity, and spectral distribution. This predictive power is crucial for designing solar cells that can perform effectively in diverse environments. Furthermore, SCAPS is not limited to single-junction solar cells; it can simulate more complex multijunction cells used in concentrated photovoltaics and space applications. This versatility expands its utility in a variety of solar energy technologies. SCAPS is an indispensable tool in the field of solar cell research and development, offering researchers and engineers the means to comprehensively analyze and optimize solar cell designs. Its flexibility, accuracy, and wide range of applications make it a cornerstone of photovoltaic research, contributing significantly to the advancement of solar energy technology. The primary purpose of SCAPS, the Solar Cell Capacitance Simulator, is to serve as a crucial computational tool in the realm of photovoltaics. Its core objective is to facilitate the accurate modeling and simulation of solar cells. Researchers and engineers use SCAPS to predict and understand the electrical performance of solar cells, allowing them to optimize designs and materials for improved efficiency and functionality.

SCAPS is designed to accurately predict the electrical characteristics of solar cells, including current-voltage (IV) curves, efficiency, fill factor, and other parameters crucial for assessing solar cell performance. It solves Poisson and continuity equations with appropriate boundary conditions and the device parameters. The basic equations which govern the semiconductor charge transport are given in Eq. (1.6).

The Poisson equation is given by:

$$\frac{dE}{dx} = -\frac{d^2\varphi}{dx^2} = \frac{q}{\varepsilon}\{N_D{}^+(x) - N_A{}^-(x) + p(x) - n(x) + p_t(x) - n_t(x)\} \quad (1.6)$$

Where, E - electric field, x -position coordinate, Ψ -electrostatic potential, q - electron charge, ε - dielectric,$p(x)$,$n(x)$- concentration of hole and electron at position 'x' respectively, $N_A{}^-(x)$, $N_D{}^+(x)$- density of the ionized acceptors and donors at position 'x,' respectively, $n_t(x)$,$p_t(x)$- trapped electron and hole at position 'x,' respectively.

Eq. (1.7&1.8) describes the continuity equations for electrons and holes

$$\frac{dp_n}{dt} = G_p - \frac{p_n - p_{n_0}}{\tau_p} + p_n\mu_p\frac{dE}{dx} + \mu_p E\frac{dp_n}{dx} + D_p\frac{d^2p_n}{dx^2} \quad (1.7)$$

$$\frac{dn_p}{dt} = G_n - \frac{n_p - n_{p_0}}{\tau_n} + n_p\mu_n\frac{dE}{dx} + \mu_n E\frac{dn_p}{dx} + D_n\frac{d^2n_p}{dx^2} \quad (1.8)$$

G_p, G_n, D_p, and D_n are hole and electron generation rate and diffusion coefficients, respectively.

1.4.2 Key Features of SCAPS

SCAPS is an invaluable tool for in-depth simulation of solar cells, providing a diverse range of features. Its comprehensive material database ensures precise representation of semiconductor materials, incorporating parameters like bandgap, mobility, and recombination lifetimes. The advanced numerical solver, utilizing finite difference methods, accurately captures the complex behaviors of charge carriers, including transport, recombination, and electric field distribution. With a user-friendly interface, SCAPS facilitates effortless input of material properties, device parameters, and operating conditions, making it accessible to researchers with varying computational backgrounds [78-82].One notable feature is its ability to model multilayer solar cell structures, including tandem cells and those with multiple absorber layers, enabling the exploration of innovative designs for enhanced efficiency [83, 84]. SCAPS also considers environmental factors by allowing the study of solar cell performance under varying temperature and light intensity conditions. Additionally, its capacity to model defects and trap states is crucial for understanding their impact on carrier recombination and transport, influencing overall cell performance.

SCAPS further stands out with its transient simulation capabilities, providing insights into dynamic processes during changing illumination or operating conditions. The tool's spectral response analysis offers detailed data on how solar cells respond to light of different wavelengths, aiding in optimization for specific applications. Moreover, SCAPS supports parameter extraction and fitting, allowing researchers to refine models based on experimental data for improved accuracy [85]. Lastly, its ability to analyze charge carrier behavior at interfaces and heterojunctions contributes to a deeper understanding of how material interfaces impact transport and recombination processes [86]. SCAPS emerges as a versatile and powerful tool, seamlessly balancing user-friendliness with advanced analysis capabilities. Researchers and engineers can leverage its diverse features to accurately simulate and predict solar cell performance, actively contributing to the ongoing optimization of solar energy conversion technologies.

1.5 Research Gap and Motivation

A general perovskite material is denoted by the generalized form ABX_3, where A is an organic ion such as methylammonium or formamidinium, B is inorganic cation such as Sn^{2+}, Pb^{2+}, and X is a halogen ion such as Cl^-, Br^-, or I^-. Due to the efficient light absorption of ABX_3 (three-

dimensional) perovskites throughout the visible and near-infrared spectrum, their usage depicts the notable performance in solar cells. Recently, hybrid perovskite solar cells are being explored in the scientific community with an emphasis on $MAPbI_3$ due to their low-cost, excellent direct bandgap properties [40, 87-92], long carrier diffusion lengths [38, 93, 94], high carrier mobility [95], high efficiency and variety of composition [96-98].

High power conversion efficiency can be achieved with a relatively high impurity level [99], as PSC devices are tolerant to defects [100] due to shallow energy levels [101] and low capture cross-sections [102]. Despite these advantages, $MAPbI_3$ perovskite solar cells have the challenge of stability and J-V hysteresis, and their performance still falls below the detailed balance limit. A close look into $MAPbI_3$ perovskite has demonstrated suboptimal fill factor (FF) and open-circuit voltage (V_{OC}) deficit [19]. Comparing experimental values with the corresponding SQ limit confirms the FF and V_{OC} deficits. The SQ limit sets an upper bound for performance [103].

This limit accounts for the balance between photogeneration and intrinsic radiative recombination of thermalized carriers. Any optical conversion or electrical loss would result in PCE lower than predicted by the SQ limit [104]. Data of PSC performance parameters from various experimental works for perovskite material [105-123] are compared here with that of SQ limit values [124]. The record efficiency for PSCs, currently at 25.7% PCE [125], is still far from their theoretical Shockley–Queisser limit (SQL), which is ∼30.5% PCE for a single-junction cell based on methylammonium lead triiodide ($MAPbI_3$) [103].

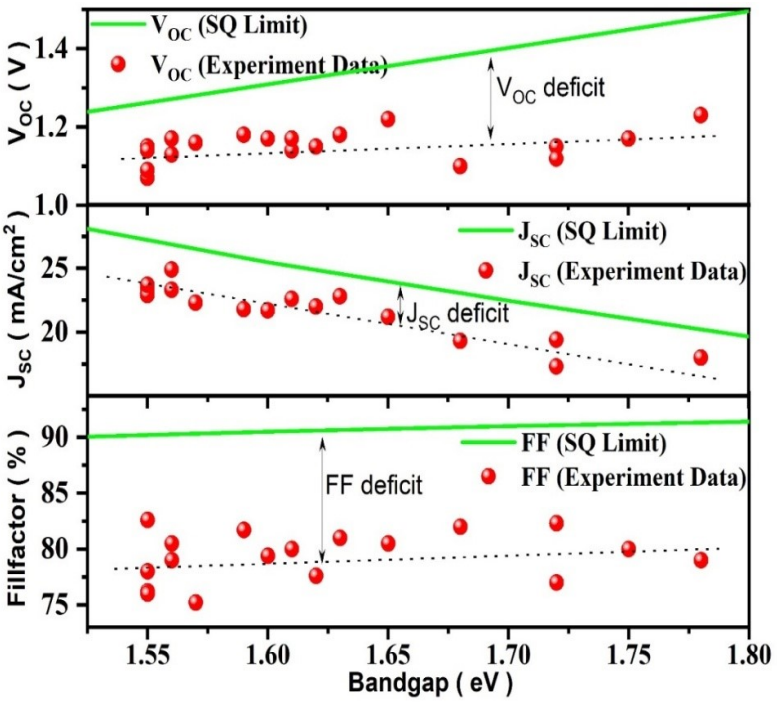

Figure 1.9 The comparison of experimentally [105-123] observed device parameters V_{OC}, J_{SC}, and FF in perovskite solar cells to the theoretical SQ limit values [124]. The dashed lines guide the eye to bring out the performance parameter deficit.

Contemporary PSC devices closely match J_{SC} values with the SQ limit value. However, FF and open-circuit voltage performance parameters significantly deviate from the SQ limit resulting in a wide research gap. Comparing PSC experimental values for J_{SC}, V_{OC}, and FF with that of SQ limit emphasizes the predominant deficit of FF and V_{OC}, as shown in Fig. 1.9.

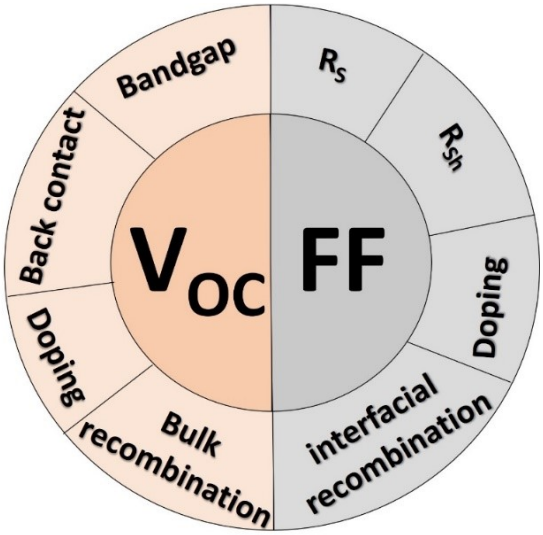

Figure 1.10 The schematic representation of design parameters that affects FF and V_{OC} output.

The motivation behind this research stems to overcome the existing limitations and further improve the efficiency of $MAPbI_3$ perovskite solar cells. It is crucial to analyze the performance parameters and understand their correlation with the structural and configuration geometry of the device. Performance parameters, such as open-circuit voltage (Voc), short-circuit current density (Jsc), fill factor (FF), and power conversion efficiency (PCE), are key indicators of device performance. However, the specific factors and mechanisms that limit these parameters in $MAPbI_3$ PSCs are not fully understood. The design parameters of perovskite solar cells that majorly influence the V_{OC} and FF of a PSC are schematically depicted in Fig. 1.10.

Establishing a comprehensive understanding of the performance parameters and their correlation with the structural and configuration geometry is essential to identify the key factors limiting efficiency and to develop strategies for optimization. By examining the relationships between performance parameters and the various structural and configuration factors, such as film thickness, composition, interface layers, and device architecture, we can gain insights into the underlying mechanisms governing device performance. Studying the correlation between performance parameters and $MAPbI_3$'s structural and configuration geometry can provide guidance for optimizing device fabrication processes. By identifying the structural features that enhance device performance, researchers can modify the fabrication techniques and design principles to achieve higher efficiencies.

Moreover, incorporating innovative absorber engineering approaches to reduce internal recombination processes and exploring the bandgap grading profile within the absorber material are crucial steps towards achieving higher efficiencies. By optimizing the double layer structure and leveraging machine learning techniques for absorber pair identification, significant advancements can be made in enhancing the overall performance of perovskite solar cells. The outcomes of this research will not only contribute to the fundamental understanding of perovskite solar cell technology but also provide practical insights for improving their efficiency. This work has the potential to revolutionize the field of renewable energy by paving the way for highly efficient photovoltaic systems based on perovskite materials.

1.6 Organization of Thesis

Chapter 1 presents a brief overview of the background of the energy scenarios energy effect on environment, and solution. Followed by the evolution of photovoltaic devices and review on

perovskite solar cells efficiency improvement over the decade and motivation of research for $MAPbI_3$.

Chapter 2 presents a summary report on device physics of perovskite solar cell details followed in this thesis work followed by a comprehensive description of the analytical tools and simulation techniques used in the analysis of the devices studied in this work.

Chapter 3 presents a brief overview of performance limiting parameters that affect the efficiency of PSCs. The research focused on characterizing device design parameters such as doping, resistance, internal, and interfacial recombination. The simulation results provided insights into the optimal ranges of these parameters for stabilizing and enhancing device performance emphasizing the $MAPbI_3$ based perovskite solar cells.

Chapter 4 focuses on overcoming limitations by incorporating innovative absorber engineering approaches. These approaches specifically aim to reduce internal recombination processes, which is crucial for enhancing the overall performance of perovskite solar cells. By mitigating loss mechanisms and improving charge carrier dynamics, these absorber engineering approaches hold the potential to significantly boost the efficiency of the solar cells. The incorporation of novel absorber designs and configurations helps minimize energy losses within the cell and optimize the movement of charge carriers. By addressing the limitations through innovative absorber engineering, this chapter contributes to advancing the field and brings us closer to achieving highly efficient perovskite-based photovoltaic systems.

Chapter 5 focuses on achieving the theoretical Shockley-Queisser (SQ) limit efficiency of that of pristine absorber for perovskite solar cells. The main approach involves tailoring the bandgap profile to optimize light absorption and minimize energy losses. The bandgap profile is carefully designed to maximize the amount of incoming light that can be effectively captured by the perovskite material. This optimization strategy aims to ensure that a larger portion of the solar spectrum is utilized, leading to higher overall efficiency. The discussion in this chapter highlights the significance of bandgap profiling in achieving higher efficiencies for perovskite solar cells and provides insights into the potential strategies and techniques that can be employed to accomplish this goal.

Chapter 6 investigates the impact of double layer optimization on enhancing perovskite solar cell performance. The focus is on identifying effective configurations to improve device performance and optimize the double layer structure for enhanced charge transport. The study explores machine learning techniques to identify optimal absorber pairs, leveraging algorithms

to achieve significant improvements in overall efficiency. By analyzing a wide range of absorber combinations, the most promising ones are identified, maximizing perovskite solar cell performance through computational models and data-driven insights. The integration of machine learning provides an innovative and efficient approach for achieving enhanced efficiency in perovskite solar cells.

Chapter 7 summarizes the present thesis work and underlines the key extension of work to be taken as future work.

1.7 Objectives of Research Work

- ✓ To analyze and establish the performance parameters that are limiting the efficiency of perovskite solar cells and establish a correlation with the structural and configuration geometry of the devices.
- ✓ To incorporate innovative absorber engineering approaches aimed at reducing internal recombination processes to enhance the overall performance of perovskite solar cells.
- ✓ To explore and optimize the bandgap grading profile within the absorber material, aiming to achieve the Shockley-Queisser (SQ) limit efficiency for perovskite solar cells.
- ✓ To investigate the impact of double layer optimization on enhancing the performance of PSCs by identifying the most effective configurations and leverage machine learning technique to identify optimal absorber pairs and facilitate the formation of a highly efficient double layer structure in PSCs.

1.8 Summary of work

Initially $CH_3NH_3PbI_3$-based solar cell simulation is carried out to identify the performance-limiting parameter - fill factor and characterize the various factors responsible for FF deficits in contemporary PSCs. The simulation analysis provided insights into the optimal ranges of design parameters such as doping, resistance, internal, and interfacial recombination, which are crucial for stabilizing and enhancing device performance. An efficiency of 23.22% is achieved by optimizing these parameters.

Further absorber optimization techniques for PSCs are proposed, specifically addressing internal recombination at interfaces. Various strategies were implemented, including asymmetric doping profiles, widening the bandgap at the absorber surface region, managing interface defect impacts, and varying the doping of the hole transport layer. By incorporating these absorber optimizations, an efficiency of 25.81% is achieved.

A comprehensive analysis is performed to achieve high-efficiency PSCs based on bandgap grading profile. Tunability of perovskite materials is used to optimize the performance of the devices. It was found that a small range bandgap variation from 1.4 to 1.2 eV at the two ends of the absorber resulted in a remarkable power conversion efficiency of 31.2%.

Later a double absorber layered perovskite device is proposed and studied through simulation analysis. Twelve different absorber layers were paired with $MAPbI_3$ layer. A systematic investigation of a double-layer structure composed of various absorber layers in PSCs was conducted. This investigation highlighted the remarkable potential of perovskite materials in achieving improved performance, with the highest recorded efficiency surpassing 35%. Further machine learning technique is employed to develop predictive models for efficiency estimation and successfully classified perovskite structures into distinct classes to form suitable double layer structure, providing valuable tools for optimizing and designing future perovskite solar cells. This study collectively contributes to our understanding of the factors affecting the efficiency of perovskite solar cells and provides valuable insights into the optimization and design of these promising photovoltaic devices.

CHAPTER 2

Literature Review

2.1 Generations of Solar Cell

Photovoltaic (PV) technology has evolved through three generations of cells: first, second, and third. The first generation, dominating the market with a 90% global share [126], consists of wafer-based silicon cells, either monocrystalline or polycrystalline. Monocrystalline cells, obtained through an energy intensive Czochralski process, are mature but expensive, achieving a 26.6% efficiency [127]. Polycrystalline cells, while more cost-effective, are less efficient. The second generation, known as 'thin film' cells, includes materials like cadmium telluride (CdTe), copper indium gallium diselenide (CIGS), and gallium arsenide (GaAs). These cells are [39]economically viable with reduced material requirements, offering flexibility and a thickness of around 1 μm [128].

The third generation, still in development, explores low-energy manufacturing and cost-effective materials. Notable technologies in this category include dye-sensitized, quantum dot, and perovskite solar cells, with perovskite cells showing significant promise. Over the last decade, perovskite solar cells have demonstrated a remarkable efficiency increase from 3.5% to 25.8% [129]. Third-generation cells, include organic photovoltaic technology (OPVs), copper zinc tin sulfide (CZTs), quantum dot cells, dye-sensitized solar cells (DSSC), and perovskite solar cells [130].

Among third-generation cells, perovskite solar cells stand out for their potential to achieve high efficiency at a low cost. They exhibit flexibility, ease of production, scalability, and the ability to react to a broad range of light wavelengths. Miyasaka et al. (2009) [39] investigated the efficiency of $CH_3NH_3PbBr_3$ and $CH_3NH_3PbI_3$ perovskite nanocrystals in sensitizing TiO_2 for visible-light conversion in photo electrochemical cells. The $CH_3NH_3PbI_3$-based photocell achieved a solar energy conversion efficiency of 3.8% and exhibited strong band-gap absorptions up to 800 nm. The $CH_3NH_3PbBr_3$-based cell demonstrated a high photovoltage of 0.96 V and an external quantum conversion efficiency of 65%.

Jeong-Hyeok et al. (2011) developed a highly efficient quantum-dot-sensitized solar cell [131] using small-sized (2-3 nm) $(CH_3NH_3)PbI_3$ perovskite nanocrystals. The perovskite quantum dots were spin-coated onto a nanocrystalline TiO_2 surface using a precursor solution. The cell achieved a maximum external quantum efficiency of 78.6% at 530 nm and a solar-to-electrical

conversion efficiency of 6.54% under 1 sun intensity. These results demonstrate the superior performance of $(CH_3NH_3)PbI_3$ perovskite quantum dots as sensitizers, surpassing other reported inorganic quantum dot sensitizers. Lee et al. (2012) demonstrated a low-cost, solution-processable solar cell using a highly crystalline perovskite absorber ($CH_3NH_3PbI_2Cl$) and achieved a power conversion efficiency of 10.9% [132]. This meso-super structured solar cell exhibits minimal energy losses and achieves high open-circuit photovoltages of over 1.1 volts. The use of mesoporous alumina as a scaffold enhances electron transport and structural organization within the perovskite absorber. This technology shows promise in overcoming fundamental energy loss challenges in photovoltaic devices.

2.2 Perovskite Solar Cell

Various photovoltaic technologies have been developed for solar energy conversion, including wafer-based, thin-film, and nanostructured solar cells. While nanostructured devices have aimed for high efficiency and have proven challenging to achieve. But, Liu Mingzhen et al. (2013) [89] has demonstrated that even in a simple planar heterojunction configuration, perovskite-based solar cells can achieve efficiencies of over 15%. This highlights the potential of perovskite absorbers in simplified device architectures without complex nanostructures.

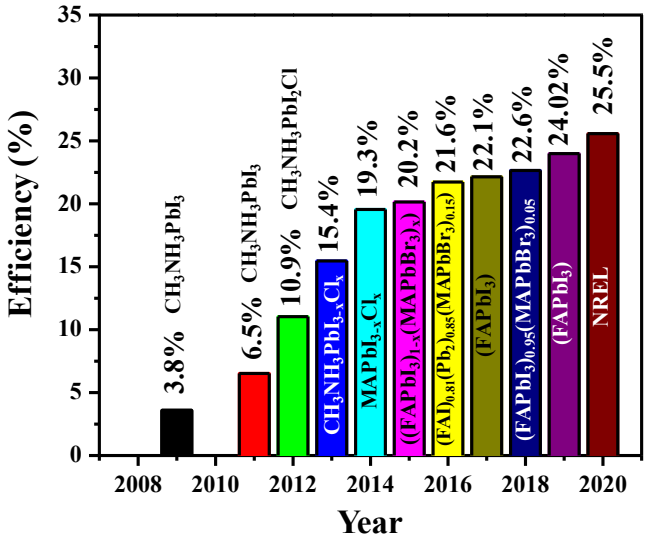

Figure 2.1 The evolution of the efficiency of perovskite solar cells from 2009 to 2020 [133].

Over the years, significant research efforts have been devoted to enhancing the PCE of PSCs. Various strategies have been explored to improve the performance of PSCs, as depicted in Fig. 2.1. Researchers have focused on developing high-quality perovskite films, enhancing charge carrier mobility, minimizing recombination losses, and optimizing device structures[134-137].

The evolution of perovskite solar cell publications reflects a remarkable growth trajectory as shown in Fig. 2.2, with the number of articles increasing from 2015 to 2023 in various renowned journals. This substantial surge in research output signifies the escalating scientific interest and concerted efforts dedicated to advancing perovskite solar cell technology over the years, underscoring its emergence as a prominent and rapidly evolving field in renewable energy research. Indeed, the growth of research in the field of perovskite solar cells has consistently been driven by the pursuit of increasing efficiency. Researchers worldwide have focused on refining material choices, optimizing fabrication processes, and innovating deposition methods to enhance the power conversion efficiency of perovskite solar cells.

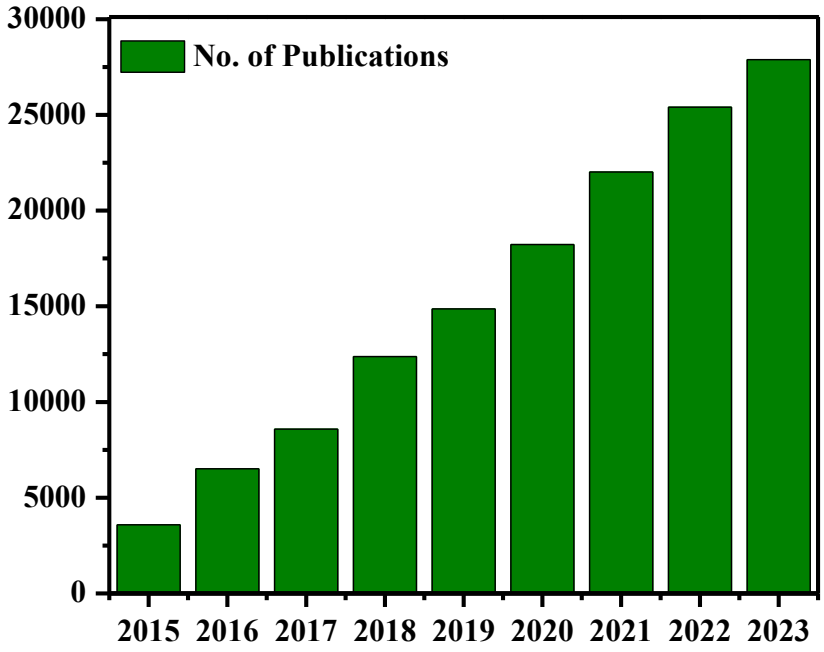

Figure 2.2 Publication Trends in Perovskite Solar Cell Research highlighting the increasing number of scientific publications related to perovskite solar cells over the years (Source: Scopus Database)

Notable advancements, such as delicate control of carrier dynamics, compositional engineering, novel deposition techniques etc., are being widely used for increasing efficiency. In the intricate realm of perovskite solar cell research, pivotal studies, such as the work by H. Zhou et al. (2014) [123] has detailed that delicate control of carrier dynamics in perovskite solar cells can lead to advancements in their power conversion efficiency. By optimizing the perovskite layer formation and material choices, carrier recombination is suppressed, facilitating injection and extraction processes. The resulting solar cells achieved an average PCE of 16.6% and reached a maximum efficiency of ~19.3% in a planar configuration without antireflective coating. Notably, the cells were fabricated in air and at low temperatures, offering

potential for inexpensive and high-performance large-area perovskite devices. W. S. Yang et al. (2015) presented a novel deposition method for high-quality formamidinium lead iodide ($FAPbI_3$) films in perovskite solar cells [138]. The method involves crystallization of $FAPbI_3$ through intramolecular exchange, resulting in films with preferred crystallographic orientation, dense microstructures, and flat surfaces. The films exhibited excellent properties with a maximum power conversion efficiency exceeding 20% in $FAPbI_3$-based PSCs. This approach offers a promising strategy for enhancing the performance of perovskite solar cells through improved film quality and broader absorption of the solar spectrum.

D. Bi et al. (2016) demonstrated a novel approach utilizing poly(methyl methacrylate) (PMMA) as a template [139] to enhance the formation of smooth perovskite films with minimal defects. These films exhibit excellent electronic quality, as evidenced by their long photoluminescence lifetime. The resulting PSCs demonstrate remarkable stability, reproducibility, and PCE reaching up to 21.6% and a certified PCE of 21.02% under standard reporting conditions. This innovative method holds great potential for advancing the performance of perovskite solar cells and facilitating their practical implementation towards precise control over nucleation and crystal growth which is crucial for achieving high electronic quality and efficiency.

The achievement of dense and uniform thin layers is crucial for optimizing the performance of perovskite solar cells (PSCs) with diverse cations and mixed halide anions. However, the presence of defect states significantly hampers cell efficiency by diminishing voltage and current density. W. S. Yang et al. (2017) introduced additional iodide ions during perovskite formation which effectively mitigated deep-level defects [122]. As a result, defect-engineered thin perovskite layers have been successfully employed in the fabrication of PSCs, leading to impressive power conversion efficiencies of 22.1% in small cells and 19.7% in 1-square-centimeter cells. These significant findings hold great promise for advancing the performance and reliability of perovskite solar cells in practical applications.

N. J. Jeon et al. (2018) performed the synthesis of hole-transporting materials with fine-tuned energy levels and high glass transition temperatures that helped in the development of highly efficient and thermally stable PSCs [140]. This study focused on the synthesis of a fluorene-terminated hole-transporting material that meets these criteria. Through the utilization of this material, PSCs were fabricated successfully with impressive efficiencies, reaching 23.2% for small-area cells and 21.7% for large-area cells under reverse scanning conditions. These results

are further supported by certified efficiencies of 22.6% and 20.9% for small-area and large-area cells, respectively. Notably, these PSCs exhibited enhanced thermal stability, with a performance retention of nearly 95% after 500 hours of thermal annealing at 60°C.

These efforts have resulted in substantial advancements, with PSCs now achieving PCEs exceeding 25%. Continued research in this field holds great promise for achieving even higher efficiencies and realizing the full potential of perovskite solar cells as a cost-effective and sustainable photovoltaic technology. The role of additives in improving perovskite solar cell performance has also been extensively studied. Among these additives, methylammonium chloride (MACl) in formamidinium lead iodide ($FAPbI_3$) perovskite has garnered attention. M. Kim et al. (2019) induced MACl as an intermediate α-phase in to the perovskite absorber. This incorporation enhanced perovskite film quality without annealing [141]. Significant improvements are observed, including increased grain size, phase crystallinity, and photoluminescence lifetime. Optimized solar cells achieve a certified efficiency of 23.48%, showcasing MACl's potential as an effective additive in perovskite solar cells.

The extensive increase in PCE of PSCs compared to other photovoltaic devices is evident from the numerous studies reviewed. Over the years, PSC technologies have undergone significant advancements, pushing the boundaries of efficiency and performance. The utilization of innovative materials, novel device architectures, and precise control over film deposition techniques have contributed to the remarkable progress in PCE. The ability of PSCs to achieve high efficiencies, often surpassing the 20% mark, showcases their potential as a promising solution for large-scale solar energy conversion. With further research and development, PSCs hold the promise of becoming a key player in the renewable energy landscape, providing a sustainable and efficient alternative to traditional photovoltaic technologies.

2.3 $MAPbI_3$ Perovskite Solar Cell

The most used perovskite material in solar cells is methylammonium lead iodide ($MAPbI_3$), often referred to as $MAPbI_3$ perovskite. $MAPbI_3$ perovskite offers several advantages that make it an ideal candidate for efficient solar cell applications. It exhibits excellent light-absorption properties, with a high optical absorption coefficient across a broad spectrum of visible and near-infrared wavelengths. This enables efficient utilization of solar energy and provides a high photocurrent generation capability [39]. Moreover, $MAPbI_3$ perovskite possesses a long carrier diffusion length, which allows for efficient charge transport within the material. This feature reduces recombination losses and contributes to the high open-circuit voltage (Voc) and short-

circuit current density (Jsc) observed in $MAPbI_3$-based solar cells [55]. The combination of efficient light absorption and charge transport properties makes $MAPbI_3$ perovskite well-suited for achieving high power conversion efficiencies.

In addition to its optoelectronic properties, $MAPbI_3$ perovskite offers advantages in terms of fabrication and processing. It can be synthesized through solution-based methods, allowing for low-cost and scalable production. W. S. Yang et al. (2017) demonstrated the solution processability of $MAPbI_3$ perovskite enables its deposition on various substrates, including flexible and lightweight materials, which opens possibilities for flexible and portable solar cells [122]. The potential of $MAPbI_3$ perovskite in photovoltaics is evident from the rapid progress achieved in the efficiency of PSCs over the past decade. Researchers have reported power conversion efficiencies exceeding 25%, rivaling those of conventional silicon-based solar cells [14]. These high efficiencies, coupled with the material's low-cost fabrication and flexibility, make $MAPbI_3$ perovskite an attractive candidate for next-generation photovoltaics. Despite its exceptional properties, there are still challenges associated with the stability and long-term performance of $MAPbI_3$ perovskite [142]. These challenges include issues related to stability, hysteresis, and the presence of nonradiative recombination centers and reaching SQ-limit efficiencies.

Rigorous research is being carried out to enhance the device's performance to reach the SQ limit. Chen et al. (2019) fabricated the $MAPbI_3$ single crystal PSCs by adapting experimental precautions like avoiding the use of solvent in the post-treatment of spin-coating and testing the device under a nitrogen-filled environment during fabrication and has achieved a PCE reaching 21.09% [105]. Cao et al. (2021) have worked on passivating the defects in $MAPbI_3$ to enhance performance and match the SQ limits. They used perylene as an additive, while chlorobenzene was an anti-solvent with different concentrations. They achieved 19.42% of PCE by using an optimized concentration of perylene as 4 $\mu g\ mL^{-1}$ [106].

Zheng et al. (2017) have shown that ammonium halides can passivate ionic defects, which are one of the underlying reasons for reduced efficiency through their charged components. Through this defect passivation, they have achieved a PCE of 20.59% [107]. Christian et al. (2017) have investigated the incorporation of fullerene derivates in ETL. This incorporation has improved V_{OC} and achieved a PCE of 19.4% [111]. Luo et al. (2018) have proposed a strategy to reduce non-radiative recombination by adapting the solution processes growth technique which improved V_{OC} and achieved a PCE of 21% [112]. Tan et al. (2017) have

fabricated the planar PSC by proposing a contact passivation strategy to suppress interfacial recombination at the absorber and ETL interface. They have implemented a chlorine cap for TiO_2 nanocrystals to achieve contact passivation, which resulted in a PCE of 20.1% [113].

In recent years, owing to their more straightforward fabrication techniques and reduced cost compared to conventional silicon solar cells, lead halide perovskite ($CH_3NH_3PbX_3$, X = I, Br, Cl) has drawn a lot of interest [143, 144]. Particularly, $CH_3NH_3PbI_3$, with a direct band gap of 1.5 eV [145], has been considered to be the ideal light absorber due to its high coefficient of extinction nearly equal to the value of 0.38085 [146, 147], lower exciton binding energy equivalent to 15-24 meV[148-150] and better charge carrier mobility of 5-12 cm^2/Vs for holes and 2.5-10 cm^2/Vs for electrons [151, 152]. Despite the discussed potential advantages possessed by the PSCs, they are far from the theoretical maximum efficiency (31%) [71]. One probable reason is the charge carrier recombination in the device, which reduces the PSCs open-circuit voltage (V_{OC}) and fill factor (FF). Degradation of the perovskite is also one of the reasons [153]. Radiative recombination in PSCs is feeble [95]. Non-radiative recombination, on the other hand, is the most predominant efficiency limiting cause in PSCs [151, 154-156].

One avenue of improvement involves an anion modification strategy, identified as a key contributor to boosting device efficiency [157]. Another promising approach is interfacial engineering, where highly π-conjugated graphdiyne employed as an interface to minimize interfacial recombination [158]. Addressing defects is also a critical focus, with research exploring the insertion of ultrathin PTAA layers to passivate defects, eliminate hysteresis, and improve the fill factor of PSCs [159]. Stabilizing the perovskite structure through doping strategies is another facet of ongoing research [160].

Domanski et al. (2016) emphasized the importance of interface engineering to mitigate recombination losses at the heterojunction interface between the perovskite absorber layer and charge-extraction layers. By improving energy level alignment and reducing surface defects, the researchers were able to enhance charge carrier extraction and achieve higher Voc values in perovskite solar cells [46]. Liu et al. (2019) highlighted the detrimental effects of interface-induced recombination on the overall performance of perovskite solar cells. The researchers demonstrated that the presence of energy barriers for electron and hole extraction at the interfaces led to increased recombination rates and deviations in Voc values from the expected values based on the energy level positions [123].

Efforts are being made to develop strategies for addressing interface-induced recombination. Mahjabin et al. (2020) shown controlling the defect in the perovskite absorber layer is a very crucial issue for developing highly efficient and stable PSCs [161]. Yang et al. (2021), demonstrated passivation of surface defects reduces the density of trap states at the interfaces. An interfacial engineering technique is used to minimize recombination losses and enhance the performance of PSCs [162]. Furthermore, Zhang et al. (2022) investigated the impact of interfacial defects and surface states on the non-radiative recombination at the interfaces of perovskite solar cells. The researchers emphasized the importance of minimizing these defects through proper materials selection and interface optimization to improve charge carrier extraction and device performance [163]. Addressing interface-induced recombination in perovskite solar cells is crucial for achieving high-efficiency devices. To address these issues, we incorporated novel absorber engineering approaches aiming to reduce the internal recombination processes to enhance the overall performance of perovskite solar cells.

Table 2.1 Comparison of Simulation and Experimental Performance Metrics of $MAPbI_3$ Perovskite Solar Cells with Recommended Optimization Parameters.

Parameter	Simulation Results	Experimental Findings	Suggested Control Parameters
V_{OC}	1.0 - 1.2 V [164, 165]	0.9 - 1.1 V [18, 166, 167]	✓ Improve interface quality to reduce non-radiative recombination. ✓ Optimize fabrication techniques to ensure consistent layer deposition.
J_{SC}	25 - 30 mA/cm² [168]	20 - 25 mA/cm² [169]	✓ Enhance light absorption with anti-reflective coatings. ✓ Minimize parasitic resistances in the device structure.
FF	75% - 85% [170, 171]	70% - 80% [172, 173]	✓ Reduce series resistance through better contact materials. ✓ Improve charge transport layer quality to minimize recombination losses.
PCE	Up to 25% [174, 175]	15% - 23% [176, 177]	✓ Implement defect passivation strategies to reduce trap states. ✓ Use encapsulation techniques to improve environmental stability.

Defect Density Impact	Lowering defect density from 10^{16} cm^{-3} to 10^{14} cm^{-3} can significantly enhance performance [178, 179]	Reduction in defect density through passivation improves V_{OC} and overall efficiency [180, 181]	✓ Optimize synthesis conditions to minimize intrinsic defects. ✓ Apply surface passivation layers to reduce surface recombination.

The Table 2.1 provides a detailed comparison between simulation results and experimental findings for key performance metrics of $MAPbI_3$ perovskite solar cells, including V_{OC}, J_{SC}, FF, PCE and the impact of defect density. Simulation results generally show higher performance values compared to experimental findings, highlighting potential areas for improvement. Suggested control parameters, such as optimizing interface quality, reducing recombination, ensuring proper band alignment, using buffer layers, and employing high-quality materials, are proposed to bridge the gap between simulation and experimental outcomes. By addressing these recommendations, we focus on refining optimizing interfaces, reduce surface recombination and band alignment to achieve higher efficiency and stability in perovskite solar cells, driving the development of more efficient photovoltaic technologies.

CHAPTER 3

Design Optimization and Insight into performance limiting parameters for $CH_3NH_3PbI_3$-based Perovskite Solar Cells

This chapter drives the theoretical study to identify and understand the device metrics/functional characteristics that impose limitations on the efficiency of $MAPbI_3$ perovskite solar cells. By conducting a comprehensive theoretical analysis and investigation, we aim to determine the specific factors that are hindering the attainment of higher efficiencies in these solar cells. This research is crucial in providing insights into the critical performance parameters that need to be addressed and optimized to enhance the overall efficiency of $MAPbI_3$ perovskite solar cells and acts as guide for the other absorber perovskite solar cells.

3.1 Introduction

Perovskite solar cells have garnered significant attention in the field of photovoltaics due to their exceptional performance and potential for high-efficiency solar energy conversion. These solar cells are based on a class of materials known as perovskites, which have a unique crystal structure resembling the mineral perovskite. These materials were widely reported in many scientific domains, but in 2009 Miyasaka et al. specified their initial usage in solar cells [39].

The design parameters that affect the functional characteristics of a PSC are depicted in Fig.1.10. The opencircuit voltage is related to the bandgap of the active material by the relation $V_{OC} = \frac{E_g}{q}$. Hence, the bandgap directly influences the V_{OC}. Recombination losses affect the current collection and injection, typically happening at the surfaces and in the bulk of the active region. These recombination losses are controlled by the number of minority carriers, their mobility and diffusion length, which depends on the localized voltage and the temperature. Hence, recombination can be minimized by optimizing the minority carrier concentration, local electric field, and parasitic resistive losses. Both series and shunt resistance losses reduce the FF and thereby the efficiency of a solar cell.

3.1.1 Series Resistance (R_s) losses in Perovskite Solar Cells

Series resistance (R_S) in perovskite solar cells is a fundamental parameter that affects the overall electrical performance of the device. It represents the collective resistance encountered by charge carriers (electrons and holes) as they traverse through various components of the solar cell from generation within the perovskite layer to collection at the external contacts.

Several components contribute to the series resistance in a perovskite solar cell. Firstly, the front contact, typically composed of a transparent conductive oxide (TCO) layer like indium tin oxide (ITO) or fluorine-doped tin oxide (FTO), introduces resistance to the flow of electrons from the perovskite layer to the external circuit due to the resistivity of TCO materials [182]. Additionally, the perovskite layer itself plays a role in series resistance, as electrons generated within it must navigate through its crystalline structure, encountering resistance along their path [93]. The back contact, often constructed from metals such as gold or silver, also contributes to series resistance, as electrons must pass through this layer before being collected by the external circuit [183].

Moreover, interconnection resistance arises from the wiring and connections within the solar cell. This includes the wires used to link different parts of the cell, such as connecting the TCO to the external circuit, further adding to the overall series resistance [184]. Understanding and mitigating these sources of resistance is crucial for optimizing the efficiency and performance of perovskite solar cells. Researchers employ various strategies to mitigate series resistance and enhance perovskite solar cell performance. These strategies include optimizing the choice of materials, improving the interface between different layers, and adopting advanced fabrication techniques [185, 186].

3.1.2 Shunt Resistance (Rsh) losses in Perovskite Solar Cells

Shunt resistance (R_{sh}) in a perovskite solar cell signifies unintended electrical pathways or short circuits that can occur, ultimately diminishing the cell's overall efficiency. These pathways provide an alternative route for charge carriers to bypass the active photoconversion region. One primary source of shunt resistance arises from leakage currents induced by imperfections or defects within the perovskite layer, such as pinholes, grain boundaries, or impurities. These flaws create unintended pathways for charge carriers, resulting in leakage currents that contribute to shunt resistance [187]. Additionally, at the edges of the solar cell where electrical contacts are established, there can be regions of lower resistivity. This circumstance creates unintended shunt pathways, allowing charge carriers to escape the active region, a phenomenon referred to as edge effects [188].

Furthermore, imperfect contacts between different layers of the solar cell, such as at the interface of the TCO layer and the perovskite layer or at the back contact, can also generate shunt paths for charge carriers, contributing to shunt resistance [118]. To mitigate shunt resistance in perovskite solar cells, endeavors focus on enhancing the quality of the perovskite

layer through improved fabrication processes, reducing defects, and refining the design of electrical contacts and edges to forestall unintended shunt pathways [189]. These strategies are vital for optimizing the efficiency and performance of perovskite solar cells.

In this chapter, we have tried to ascertain the potential factors influencing the FF of PSCs by numerical simulation study of $MAPbI_3$ devices. The primary objective of this chapter is to analyze and identify the performance parameters that limit the efficiency of $MAPbI_3$ perovskite solar cells. By conducting a systematic analysis, we aim to investigate the factors that contribute to the efficiency limitations and gain a comprehensive understanding of their impact on device performance. This objective evaluates the performance parameters, such as open-circuit voltage (Voc), short-circuit current density (Jsc), fill factor (FF), and power conversion efficiency (PCE). Through rigorous analysis, we aim to determine the specific performance parameters that have the most significant influence on the efficiency of $MAPbI_3$ perovskite solar cells. This knowledge is crucial for guiding future optimization strategies and device design modifications to enhance the overall efficiency of these solar cells.

The secondary objective of this chapter is to establish correlations between the identified performance parameters and the structural/configuration geometry of $MAPbI_3$ perovskite solar cells. We aim to investigate how structural factors, such as film thickness, carrier concentration of the absorber film and the resistance of the device are affecting the performance parameters and, subsequently, the overall efficiency of the solar cells. By systematically varying and controlling these parameters, we establish a correlation between these factors and the performance parameters. This correlation provided valuable insights into the underlying mechanisms governing device efficiency and helped to elucidate the role of specific structural features in limiting or enhancing performance. Establishing correlations between performance parameters and structural/configuration geometry is crucial for optimizing the design and fabrication processes of $MAPbI_3$ perovskite solar cells. It will provide valuable guidelines for improving efficiency by tailoring the absorber and configuration parameters to achieve higher device performance.

By achieving these objectives, this chapter aims to provide a comprehensive understanding of the performance parameters that limit the efficiency of $MAPbI_3$ perovskite solar cells and establish correlations with the structural and configuration geometry. The outcomes of this research will contribute to the development of optimization strategies, materials engineering approaches, and device design modifications to achieve efficiencies closer to the Shockley-

Queisser (SQ) limit, the theoretical maximum efficiency for a single-junction solar cell. Ultimately, this research will advance the field of perovskite solar cells and contribute to the broader goal of sustainable and efficient renewable energy technologies.

3.2 Methodology

The detailed structure of the device Au/Spiro-OMeTAD/$MAPbI_3$/SnO_2/FTO used in the simulation is depicted in the inset of Fig. 3.1 (a). The device comprises thin film of perovskite $CH_3NH_3PbI_3$ sandwiched between FTO (Fluorine doped Tin Oxide) coated glass and gold electrode at the two ends. The material parameters of each layer, such as the thickness of the layers, bandgap, electron affinity, relative permittivity, donor/acceptor concentration, carrier mobility, defect density, the effective density of valence, and conduction band are chosen from references [190-193] and tabulated in Table 3.1.

Fig. 3.1 (b) depicts the simulated characteristic J-V curve under one sun illumination and at room temperature. For light J-V characteristics, the structure has reported an open circuit voltage (V_{OC}) of 1.06V, short circuit current (J_{SC}) of 22.87mA/cm^2, with a fill factor (FF) of 76.79%, and power conversion efficiency (PCE) of 18.62% which exactly matches with the experimental device as reported in [194]. The performance of the PSC in the perspective of the deficit, as depicted in Fig. 3.1, is well influenced by several factors, viz., doping concentration, defect density, resistivity, work function, etc., which were discussed further.

Table 3.1 Device parameters for PSC optoelectronic simulation.

Material / Parameter	**FTO**	**SnO_2**	**$MAPbI_3$**	**Spiro-OMeTAD**
Bandgap (eV)	3.6	3.3	1.55	3
Electron affinity (eV)	4.2	4	3.9	2.45
Dielectric permittivity (eV)	9	9	6.5	3
CB effective DOS (cm^{-3})	10^{18}	$1.2*10^{18}$	$2.7*10^{18}$	$2.8*10^{19}$
VB effective DOS (cm^{-3})	10^{18}	$1.8*10^{18}$	$3.90*10^{18}$	10^9
Electron mobility (cm²/Vs)	200	100	5	$2*10^{-4}$
Hole mobility (cm²/Vs)	100	25	5	$2*10^{-4}$
Donor density N_D (cm^{-3})	$5*10^{18}$	10^{18}	0	0
Acceptor density N_A (cm^{-3})	0	0	$2*10^{13}$	10^{17}

Material /Parameter	$MAPbI_3$	$MAPbI_3/SnO_2$	$MAPbI_3$/ Spiro-OMeTAD
Total defect density (cm^{-3})	$5*10^{15}$	$8*10^{16}$	$5*10^{10}$
Defect type	Acceptor	Donor	Acceptor
Energetic distribution	Uniform	Uniform	Uniform
Reference energy level	> Highest E_V	>Highest E_V	> Highest E_V
Capture cross section of electron (cm^2)	10^{-15}	10^{-19}	10^{-19}
Capture cross section of hole (cm^2)	10^{-15}	10^{-19}	10^{-19}

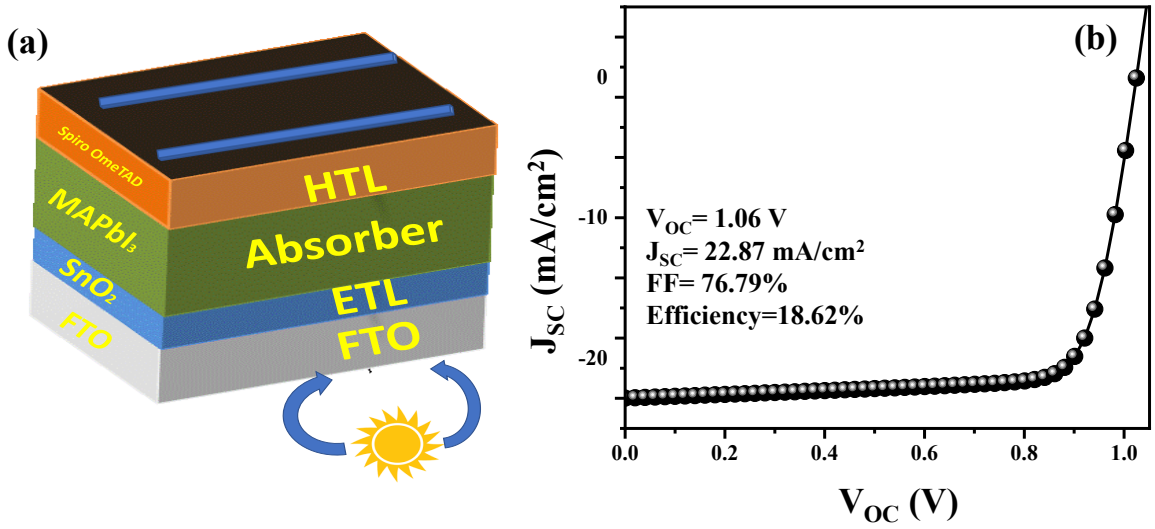

Figure 3.1 (a) Schematic representation of perovskite solar cell & (b) simulated J-V curve for the perovskite solar cell.

The density of photons absorbed in the perovskite layer under AM1.5G solar irradiation is calculated using this light absorption distribution. The photo-generation profile outlines the distribution of charge carriers in the device and is a crucial component in analyzing the device's performance. This profile is used as an initial value to solve the drift-diffusion equations. The accumulated photon density is computed by integrating the generation profile with device depth. The simulated generation rate profile of the device concerning the device depth is depicted in Fig. 3.2. According to the study, a conventional perovskite layer of about 0.3 µm in thickness is enough to capture 80% of useful photons. Absorber thickness beyond has a

significantly lower generation profile. Eq. (3.1) gives the generated profile in the absorber layer. The depth dependent maximum photocarrier generation rate profile is produced by the spectral integration of the photon density profile and is provided by the Eq. (3.2).

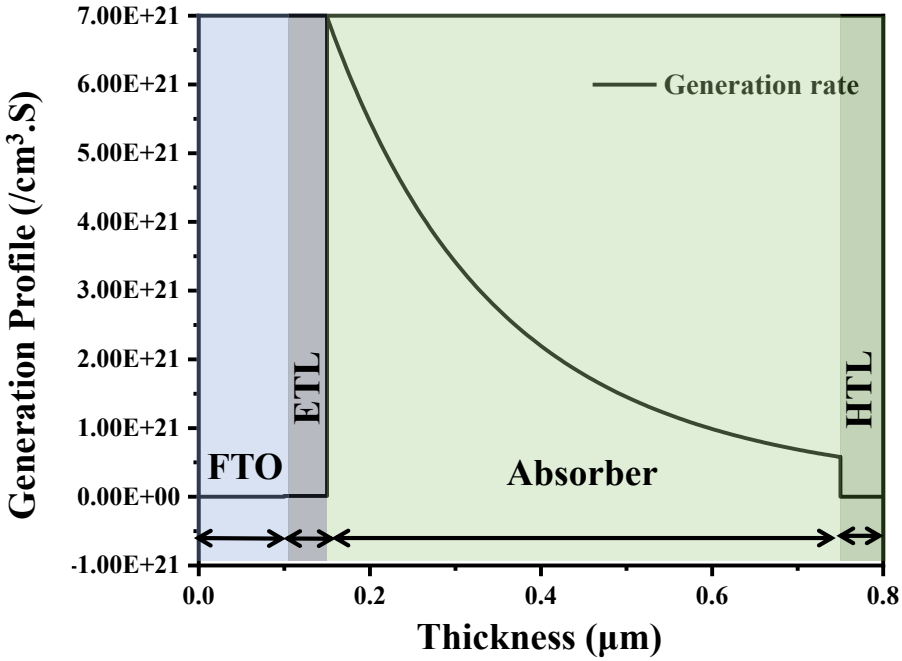

Figure 3.2 Photon density generation profile as function of device depth illustrating distribution of photon density generated within a perovskite solar cell as a function of the device's depth.

$$G(x) = Geffe\ -x/\lambda ave,\ \mathrm{G(x)} = \mathrm{G_{eff}e^{-x/\lambda_{ave}}} \quad (3.1)$$

Where G_{eff} and λ_{ave} are the material-specific constants averaged over the solar spectrum.

$$\mathrm{G_{max}} = \int_0^\infty \mathrm{G_{eff}e^{-x/\lambda_{ave}}}\,\mathrm{dx} = \mathrm{G_{eff}\lambda_{ave}} \quad (3.2)$$

3.3 Results and Discussion

3.3.1 Impact of resistances

The FF & efficiency values for experimental PSC devices, along with the corresponding series (R_S) and shunt resistance (R_{Sh}), respectively, are summarized in Table 3.2. We have considered an experimental PSC device with an efficiency above 15% for summarizing the series and shunt resistance values. It shows that series resistance values are as high as 50 Ωcm^2 and shunt resistance values are 1000 Ωcm^2. These suboptimal values of resistance are one of the possible reasons for the observed FF deficit in PSC devices.

Table 3.2 Series and shunt resistance for experimental PSC devices with efficiency above 15%.

Device	R_S (Ωcm^2)	R_{Sh} (Ωcm^2)	FF (%)	Efficiency (%)	Ref.
Au /Spiro-OMeTAD / $MAPbI_3$/TiO_2/SnO_2:F	3.2	-	-	17.5	[195]
Au/Spiro-OMeTAD/$MAPbI_3$/ TiO_2/FTO	50	1000	78	19.5	[196]
Au /Spiro-OMeTAD / $MAPbI_3$/TiO_2/SnO_2:F	4.5	2500	72	16	[197]
Au /Spiro-OMeTAD / $MAPbI_3$/TiO_2/SnO_2:F	3	4000	75	18	[197]
Ag/BCP/C_{60}/$Cs_{0.25}FA_{0.75}Pb(Br_{0.2}I_{0.8})_3$/PTAA/ITO	10-2.5	-	70-80	-	[198]

FF is majorly dependent upon shunt and series resistance of solar cell device, empirical dependence of FF [199] is given in Eq. (3.3&3.4)

$$FF_{SH} = FF_o\left(1 - \frac{V_{oc}+0.7}{V_{oc}}\frac{FF_o}{r_{sh}}\right) \quad (3.3)$$

$$FF_S = FF_o(1 - r_s) \quad (3.4)$$

Where r_{sh}, r_s is normalized shunt and series resistance. FF_{SH}, FF_S, FF_0 is fill factor as a function of shunt resistance, series resistance and independent of series and shunt resistance respectively. Fill factor will be high for high shunt and low series resistance, respectively, as per the Eq. (3.6&3.7). We simulated the ramification of resistances on FF. The impact of shunt resistance on V_{OC} under the variation of illumination intensities is simulated in Fig. 3.3 (a). V_{OC} is linearly dependent upon illumination intensity (intensity below one sun) for shunt resistance below 5K Ωcm^2. V_{OC} increases linearly at higher illuminations (above one sun) irrespective of shunt resistance values. The V_{OC} is sensitive to low shunt resistance values and low illumination intensity. With the incident photons, the buildup of the photogenerated carrier in the conduction and valence band takes place. The strength of this carrier buildup is the voltage source in the device; thus, voltage is dependent upon the illumination intensity. Eq. (3.5) demonstrates the empirical dependence of V_{OC} on the illumination intensity or generation rate [200].

$$V_{oc} = \frac{2KT}{q}\left(\ln\left(\frac{G_l\tau_o}{n_i}\right)\right) \quad (3.5)$$

G_l is the generation rate that is directly proportional to the illumination intensity. This generation-dependent V_{OC} is dominant in the low illumination region. For higher illumination, V_{OC} is logarithmically dependent upon the illumination intensity as given by Eq. (3.6).

$$V'_{OC} = V_{OC} + \frac{2KT}{q}\ln(\text{suns}) \quad (3.6)$$

Therefore, the V_{OC} has two different slopes in low and high illumination regions. The shunt resistance acts as the recombination pathway reducing the buildup of photogenerated carriers in the conduction and valence band. This reduction could be the reason for V_{OC} sensitivity toward the low values of R_{Sh} and illumination intensity, respectively. FF dependence on the illumination intensity is simulated in Fig. 3.3 (b). FF grows with an increase in illumination intensity initially, and then rapidly falls for higher illumination intensity, achieving maximum values in the 0.1-1 sun illumination region. For optimal shunt resistance (R_{sh}>1K Ωcm^2), FF is reaching SQ limit values, whereas for suboptimal shunt resistance, numerical values of FF fall rapidly. The maximum values of FF shift to higher illumination with reduced shunt resistance values. The illumination-dependent characterization highlighted the role of shunt resistance in the internal recombination process of the device. Low shunt resistance in PSC devices provides an alternate current path for the light-generated current via internal recombination. This inner recombination path must have high shunt resistance to avoid internal leakage. The impact of shunt resistance is specifically seen on FF and V_{OC} at lower illumination intensities because of the low transient built-up of the photogenerated carrier and the possibility of internal recombination pathways.

The impact of series resistance on V_{OC} is simulated to gain insight into the underlying recombination mechanism. V_{OC} increases with incident intensity irrespective of series resistance. Overlap for different values of series resistance in the V_{OC}-illumination plot is observed, as shown in Fig. 3.3 (c).

Open circuit voltage increases steeply for low illumination and saturates for high illumination intensity. Series resistance has a considerable impact on the FF under illumination intensity variation. Fig. 3.3 (d) shows that the FF is unaltered for low illumination intensity suns. For higher series resistance above >1 Ωcm^2, FF decreases with an increase in illumination intensity. The illumination dependence of FF for various R_S and R_{Sh} reveals the specific sensitivity of shunt resistance values and emphasizes the sensitive nature of FF towards R_{Sh}. Lower values of R_{Sh} impact both V_{OC} and FF nearly. Simulation reveals the optimal value of shunt resistance to be >5K Ωcm^2 for stabilizing V_{OC} and FF values.

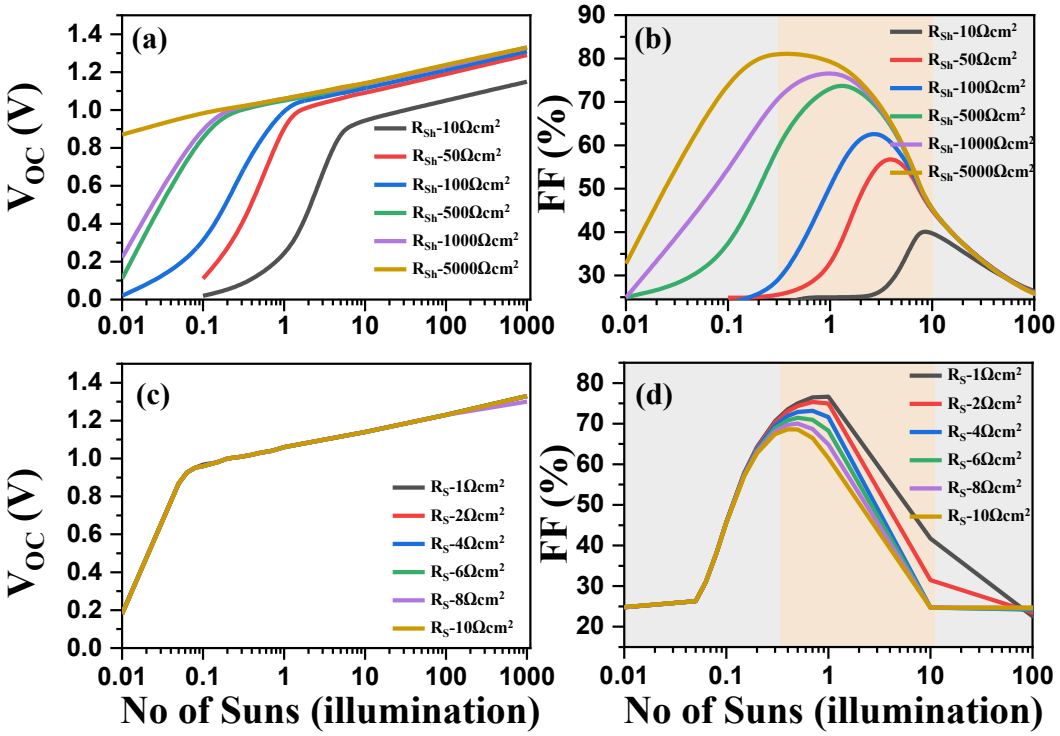

Figure 3.3 (a) V_{OC}, (b) FF as a function of illumination intensity for different values of R_{sh} values; (c) V_{OC} and (d) FF as a function of illumination intensity for different values of R_s values.

3.3.2 Impact of carrier concentration

The doping or carrier concentration is a crucial design parameter, influencing carrier mobility, carrier collection, and controls band bending at interfaces. To examine the impact of donor carrier concentration (N_D) on the performance of $CH_3NH_3PbI_3$ PSC, we have varied the carrier density from 10^{11} to 10^{18} cm^{-3} of the $CH_3NH_3PbI_3$ absorber. The band diagram of the device is simulated in Fig. 3.4 (a) for donor density at 10^{11} cm^{-3} and Fig. 3.4 (b) acceptor density at 10^{18} cm^{-3} in the perovskite absorber layer, respectively. Fig. 3.4 (a) and Fig. 3.4 (b) shows the same band bending at the interface. The dashed region highlights the band bending within the perovskite layer. The profile of band bending in the perovskite absorber with donor concentration does not show any effect with the concentration variation unlike the acceptor concentration simulated in Fig. 3.6 (a) and Fig. 3.6 (b).

Fig. 3.5 simulates the variation of performance parameters (V_{OC}, J_{SC}, FF, PCE.) with varying absorber donor density. Fig. 3.5 (a) shows the variation in FF and efficiency for donor type doping concentration in the range 10^{11}-10^{18} cm^{-3} in the absorber layer. Simulations as depicted in Fig. 3.5 (b) show that V_{OC}, J_{SC}, FF and PCE retains at the same value irrespective of the variation in donor density until 10^{16} cm^{-3} and for the concentration values beyond 10^{16} cm^{-3} a

steep decrease in all the performance parameters is observed which completely deteriorates the performance of the cell. As a result of this study, it is not recommended to choose a donor type absorber layer. If required to choose the optimal value of donor concentration is to be chosen less than 10^{16} cm^{-3}.

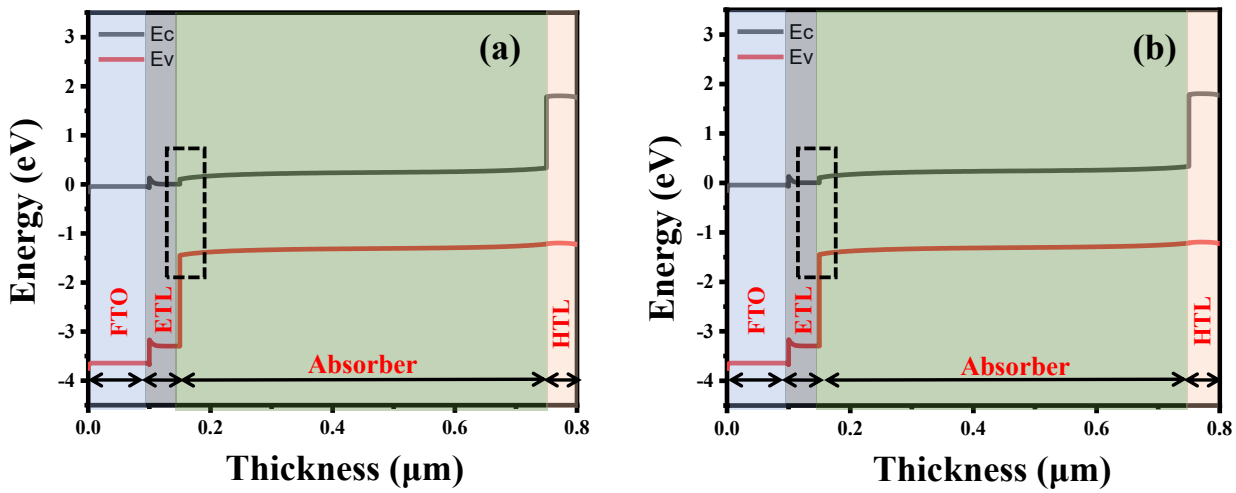

Figure 3.4 The simulated profile of band diagram under the influence of (a) low donor density and (b) high donor density in the absorber layer.

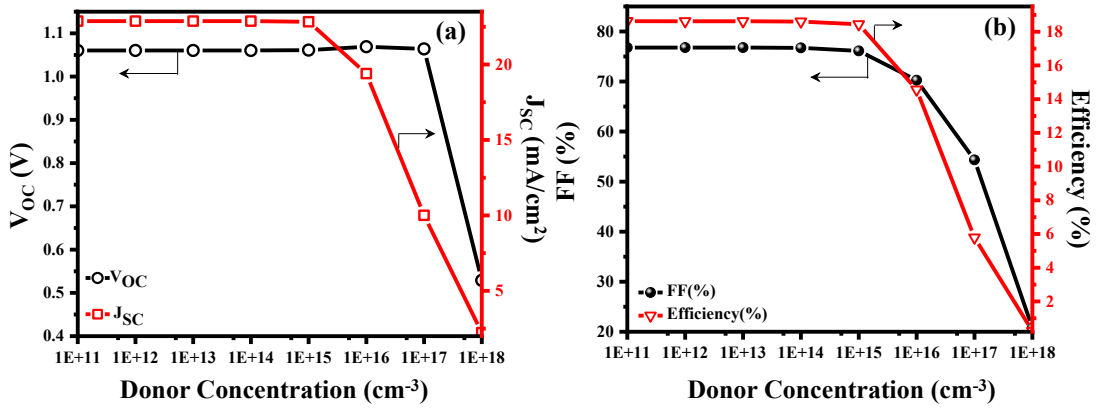

Figure 3.5 Variation of (a) FF and efficiency and (b) J_{SC} and V_{OC} as a function of donor concentration.

To examine the impact of acceptor carrier concentration (N_A) on the performance of $CH_3NH_3PbI_3$ PSC, we have varied the carrier density from 10^{11} to 10^{18} cm^{-3} of the $CH_3NH_3PbI_3$ absorber. The band diagram of the device is simulated in Fig. 3.6 (a) for acceptor density at 10^{18} cm^{-3} and Fig. 3.6 (b) acceptor density at 10^{11} cm^{-3} in the perovskite absorber layer, respectively. Fig. 3.6 (a) shows the band bending at the interface. The dashed region highlights the extent of the depletion width within the perovskite layer. The profile of band bending in the perovskite absorber with low acceptor concentration is simulated in Fig. 3.6 (b). With high

absorber density, the depletion width is limited to the interface and has a high electric field or built-in voltage, as shown by the highlighted dashed region in Fig. 3.6 (a). Low density in the absorber layer tends to have a depletion region spread throughout the absorber bulk, as shown in Fig. 3.6 (b).

Fig. 3.7 simulates the variation of performance parameters (V_{OC}, J_{SC}, FF, PCE) with varying absorber carrier density. Fig. 3.7 (a) shows the variation in FF and efficiency for acceptor type doping concentration in the range 10^{11}-10^{18} cm^{-3} in the absorber layer. Simulations show that FF maximizes at an acceptor density of 10^{16} cm^{-3} and falls steeply for higher acceptor density.

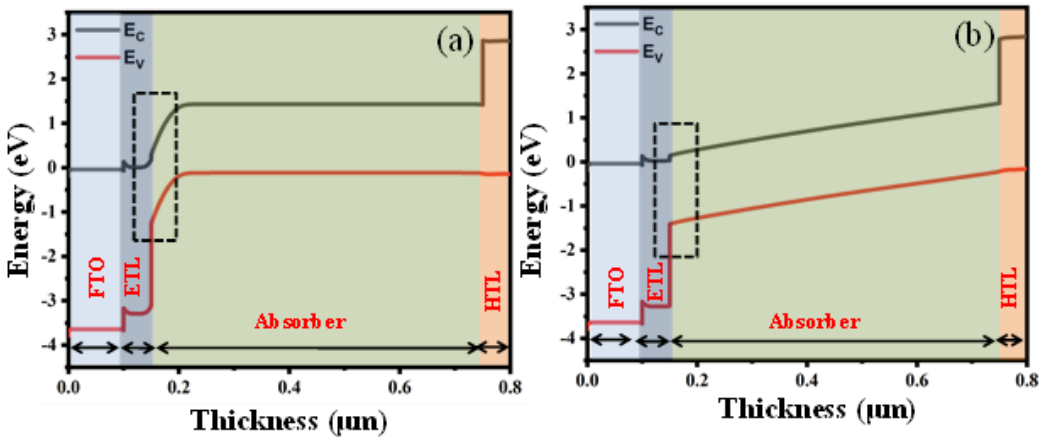

Figure 3.6 The simulated profile of band diagram under the influence of higher acceptor density in the absorber layer and (b) for low carrier density in the absorber layer.

A similar observation of FF maximizing for mid-level acceptor concentration is obtained by [76, 190, 191]. Acceptor concentration acts as p-type doping and strengthens the depletion region and built-in voltage across the perovskite/ETL junction. Increasing carrier density decreases resistivity (i.e., sheet resistance will be lower). Thus, at some mid-value of carrier concentration, FF maximizes. For increased carrier concentration of acceptor beyond 10^{17} cm^{-3}, the Auger recombination might enhance the recombination process of photogenerated carriers that results in the reduction of FF, efficiency and V_{OC}, as depicted in Fig. 3.7 (a)&(b), respectively.

SRH recombination is dominant in the lower defect density region $R_{SRH} \propto n$, Auger recombination dominates for higher defect density $R_{Auger} \propto n^2$. The resistivity or resistance is inversely proportional to carrier density $R_\rho \propto n^{-1}$. Thus, an optimized region is obtained where FF is maximized, as shown by region II in Fig. 3.8.

$$V_{in} = \frac{2KT}{q}\left(\ln\left(\frac{N_A N_D}{n_i}\right)\right) \quad (3.7)$$

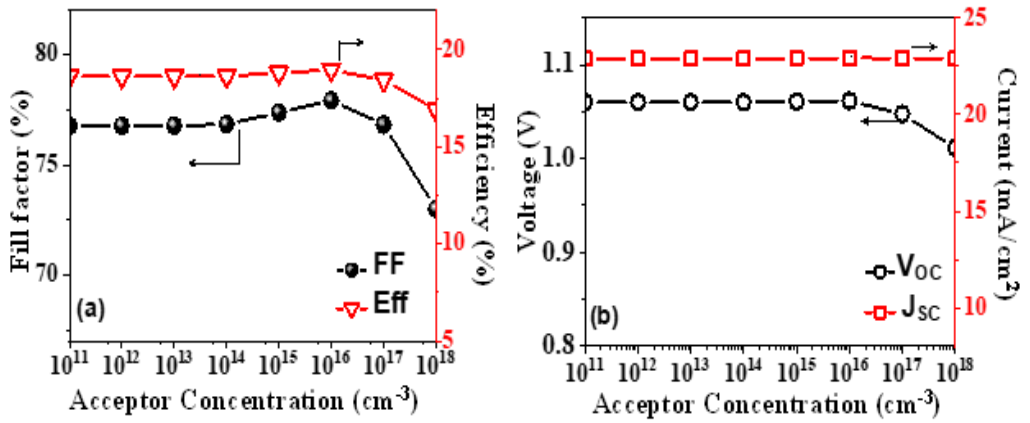

Figure 3.7 Variation of (a) FF and efficiency and (b) J_{SC} and V_{OC} as a function of acceptor concentration. FF maximizes at an acceptor density of 10^{16} cm^{-3}.

V_{OC} is dependent upon the built-in voltage, which is given by Eq. (3.7). Therefore, V_{OC} should increase with high acceptor density. Still, as depicted via simulation in Fig. 3.7 b, it falls for acceptor density beyond 10^{17} cm^{-3} due to dominant recombination (R_{Auger}) for higher density, as marked by region III in Fig 3.8.

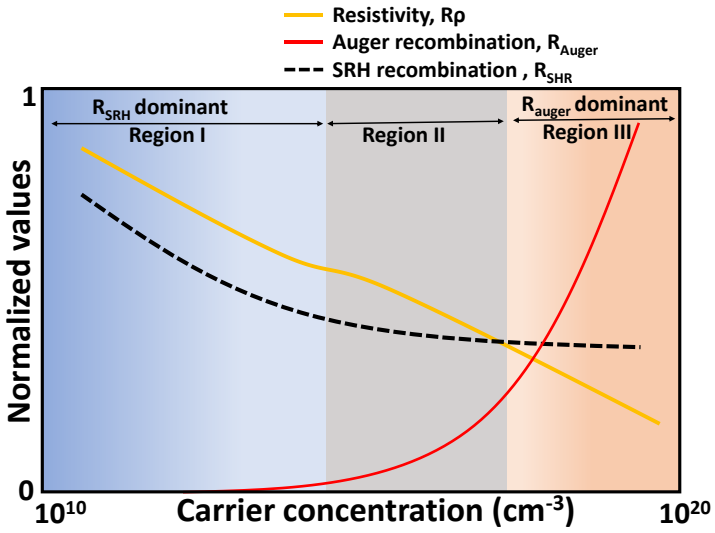

Figure 3.8 Schematic of the dominant recombination mechanism in different carrier concentration regions.

J_{SC} does not show any variation for any chosen acceptor density in the considered range. V_{OC}, FF, and efficiency show a slight depreciation for acceptor density beyond the value of 10^{16} cm^{-3}. This attributes to the carrier recombination rate for higher density in the absorber layer [143]. Defect density above 10^{17} cm^{-3} will have Auger recombination, and increased doping

concentrations result in an extended depletion region with the broader neutral region. In this, bulk recombination is robust, lowering the chance of collecting photogenerated carriers and decreasing overall efficiency. With N_A doping, the perovskite will show a p-type nature. The general nature of $MAPbI_3$ is intrinsic, with a carrier concentration of 10^{13} cm^{-3}. With N_A varying from 10^{11} to 10^{15} cm^{-3}, the performance parameters remain steady, and beyond 10^{15} cm^{-3}, they decline. The limiting device parameter for V_{OC} and FF are probed further by simulating variable sun intensity. The impact of acceptor type carrier concentration on the V_{OC} and FF is simulated for various illumination intensities in Fig. 3.9 (a-b). It shows the dependence of V_{OC} and FF on illumination (no of suns) for our PSC model.

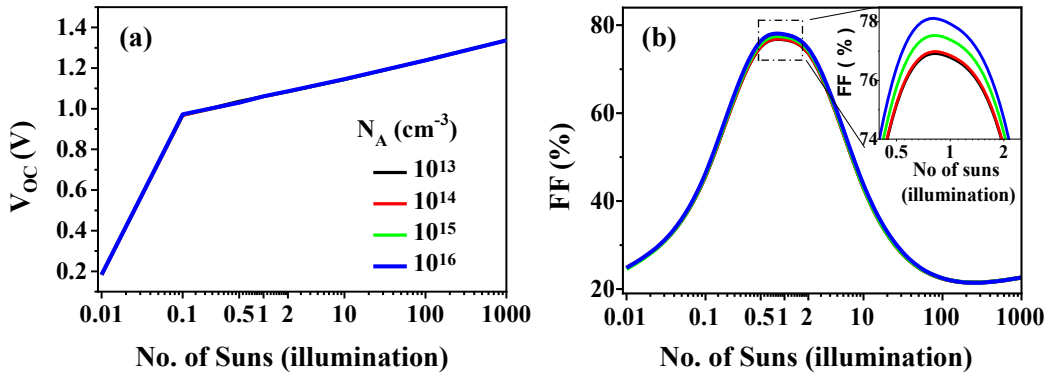

Figure 3.9 The dependence of V_{OC} and FF on acceptor concentration of perovskite absorber layer (a) V_{OC} as a function of suns for different acceptor concentrations and (b) FF as a function of suns for different acceptor concentrations.

In the low illumination region (intensity < 0.1 suns), V_{OC} steeply increases and at higher illuminations (no of suns), it increases at a lower rate. The V_{OC} illumination behavior is independent of acceptor concentration (overlapping for various acceptor densities in absorber layers as depicted in Fig. 3.9 (a). FF dependence on illumination is shown in Fig. 3.9 (b). FF increases with illumination intensity up to 1 sun i,e. 1000W and decreases for higher illumination intensity. FF increases with acceptor carrier density N_A in the illumination region of one sun, as shown in the inset of Fig. 3.9 (b).

3.3.3 Impact of defect density (N_t)

The influence of interface defects on the performance of PSC is numerically examined. The interfacial recombination in the perovskite absorber layer is highly probable. Interface recombination appears as material discontinuities, lattice mismatches, and band offsets. Besides these, defects such as grain boundaries and dislocations can also exist [201]. These defects cause charge carrier trapping, leading to non-radiative recombination of electrons and

holes. SCAPS can simulate these defects with the donor, acceptor, or multivalent nature. Table 3.1 describes the defect utilized in our simulation model in bulk and at the interface. The variation of defect density from 10^{11} to 10^{17} cm^{-3}showsconsiderable effects that influence PSC, as depicted in Fig. 3.10.

Fig. 3.10 (a-b) depicts the performance parameters V_{OC}, $J_{SC,}$ and FF, PCE variation with interface defect density at the ETL/Perovskite junction, which varies from 10^{11} to 10^{18} cm^{-3}. The simulation shows that V_{OC}, J_{SC}, and PCE decrease when interface density is higher than 10^{15} cm^{-3}. It demonstrates that an interface trap raises recombination centers, leading to the lowering of V_{OC} and PCE, whereas FF does not fall. A rise in the FF value from 75.25 to 76.75% is observed at interface defect density range from 10^{14} to 10^{17} cm^{-3} and falls for a higher defect density. As only FF improves in Fig. 3.10, the carrier transport and resistivity seem to improve under mid-level interface defect density. The probable reason is discussed in Fig. 3.8. In region II, where the resistivity is low, SRH and R_{Auger} are lower. At these carrier concentrations, FF maximizes. All the parameters monotonically fall with an increase in defect density except FF.

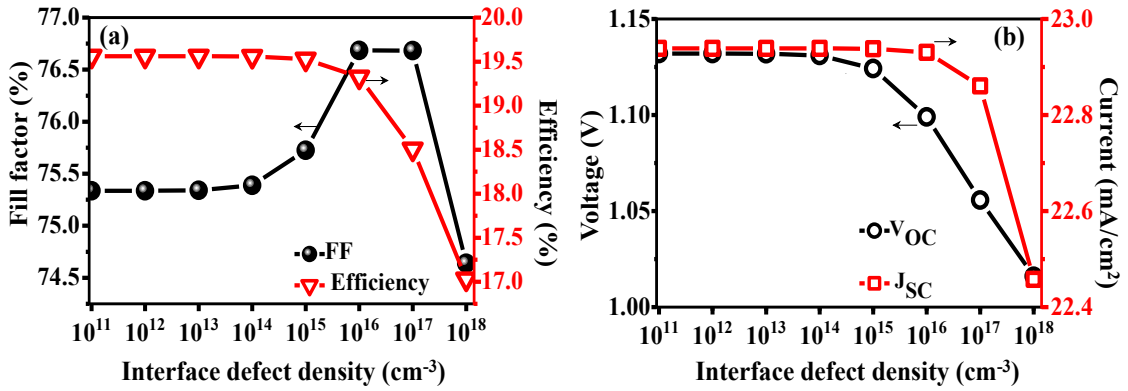

Figure 3.10 Variation of (a) FF and efficiency and (b) V_{OC} and J_{SC} as a function of ETL/Absorber interface defect density.

3.3.4 Impact of Thickness

The thickness of the perovskite absorber is varied from 0.1 to 1 µm and its effect on the performance parameters are depicted in Fig. 3.11. At the lower thickness of the absorber the generated photocurrent is very low because of lower absorption. Whereas the Voc has considerable value due to the fact that the charge extraction is high. As thickness increases Jsc increases due to improved absorption of light. It shows a linear increase from ~8.83 mA/cm^2 to ~22.87 mA/cm^2 for a thickness from 0.1µm to 0.6 µm and further than that the rate of increase is very low and almost reaches saturation with a value of ~25 mA/cm^2. This reveals

that an optimized Jsc will be achieved by the absorber layer around the thickness of 0.6 µm. Fill factor initially shows a steep increase and then declines with increased thickness because of increased series resistance. A slight decline in Voc for the thickness beyond 0.6µm is due to an enhanced recombination. The PCE improves steadily and merely due to Jsc; whereas the saturation in PCE for the thickness above 0.7 µm is because of the saturation in absorption and Jsc.

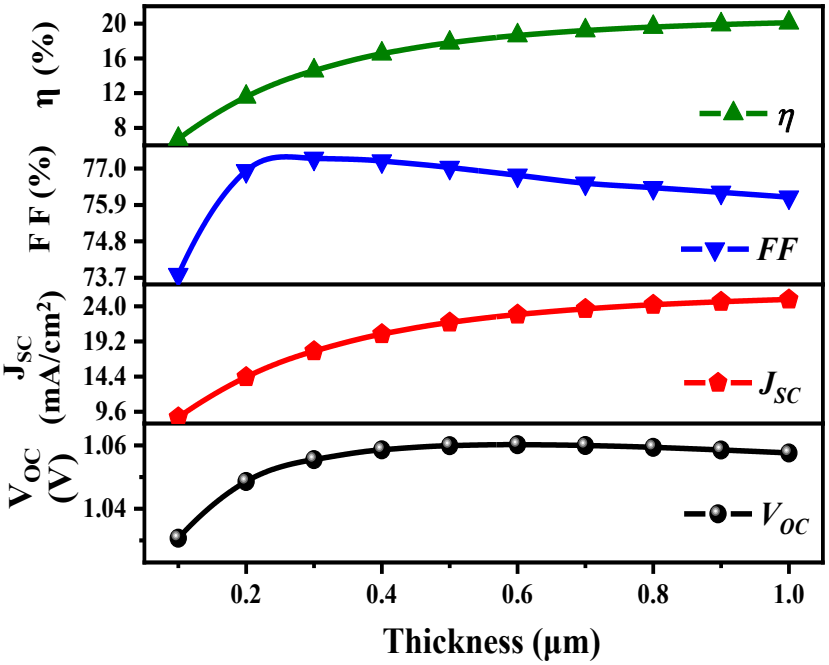

Figure 3.11 Variation V_{OC}, J_{SC}, FF and efficiency (η) as a function of perovskite absorber thickness.

The ETL thickness was varied from 0.002 to 0.05µm and its effect on the performance parameters are depicted in Fig. 3.12. At the lower thickness of the ETL all the performance parameters have depicted the lowest values. The thickness of ETL from 0.01 to 0.025 µm has shown an improved results for V_{OC}, J_{SC}, FF and efficiency. For the thickness above 0.025 µm the result sustains with saturated values. Therefore, an ETL thickness of 0.002 to 0.025 µm is appropriate for efficient results. Maximum Voc, Jsc, FF and PCE of 1.06 V, 22.87 mA/cm^2, 76.79% and 18.6% are observed respectively for thickness of 0.02 µm.

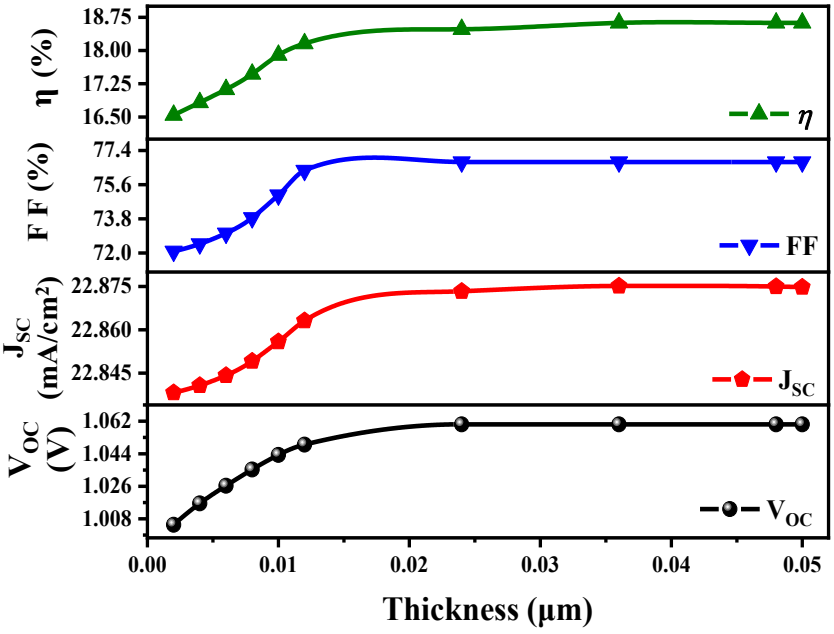

Figure 3.12 Variation V_{OC}, J_{SC}, FF and efficiency (η) as a function of ETL thickness.

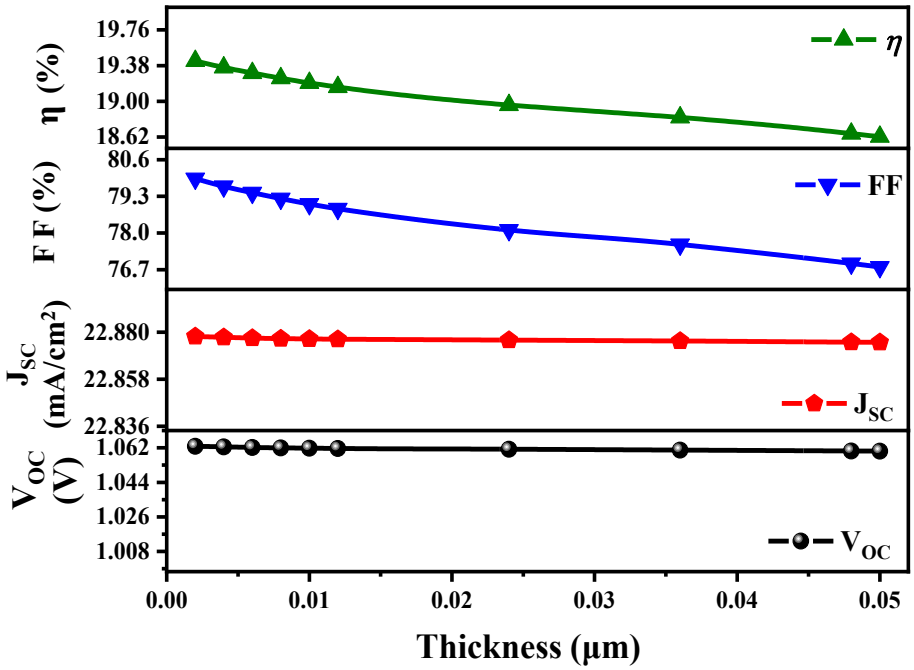

Figure 3.13 Variation V_{OC}, J_{SC}, FF and efficiency (η) as a function of HTL thickness.

The HTL thickness was varied from 0.002 to 0.05µm and its role on the performance parameters are depicted in Fig. 3.13. The obtained results show that thick HTL is not appropriate for high PCE. When the thickness of HTL is above 0.025 µm, V_{OC} reaches saturation and does not respond to further increase in the thickness. High Voc is obtained when the thickness is above 0.02 µm. Variation in FF with variation in the thickness of HTL signifies

the variation in series resistance. Reduction in FF with increased thickness of HTL is due to increased series resistance. Maximum Voc, Jsc, FF and PCE of 1.06 V, 22.87 mA/cm^2, 79.93% and 19.43% respectively were obtained corresponding to a thickness of 0.002 μm. Therefore, we opt the thickness range of HTL to be 0.002 to 0.025 μm where the result is sustained.

3.3.5 Impact of back contact work function

The influence of the back contact work function on PSC performance is numerically investigated. The back electrode is intended to grab photogenerated holes. It is responsible for collecting holes/ highly relaxed electrons entering through the external circuit. To transmit the holes properly to the back contact, they must have an ohmic contact. When the work function of the rear contact exceeds that of the HTM, holes move efficiently, whereas the electrons encounter a barrier. A dipole-orientated HTM's negative and metals positive creates an electrostatic barrier for the holes, also known as a Schottky barrier when the work function is lower [202]. As a result, difficulties develop in the conveyance of holes at contact, suggesting that a more significant work function material is required to form an ohmic contact that will conduct the hole to the electrode. [203-205]. When employing spiro-OMeTAD as HTM, the HTM's HOMO level collects holes; the deeper the HOMO, the more significant the V_{oc} [206]. Because of the shallow effective mass of holes and electrons in $CH_3NH_3PbI_3$ lattice [207] and the low effective density of states, the carrier concentration within those perovskite materials is low. This demonstrates that its work function value significantly contributes to the device performance and is examined further.

It is observed that with increasing back contact's work function, the fill factor and PCE improve, as depicted in Fig. 3.14 (a). FF attains saturation for a higher work function of back contact. Fig. 3.14 (b) simulates band banding of the PSC device for various work functions. By choosing higher work function back contact, the band banding has a higher slope, as shown in Fig. 3.14 (b). The slope of the conduction band ($\varepsilon = \Delta E_C/\Delta X$) is caused by variation in work function. This provides an additional drift field favorable for carrier collection at the hetero-junction and lowers the electron-hole recombination in the bulk absorber.

The new design will have a new effective recombination velocity for carriers in the engineered device ($S_{n\,eff}$), which can be estimated from Eq. (3.8).

$$S_{n\,eff} = S_n - \mu_n \varepsilon \qquad (3.8)$$

where μ_n is the electron mobility, S_n represents the recombination velocity of the conventional design, and ε is the electric field generated by the slope of conduction band profile [208]. The

semiconductor/metal contact affects the carrier transport, overall band banding in the absorber layer, and charge transport at the interface, thus affecting FF values. This suggests that a greater work function material is required to form a near ohmic contact with a semiconductor to conduct the hole to the electrode [203-205].

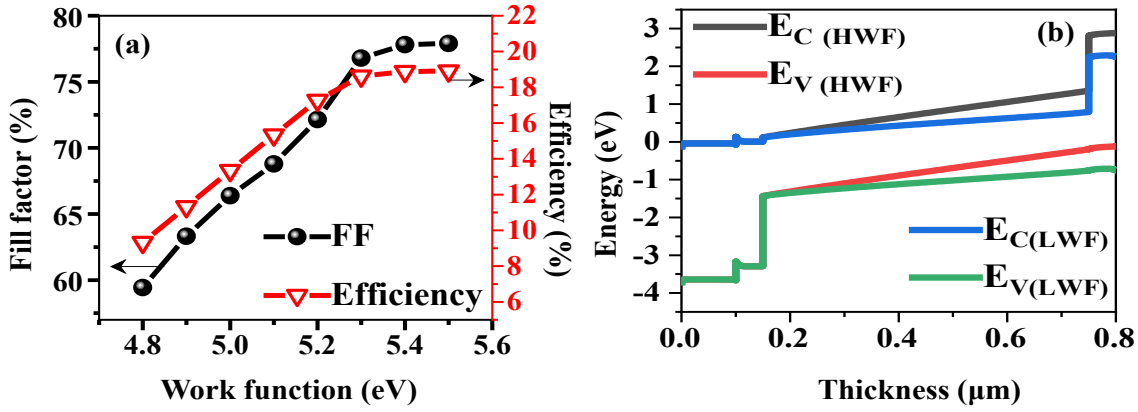

Figure 3.14 Variation of (a) FF and efficiency as a function of back contact work function and (b) The simulated band diagram of the device shows absorber layer slopes for a different back contact work function.

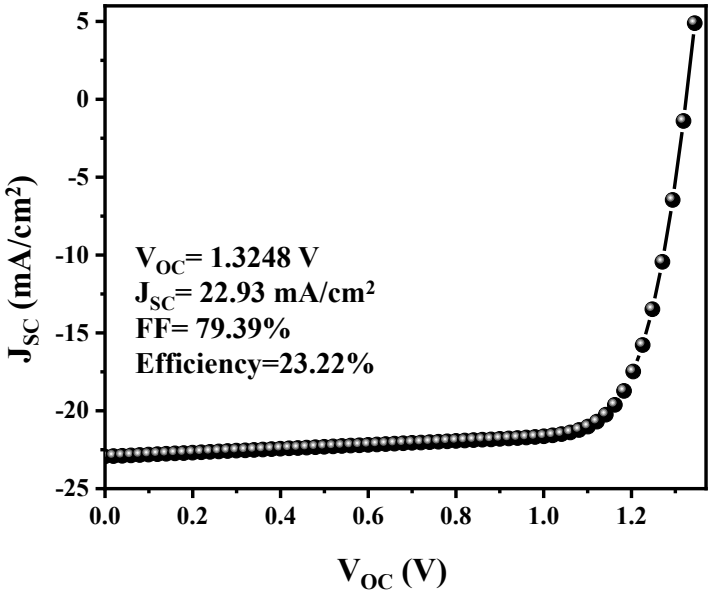

Figure 3.15 Modeled J-V characteristic for the enhanced PSC demonstrating the simulated electrical performance under standard testing conditions.

The device is finally simulated with the studied design parameters. Finally, we have chosen a robust P-type absorber with acceptor concentration of 10^{16} cm^{-3} and a matched defect density to increase the FF as discussed. The absorber, ETL and HTL thickness has been chosen as 0.6 µm, 0.025 and 0.02 µm respectively that enhanced the performance further. The simulated

device with the derived design parameters has achieved a Voc, Jsc, FF and PCE of 1.3248 V, 22.93 mA/cm^2, 79.39% and 23.22% respectively and its JV curve is depicted in Fig. 3.15. This study has shown an improved performance over the related works as shown in Table. 3.3.

Table 3.3 Comparison of $MAPbI_3$ based perovskite solar cell device with the optimized simulated device.

Absorber	ETL	HTL	PCE (%)	Ref
$MAPbI_3$ ($CH_3NH_3PbI_3$)	C_{60}	PTAA	21.09	[105]
$MAPbI_3$ ($CH_3NH_3PbI_3$)	C_{60}	PTAA	20.59	[107]
$MAPbI_3$ ($CH_3NH_3PbI_3$)	Varied	Varied	19.47	[111]
$MAPbI_3$ ($CH_3NH_3PbI_3$)	TiO_2	Spiro-OMeTAD	17.5	[195]
$MAPbI_3$ ($CH_3NH_3PbI_3$)	TiO_2	Spiro-OMeTAD	19.5	[196]
$MAPbI_3$ ($CH_3NH_3PbI_3$)	TiO_2	Spiro-OMeTAD	18.2	[197]
$MAPbI_3$ ($CH_3NH_3PbI_3$)	**SnO_2**	**Spiro-OMeTAD**	**23.2**	**This Work**

3.4 Outcomes

Based on the analysis and simulation conducted in this work on $CH_3NH_3PbI_3$-based solar cells, the outcomes are drawn as follows:

1. *Performance limiting parameter*: The study identifies the deficit in fill factor (FF) as the main performance limiting factor in the investigated perovskite solar cell (PSC) devices. Direct comparison with the Shockley-Queisser (SQ) limit values helps to highlight this limitation.

2. *Identification of parameters affecting FF deficits*: The research identifies various parameters responsible for the observed FF deficits in contemporary PSCs. These parameters include doping levels, resistance, internal and interfacial recombination processes within the device.

3. *Characterization of device design parameters*: The study characterizes the impact of different device design parameters on FF. Specifically, the effects of doping, resistance, and

recombination processes are investigated. This characterization provides valuable insights into the optimal ranges of these parameters, which are crucial for stabilizing and designing PSCs with enhanced performance.

4. *Carrier density and FF relationship*: The analysis reveals that as carrier density increases, all performance parameters except FF decrease. Interestingly, FF reaches its maximum value around an acceptor carrier density of 10^{16} cm^{-3}. This finding suggests that a robust p-type absorber with a mid-range acceptor density is beneficial for FF and overall efficiency, as it minimizes the trade-off between resistivity, Shockley-Read-Hall (SRH), and Auger recombination.

5. *Sensitivity of FF to shunt resistance*: The research demonstrates that FF is highly sensitive to the shunt resistance of the device. Experimental PSC devices with a shunt resistance of 4 $K\Omega cm^2$ indicate the need for a shunt resistance above 5 $K\Omega cm^2$ to achieve optimal FF, Voc, and efficient device functioning.

6. *Influence of back contact work function*: The study highlights the importance of the back contact work function in optimizing FF. A high back contact work function is found to lower recombination and optimize FF in the PSC device.

7. *Performance of the optimized device*: Using the derived design parameters, the research presents the performance of the optimized PSC device. The optimized device achieves a V_{oc} of 1.3248 V, J_{sc} of 22.93 mA/cm^2, FF of 79.39%, and PCE of 23.22%.

This work provides valuable insights into the performance parameters and design considerations affecting the efficiency of $CH_3NH_3PbI_3$-based solar cells. By identifying and characterizing the parameters responsible for FF deficits, the study offers guidance for designing PSCs with enhanced performance. The optimized device parameters derived from the study demonstrate improved Voc, Jsc, FF, and overall PCE. These findings contribute to the development of more efficient and stable perovskite solar cell technologies, advancing the field of renewable energy.

3.5. Summary

In summary, this chapter focused on the analysis and simulation of $MAPbI_3$-based solar cells to understand the performance parameters that limit their efficiency. The main objective was to identify and characterize the factors contributing to the fill factor (FF) deficit in perovskite solar cell (PSC) devices and establish a correlation with the structural and design parameters.

Through the simulation analysis, it was found that FF was the performance limiting parameter in the investigated PSC devices. Various factors such as doping, resistance, and internal and interfacial recombination processes were identified as responsible for the observed FF deficits in contemporary PSCs. The study further investigated the relationship between carrier density and FF, revealing that FF reaches its maximum value around an acceptor carrier density of 10^{16} cm^{-3}. This indicates the importance of a robust p-type absorber with a mid-range acceptor density for achieving high FF and overall efficiency in PSCs.

Additionally, the research highlighted the sensitivity of FF to the shunt resistance of the device. It was determined that a shunt resistance above 5 $K\Omega cm^2$ is necessary for optimal FF, Voc, and efficient device functioning. Furthermore, the impact of the back contact work function on FF was discussed, emphasizing its role in reducing recombination and optimizing FF in the PSC device. By incorporating the derived design parameters, an optimized PSC device was developed, demonstrating improved performance with a Voc of 1.3248 V, Jsc of 22.93 mA/cm^2, FF of 79.39%, and PCE of 23.22%.

Overall, this work contributes to the understanding of performance parameters and their correlation with the structural and configuration geometry in $MAPbI_3$-based solar cells. The findings provide valuable insights into the factors influencing FF deficits and guide the design and optimization of PSCs for enhanced efficiency and stability.

This chapter sets the stage for further research in the field, as the identified parameters and optimized design offer opportunities for improving the performance of perovskite solar cells and advancing renewable energy technologies.

CHAPTER 4

Absorber Optimization for Minimized Interfacial Recombination in Perovskite Solar Cells

In this chapter, configurational optimization of heterojunction perovskite solar cells using simulation techniques is conducted to mitigate internal recombination. The perovskite absorber/ETL junction is a critical site for interfacial recombination in PSCs. Our focus was on controlling carrier density near interfaces along the absorber/ETL junction to minimize interfacial recombination. We explored several design modifications, including (i) limiting majority carriers at the perovskite absorber/ETL interfaces, (ii) tuning the absorber bandgap at the interface, (c) introducing donor interfacial defects at the perovskite absorber/ETL junction, and (d) employing high rear doping of the HTL at the back contact. The feasibility of these absorber layer optimizations for reducing overall internal recombination within the device is investigated. By incorporating all these methods, an optimized device is designed that exhibited improvements in efficiency, FF, and V_{OC} by 38.61%, 5.5%, and 21.69%, respectively, compared to the benchmark device.

4.1 Introduction

With the rapid progress in solar cell performance, PSCs have taken center stage in the field of photovoltaics. Interfacial regions and heterojunctions present challenges associated with interfacial recombination at the junctions between absorber and charge transport layers, as well as between charge transport layers and metal extracting contacts. These interfaces represent the predominant origins of non-radiative losses within the PSC device. [209-212]. Hence, a detailed examination of heterojunction PSC devices and the minimization of interfacial recombination are imperative for achieving efficient performance.

An essential design strategy to manage recombination involves limiting the presence of the majority carrier at the interfaces. By adjusting the doping levels in both the perovskite and ETL layers, we can effectively reduce recombination by separating the photo-generated electron-hole pairs into their respective transport layers. This facilitates the charge separation process [213]. Material defects have a significant impact on contacts and junctions, particularly at the metal/charge transport layer junction. Maintaining a low surface recombination velocity (SRV) is essential to achieve near-Ohmic contacts [214]. Appropriate optimization of the structural design holds the potential to alleviate these constraints [215]. Hence, strategies for design optimization may be effective in reducing interfacial recombination [215]. In this investigation,

we delve into the dynamics of interfacial recombination within PSCs. This exploration encompasses the impact of various factors, including asymmetric doping profiles within the perovskite absorber/ ETL, bandgap widening of the perovskite at the interface, the influence of interface defects (both acceptor and donor defects occupying interface states), and the establishment of ohmic contacts through a high carrier density profile at the rear contact. The primary objective is to comprehensively understand these elements and formulate effective strategies to alleviate interfacial recombination in PSCs.

4.2 Basic Device Structure

The perovskite solar cell structure adapted for this study is Au/HTL/Perovskite/ETL/FTO, schematically depicted in Fig. 4.1. $MAPbI_3$ Perovskite material is used as an absorber, as widely reported [150, 216, 217] the $MAPbI_3$ absorber is chosen as p type. SnO_2 is used as ETL, and Spiro-OMeTAD as HTL. Detailed material parameters for each layer in the structure are obtained from the literature [190, 192, 193, 218] and are tabulated in Table 4.1. We have used standard test conditions (STC) to benchmark the structure. The device parameters as simulated are power conversion efficiency (PCE) of 18.62%, open-circuit voltage (V_{OC}) of 1.06V, fill factor (FF) of 76.79%, and a short circuit current (J_{SC}) of 22.87 mA/cm^2 and are matching with the experimental device [194].

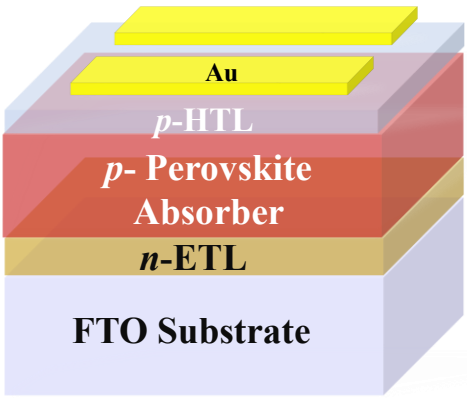

Figure 4.1 Device structure of the peer device benchmarked in simulation. The configuration of PSC is Au/HTL/Perovskite/ETL/ FTO device.

Table 4.1 Device Parameters for Optoelectronic Simulation

Material / Parameter	FTO	SnO_2	LPDTA	HNDTA	$MAPBI_3$	Spiro-OMeTAD
Bandgap (eV)	3.6	3.3	1.55	1.55	1.55	3
Electron affinity (eV)	4.2	4	3.9	3.9	3.9	2.45
Dielectric permittivity (eV)	9	9	6.5	6.5	6.5	3

Electron/Hole mobility (cm^2/Vs)	200/100	100/25	5/5	5/5	5/5	$2*10^{-4}/2*10^{-4}$
Donor density N_D (cm^{-3})	$5*10^{18}$	10^{18}	0	10^{18}	0	0
Acceptor density N_A (cm^{-3})	0	0	$2*10^{17}$	0	$2*10^{13}$	10^{17}
Total defect density (cm^{-3})	10^{15}	10^{15}	10^{15}	10^{15}	10^{15}	10^{15}
Interface Parameters for Optoelectronic Simulation						
Material / Parameter			SnO_2/ $MAPBI_3$		$MAPBI_3$/ Spiro-OMeTAD	
Capture cross section electron/hole (cm^2)			$10^{-19}/10^{-19}$		$10^{-15}/10^{-15}$	
Energetic Distribution			Single		Single	
Reference for defect energy level E_t			Varied		Varied	
Energy level with respect to reference (eV)			Varied		Varied	
Total defect density (cm^{-3})			10^{15}		10^{15}	
References			[191-193]			

Since the rate of recombination is proportional to the rate of charge carrier generation, higher recombination can arise in the depletion region at the absorber/ETL interface than in bulk quasi-neutral region. Therefore, as per the device architecture controlling the recombination at the absorber/ETL interface is crucial. Hence, to minimize this recombination, we have implemented (i) asymmetric doping in the vicinity of the interface of absorber/ETL via the incorporation of a thin layer of the absorber and appended different doping mechanisms analogous to surface doping of the absorber (ii) Wide bandgap of the absorber in the vicinity of the interface at absorber/ETL, (iii) interface defect both shallow and deep defects with varied defects and positions (iv) higher doping of absorber layer at the rear region at the interface of HTL/absorber, analogous to back surface field are investigated for the optimized device.

4.3. Results and Discussion

Auger recombination, defect-assisted non-radiative recombination, and radiative recombination are the major carrier recombination processes in PSCs, with the former two recombinations being non-radiative. Radiative recombination rate can be defined [219] as shown in Eq. (4.1).

$$R \approx \beta np \tag{4.1}$$

where p and n are hole and electron densities respectively, whereas β is the radiative recombination constant. In contrast, to defect mediated non-radiative recombination, band-to-band radiative recombination does not contribute significantly to recombination in PSCs [154, 220]. Trap-assisted recombination captured electron (or hole) at the energy state within the bandgap recombines with an opposing charge carrier, resulting in non-radiative recombination.

The traps could accumulate at junction grain boundaries [221] and the interface of perovskite/ETL (HTL) material discontinuity, lattice mismatch, etc [222]. All these bulk and interface defect accumulations appear to exist in PSCs and have a subsequent impact on the performance of the PSC device [156, 220].

The rate of trap-assisted recombination as expressed by the Shockley–Read–Hall (SRH) theory is specified by Eq. (4.2).

$$R_{SRH} \approx \frac{np}{\tau(p+n)} \tag{4.2}$$

with τ being the carrier SRH lifetimes, respectively.

The Auger carrier recombination process is given by Eq.(4.3) [223].

$$\frac{dn}{dt} = \frac{-1}{\tau n - \beta n^2 - k n^3} \tag{4.3}$$

with n - photo-generated charge carrier density and β, k are radiative and Auger recombination constant.

The Auger recombination constant value in high-efficiency PSCs is $\sim 10^{-11}$ cm^3 /s [224]. Auger recombination is insignificant for lower carrier doping concentrations ($\sim 10^{-18}$ cm^3); thus, it has a negligible effect on PSCs recombination [225]. SRH-mediated recombination is crucial to minimize recombination. The essential factors to be considered remain in controlling trap-assisted recombination, in bulk and at the interface of perovskite/ETL. To explore carrier transport through the interface and recombination current flowing through it under various doping concentrations and band banding profiles, we numerically solved the Poisson-Schrodinger equation under light illumination conditions. The pin configuration of perovskite is modified to achieve an asymmetric doping profile by using an absorber near interface region doping, widening the bandgap at the surface region, various interface defect profiles, and rear hole doping in the absorber.

4.3.1 Restricting majority carrier doping at the interface (absorber/ETL interface)

The absorber surface region in the proximity of the absorber/ETL interface is vital to steer the interfacial recombination. The interface state of absorber/ETL ($MAPbI_3$/ SnO_2) has access to holes being the majority carriers from the absorber and electrons from the ETL layer. Restricting the absorber's majority carriers at the interface will make the interface trap state redundant. The lower density of absorber majority carriers in the vicinity of the absorber/ETL

interface reduces the likelihood of majority carriers occupying the interface state and reduces interfacial recombination.

The probable hypothesis for this cause is that the ETL (SnO_2) has a high density of electrons, and the absorber ($MAPbI_3$) being p doped has a high profile of hole density, enhancing the electron-hole recombination at the absorber/ETL junction through the interface states. When the hole is restricted to access interface states, the electron only will occupy these states. In such a scenario, the photo-generated electron in the absorber will not recombine through the electron filled interface trap states.

Hence, restricting the majority carriers from accessing the interface is achieved by asymmetric doping profile at the interface (Absorber/ETL) by inserting an additional thin layer (10 nm) of absorber ($MAPbI_3$) with a decreased density of hole concentration (Lightly p doped absorber – LPDTA) and maintaining all other parameters identical to $MAPbI_3$. We insert the surface region with controlled carrier density without altering the doping or carrier concentration of bulk perovskite absorber. This can be achieved by using surface doping of perovskite. This LPDTA requires carrier density modification at the surface. Such a surface modification of densities is reported in the literature [226-228]. There are other reports on doping of perovskite [229-233] where it is reported that photoluminescence quantum yield can be increased by doping by accelerating radiative recombination. It might as well result in the reduction of diffusion length at high doping densities besides the improvement in V_{OC} and photoluminescence quantum efficiency (PQE) [229].

Higher doping densities cause a reduction in the Shockley-Read-Hall recombination (RSRH), which is constrained by the rate of electron capture. The electron concentration within the device varies linearly with the electron capture rate. As acceptor doping density increases, the electron concentration drops, and the hole concentration rises, decreasing the electron capture. It turns into the rate-limiting phase in the reduction of RSRH. The radiative and Auger recombination rate increases with the increased acceptor doping. Even if the proportion of each separate recombination process changes, the average overall recombination rate derived from the interaction of these three rates remains essentially constant. Depending on a number of variables, including the mobility's of the various layers and the ratio of the charge carrier capture cross sections, the photovoltaic performance may increase at an optimum doping density. Many literature reports reported doping in specific sites of $MAPbI_3$. Doping of $MAPbI_3$ results in enlarged grain size, improved surface morphology, enhanced crystallinity, and

reduced defect density [230-233]. Recently perovskite doping with super-alkalis investigated by Tingwei Zhou et al. [234] reported stable dynamics and relevant tolerance factors.

The acceptor density of the absorber can be altered by varying the MAI and PbI_2 ratios in the precursor solutions. Observations made by the Hall Effect of different films fabricated by varied precursor ratios from 0.3 to 1.7 showed varied doping of p and n at different precursor ratios [228]. The perovskite films, produced with a precursor ratio of 1.0, exhibited significant n-doping, characterized by a high electron concentration of $2.8 * 10^{17}$ cm^{-3}. The electronic characteristics of these films proved to be responsive to variations in the pre-mixed precursor ratio. Decreasing the precursor ratio to 0.65 resulted in a notable reduction in electron concentration to $8.1 * 10^{16}$ cm^{-3}, while an increase in the ratio to 1.7 elevated the electron concentration to $3.5 * 10^{18}$ cm^{-3}. Notably, lowering the precursor ratio to 0.3 induced a transition in the perovskite films from n-type to p-type, accompanied by a hole concentration of $4.0 * 10^{16}$ cm^{-3}. This experimental evidence, showcasing the dual-nature doping capability of methylammonium lead triiodide through compositional changes, corroborated the earlier predictions of unintentional doping by Hong [227] and Yin et al.[226]. Tuning the precursor ratio of MAI and PbI_2 can be used to tune the carrier density.

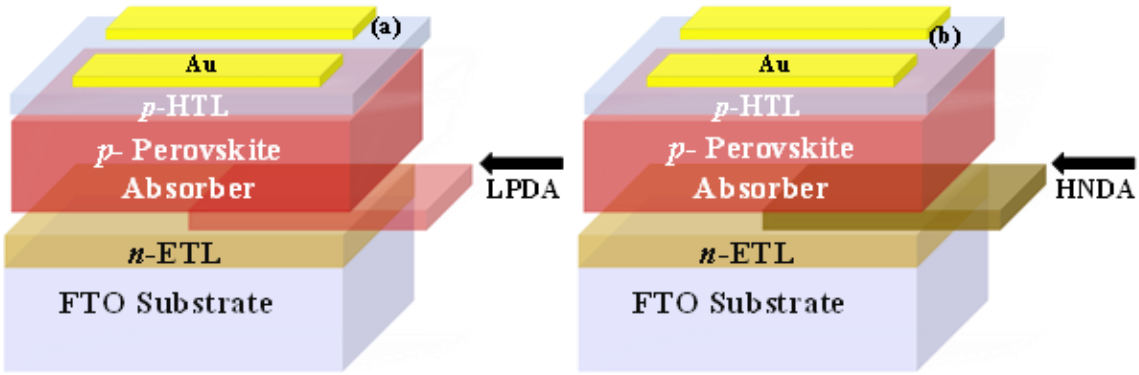

Figure 4.2 Schematic of device optimization (a) lowering the hole density in the absorber region in the vicinity of the interface by inserting a thin layer of lightly p-doped absorber (LPDTA), (b) increasing the electron density at the interface by inserting a heavily n-doped absorber (HNDTA) at the interface.

The LPDTA device, which restricts hole density at the interface, is depicted in Fig. 4.2 (a). As the concentration of majority carriers (holes) has decreased at the interface, it ultimately supports the electrons to occupy the interface states, decreases the photo-generated electrons and traps state electron recombination. The LPDTA device shows an efficiency of 20.28%.

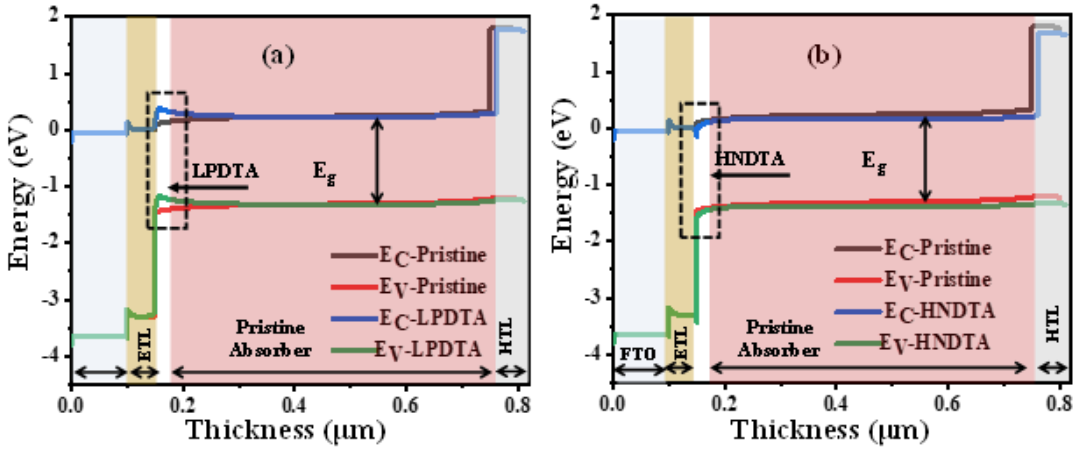

Figure 4.3 Comparative energy band schematics (simulated) for (a) Pristine (Benchmark)-LPDTA (b) Pristine (Benchmark)-HNDTA device. It shows that the energy offset modifies to spike type in case of LPDTA, and in case of HNDTA energy offset is cliff type.

The presence of metal ions (strontium, cerium, silver ions, etc.) as impurities in the perovskite precursors can lead to n-type doping of the perovskite surface to metallic nature [213]. Metal impurities are attracted to the surfaces due to their limited solubility in the halide perovskite crystals, making the surface region behave as n-doped. This scenario is simulated with increased density of electron concentration (heavily n-doped absorber – HNDTA) at the interface (Absorber/ETL) by inserting a thin layer (10nm) identical to $MAPbI_3$. The mimicked HNDTA device is depicted in Fig. 4.2 (b).

A change has been observed in the interfacial energy offset with p-type (LPDTA) or n-type (HNDTA) layer insertion. The simulated band diagram is depicted in Fig. 4.3 (a) &(b) marking the energy offset region in both the case of LPDTA and HNDTA layer insertion. We observed that the energy offset formed in LPDTA insertion lowers interfacial recombination and is beneficial for device performance. This observation is in line with other reports [235].

The J-V characteristics of the benchmark, HNDTA and LPDTA device are depicted in Fig. 4.4. The interface recombination is lowest in the case of HNDTA. Whereas, HNDTA has shown the highest bulk recombination, as represented in Fig. 4.4 (b), due to the presence of both the types of majority carriers in bulk, which led to an enormous increase in internal recombination. LPDTA device has substantially decreased the interface recombination compared to the benchmarked and the HNDTA device. Fig. 4.4 (c) summarizes an optimized LPDA device configuration to improve the efficiency and reduce the device's overall recombination.

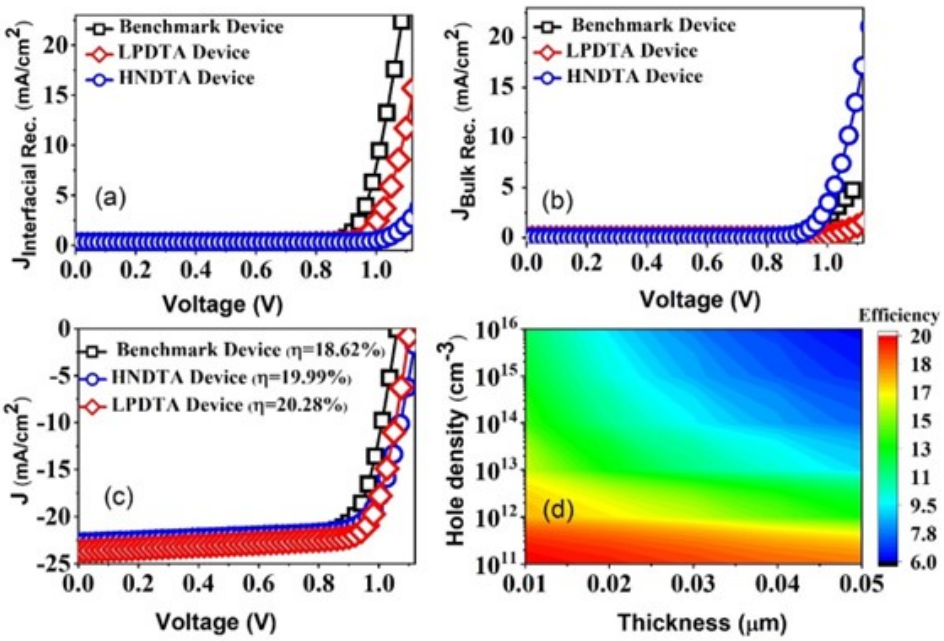

Figure 4.4 Comparative (a) Bulk recombination current, (b) Interface recombination current, (c) J-V characteristics curve for Benchmark, HNDTA and LPDTA device, (d) 2D contour plot depicting the variation of efficiency as a function of the carrier density profile of inserted absorber (LPDTA) and its thickness.

Further, we have investigated the influence of the thickness of inserted thin layer along with the carrier density profile on the device's efficiency. As the thickness of the inserted LDPTA increases, the separation of charge carriers narrows down, decreasing the overall efficiency. An increase in the charge carrier density of the surface region to the extent that matches the carrier density of ETL will enhance the interface recombination as depicted in contour plot Fig. 4.4 (d).

The LPDTA shows decreased interface and bulk recombination than the benchmarked device. This validates that lowering the absorber's hole density profile in the vicinity of the surface region conclusively narrows down the recombination via interface state. Nevertheless, implementing HNDA exhibits reduced interface recombination compared to LPDTA and benchmarked devices but has more bulk recombination than LPDTA and benchmarked devices. Therefore, restricting hole density at the interface achieved through LPDTA results in optimized efficiency than both HNDTA and benchmarked devices. Implementing this technique in practical device is challenging and require addressing the issue of doping and controlling carrier densities. Extensive research [213, 236-239] is being carried out to investigate the surface doping techniques of perovskite.

4.3.2 Band gap widening at the interface (absorber/ETL interface)

The bandgap is increased in a very thin top region of perovskite at the absorber/ETL interface. It is done to increase the interface barriers for holes and electrons. This widening in the surface region of the absorber is done by maintaining the electron affinity constant and increasing the bandgap. This optimization is to achieve a scenario analogous to valence band offset (VBO) at the absorber/ETL interface. This scenario at the junction is of a staggered gap (Type II junction), which is a favorable condition for carrier transport from the absorber to ETL. Making the absorber valence band maximum (VBM) far from ETL conduction band minimum (CBM) increases the hole-electron recombination barrier and limits the interfacial recombination. This approach is implemented in simulation by considering a thin layer (10 nm) of absorber ($MAPbI_3$) with an increased band gap, as depicted in Fig. 4.5. Simulation shows that a wide bandgap thin absorber layer (WBGTA) of around 1.65 eV at the interface is optimal. It increases the interfacial barrier for holes of the absorber layer at the interface of absorber/ETL by showing a strong type-II band alignment and thereby reduces the interfacial recombination. The impact of surface bandgap variation on device efficiency via interfacial recombination is studied. The variation in the band gap of the inserted thin layer is given by Eq. (4.4).

$$\Delta E_V = E_{CBM\ ETL} - E_{VBM\ Perovskite} \quad (4.4)$$

The valence band offset ΔE_V increases by increasing the wide bandgap WBGTA layer. The higher ΔE_V correspond to a high interface recombination barrier for electron and hole [240].

Widening the bandgap (ΔE_V) of the absorber's surface at the absorber/ETL interface, as simulated in Fig. 4.6 (a-b), enhances the barrier for the majority carriers of the absorber to occupy the interface states. Hence results in reduced interface recombination and thereby, total recombination compared to the benchmark device as depicted in Fig. 4.6 (a-b). Fig. 4.6 (c) depicts the enhanced performance over the benchmark device with an efficiency of 19.55% and improved FF of the WBGTA device.

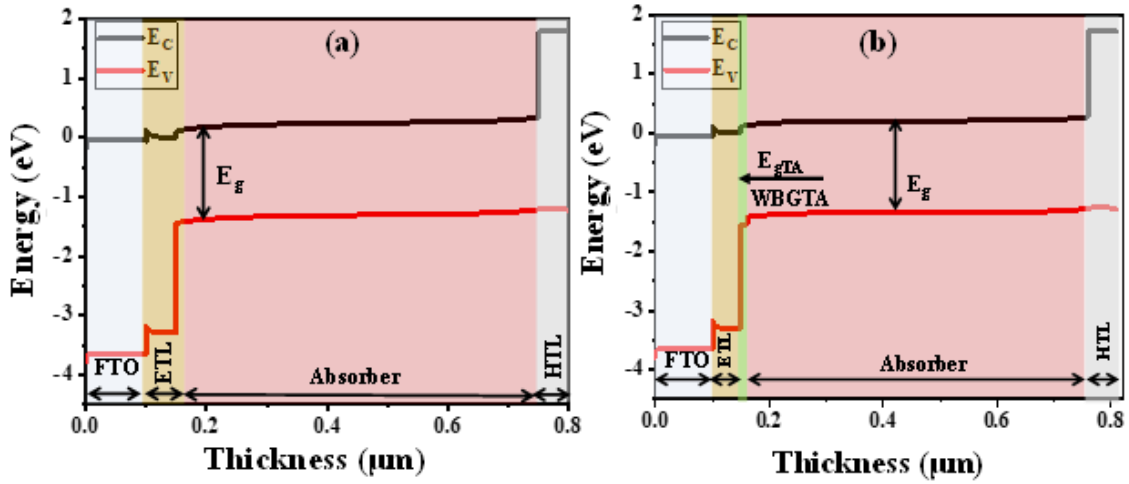

Figure 4.5 Energy band schematics for (a) benchmark device and (b) wide bandgap absorber at the interface (WBGTA).

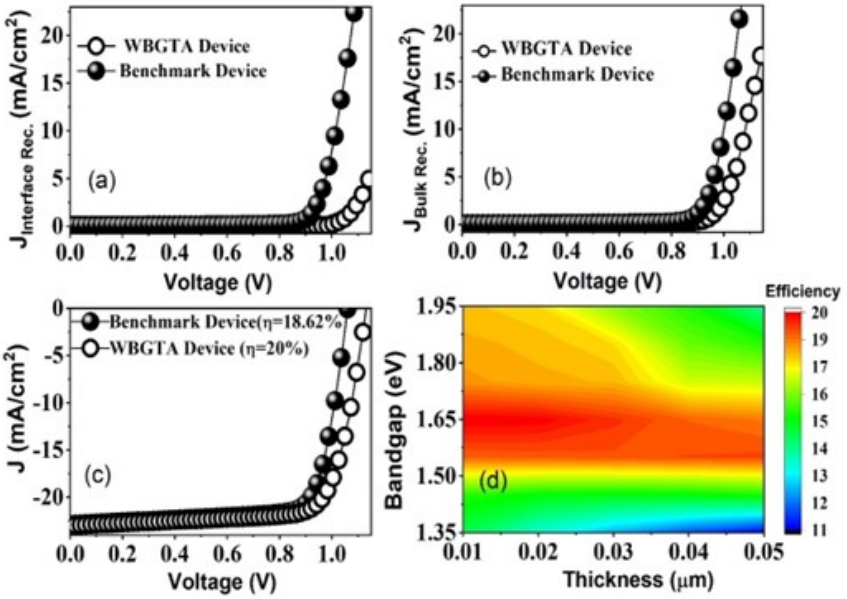

Figure 4.6 Comparative (a) Interfacial recombination current, (b) Bulk recombination current, (c) J-V characteristics curve for benchmark and WBGTA device, (d) 2D contour plot depicting the variation of efficiency as a function of band gap variation of inserted absorber (WBGTA) and its thickness.

The dependence of efficiency with the variation of the bandgap of the WBGTA at the absorber/ETL interface and its thickness is depicted in contour Fig. 4.6 (d). Efficiency is observed to maximize for WBG value of 1.65 eV beyond this efficiency decrease for higher bandgap. As the thickness of the inserted WBGTA increases, it starts behaving as a separate absorber layer and at higher band gap variation with increased thickness shows the impact of WBG absorber by decreasing the current and hence narrows down overall efficiency.

Therefore, surface bandgap variation of perovskite at the absorber/ETL interface enhances the device performance by reducing internal recombination.

4.3.3 Interface defect profile

An ideal perovskite crystal structure has ions located in the equilibrium site. Whereas in real-time scenarios, structural defects are unavoidable due to a mismatch in the lattice alignment that leads to grain boundaries and point defects. Based on the theoretical calculations of Yan et al., $MAPbI_3$ has 12-point defects, out of which 3 are vacancy defects (MA (V_{MA}), Pb (V_{Pb}), and I (V_I)), three are interstitial defects (MA (MA_i), Pb (Pb_i), and I (I_i)) and 6 are anti-site occupations (MA_{Pb}, MA_I, Pb_{MA}, Pb_I, I_{MA}, and I_{Pb}) [226, 241]. The anti-site occupation defects were predicted as deep-level states with high formation energies [242, 243] and hence will not contribute to a broader extent to non-radiative recombination [226, 241, 244]. The shallow defects have low formation energies and were considered to reduce the V_{OC} [245]. In general, for a solar cell under illumination, V_{OC} is determined by considering the splitting of electron quasi-fermi level (E_{Fn}) and hole quasi-fermi level (E_{Fp}) [246]. Defect density influences the Fermi level Shifting and pinning. When a perovskite absorber is considered with shallow traps (at E_T energy level) located below CB, E_{Fn} will be pinned near E_T. Similarly, E_{Fp} will be pinned near E_T if located at VB. Hence, V_{OC} governed by the splitting of E_{Fn} and E_{Fp} will decrease at high-density shallow traps. Shallow traps dictate the energy level alignments at absorber/E(H)TL interfaces[245, 246]. Hence, shallow traps at VB and CB with a narrowly distributed density of states (DOS) are preferable to increase the quasi-Fermi level (E_{Fn}) of light-induced electrons and decrease V_{oc} losses [247].

Suppose the absorber comprises unintended shallow defects at band edges with auxiliary electronic states at normal temperature. In that case, the defects can ionize and serve as acceptors or donor states doping the semiconductor. A high profile of deep defects in the bulk or at interfaces can pin the Fermi level restricting the doping control over the electric field distribution [248]. The primary decay process, defect assisted SRH recombination, causes substantial efficiency loss owing to the recombination of minority carriers.

The schematics of trap-assisted defects that act as recombination centers close to CBM and VBM are depicted in Fig. 4.7. It shows the condition when donor defects are occupying the interface states. Donor defects act as n-type doping, which leads to the junction of the p-n^+ type. This will cause the band to bend in the lower doped p side absorber. If the acceptor's defects occupy the interface state, it will act as p doping, forming a p^+n - type junction. In such

a scenario, depletion width and band bending will shift to the n-type region. These band bending and depletion region width for the different interface defect scenarios are depicted suitably in Fig 4.7.

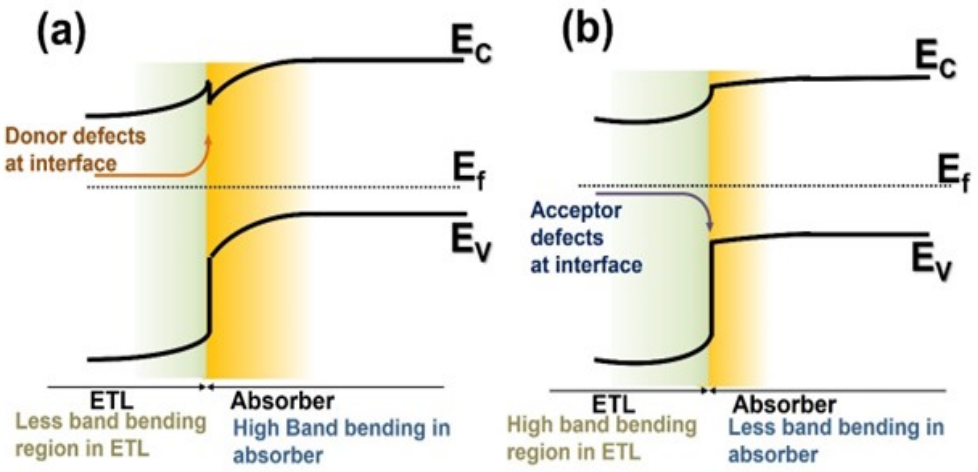

Figure 4.7 Energy band schematics showing the interface defects (a) occupied by donor defect and (b) occupied by acceptor defect.

$$R_{SRH} = \frac{C_n C_p (N_{trap} + P_{trap})}{C_n (n + n_1) + C_p (p + p_1)} (np + n_i^2) \quad (4.5)$$

$$n_1 = N_c \exp\left[-\frac{E_c - E_{trap}}{k_b T}\right] \quad (4.6)$$

$$p_1 = N_c \exp\left[-\frac{E_{trap} - E_v}{k_b T}\right] \quad (4.7)$$

Where N_{trap},P_{trap}, C_n, C_p are trap concentrations and of electron and hole capture coefficients, respectively and E_{trap} is trap energy.

Trap-assisted recombination is particularly efficacious whenever the trap is in mid-gap and may be used to classify the recombination dynamics for random distribution of traps at the mid-band gap [249] via Eq. (4.5-4.7). Consequently, it is imperative to minimize recombination loss at absorber/E(H)TL to augment the device performance. The deep transition level defects have higher formation energies. Hence, shallow defects are predominant in $MAPbI_3$ PSC.

Here we simulated the effect of shallow donor and acceptor defects at the interface on the overall device performance. The simulated band diagram for the donor defect occupying the interface states is depicted in Fig. 4.8 (a), and the acceptor defect occupying the interface states is depicted in Fig. 4.8 (b). As the absorber is p-doped, donor defects near the CBM have less probability of capturing the carriers, enhancing the device performance. In contrast, the

presence of acceptor defects has a greater probability of capturing the carriers and degrading the device's performance. Total and interface recombination that has occurred due to acceptor and donor defects is depicted in Fig. 4.9 (a-b), respectively. The acceptor defects engaging interface states decrease band bending in the absorber and the depletion region. In lieu, it happens in the ETL layer. A decrease in band banding and depletion region width lowers the V_{OC}. The device performance enhances efficiency for donor defects, as observed in Fig. 4.9 (c). The comparative J-V curve in Fig. 4.9 (c) shows the device performance with the donor and acceptor defects considering shallow interface states.

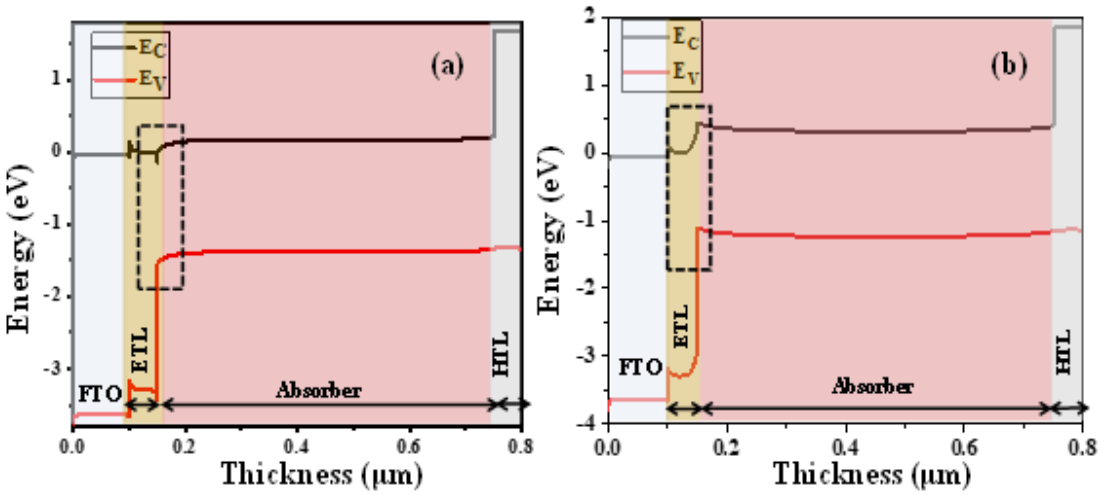

Figure 4.8 Energy band schematics for PSC with (a) donor defect and (b) acceptor defect occupying the interface states (perovskite/ETL).

The higher V_{OC} is perceived due to intense band banding and increased width of the depletion region in the absorber layer owing to the donor defects at interface states. The total and interface recombination with donor defects is less than that of the device possessing acceptor defects, as depicted in Fig. 4.9 (a-b), respectively. Additionally, the impact of defect density and the defect formation energy on the efficiency is depicted in Fig. 4.9 (d) concerning the donor defect. As the defect density increases, the trap-assisted defects will be more and provide more recombination centers for the carriers to be recombined, degrading the device performance.

The position of the trap-assisted defect concerning the formation energy also dramatically impacts the device's performance. To study this effect, we have varied the defect formation energy respective to the reference considered below E_C. When the formation energy is shallow, i.e., the presence of a trap-assisted defect is very close to the CBM. The probability of trapping the holes from the VBM is significantly less at the interface. As the defect's formation energy

increases, the trap-assisted defect's position moves towards the VBM. The defect will likely become a neutral charge by accepting the hole from the VBM. Therefore, it enhances recombination by decreasing the photo-generated carriers. Hence the device efficiency reduces drastically. Thus, the presence of donor defect near the CBM provides optimized efficiency with decreased recombination current.

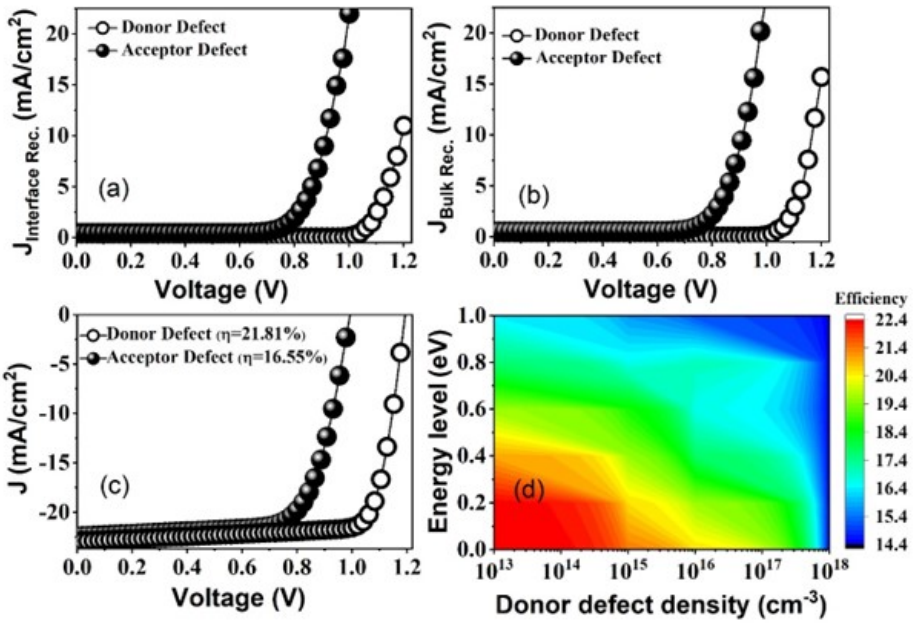

Figure 4. 9 Comparative (a) Interfacial recombination current for the device with donor defect, (b) Bulk recombination current for the device with acceptor defects. (c) J-V characteristics curve with acceptor and donor defects (d) 2D contour plot depicting the efficiency variation as a function of donor defect density and the defect energy level.

4.3.4 High hole doping in absorber near HTL interface

Concerning PSC, higher work function values and low surface recombination velocity (SRV) lead to increased solar cell efficiency [250-252]. This attributes to the fact that the barrier height of the majority carrier decreases with the increase in HTL work function value, which eventually makes semiconductor-metal contact near the ohmic type.

A highly doped p^+ layer at HTL/metal contact is simulated to reduce the contact resistance for Ohmic contact. We have implemented this effect by inserting a heavily doped thin (10 nm) layer of HTL (HDTHTL) by maintaining all other parameters constant, as depicted in Fig. 4.10 The comparative total recombination and interface current of the benchmark and HDTHTL devices are depicted in Fig. 4.11 (a-b), respectively.

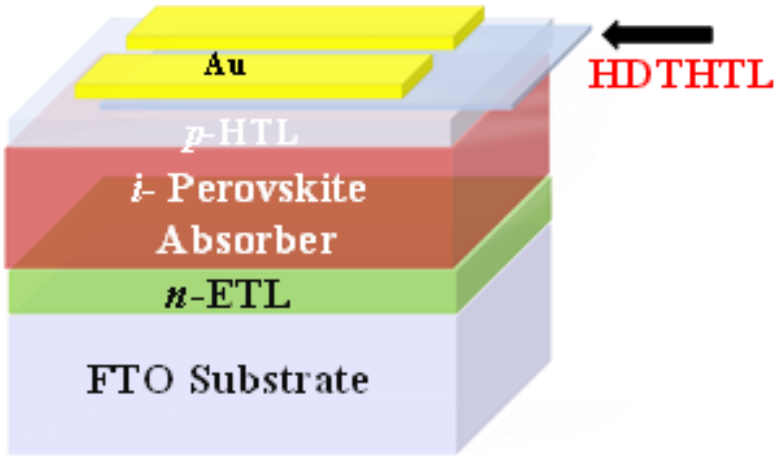

Figure 4.10 Device schematics with an inserted thin layer of heavily doped thin HTL (HDTHTL).

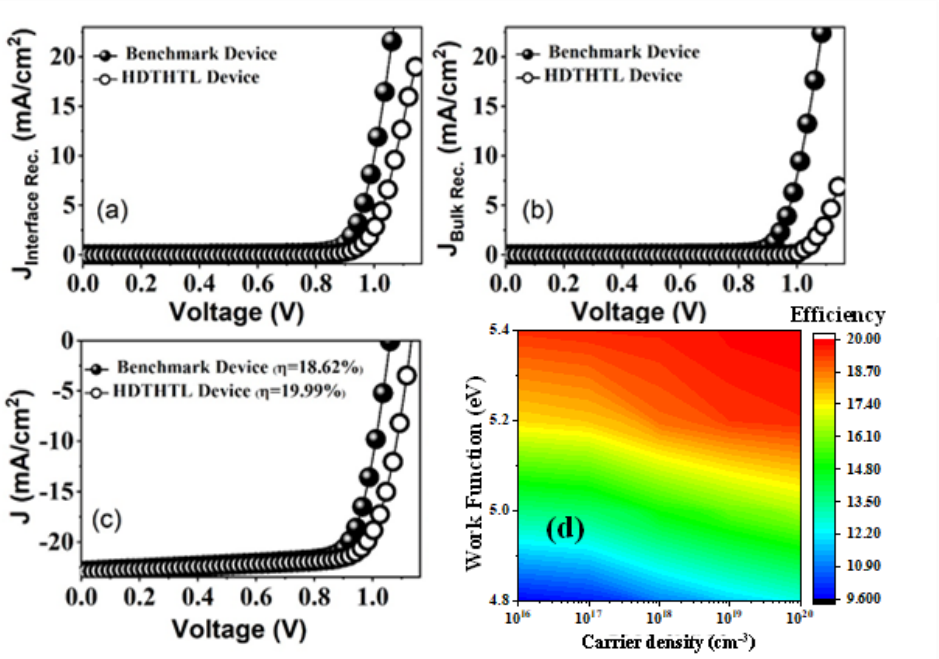

Figure 4.11 Comparative (a) Interfacial recombination current, (b) Bulk recombination current and (c) J-V characteristics curve of Benchmark and HDTHTL; (d) 2D contour plot depicting the variation of efficiency as a function of rear electrode work function and carrier density of HDHTL.

The efficiency is elevated in case of high hole doping with reduced recombination current as assimilated to the benchmark device. The high doping layer makes a near ohmic contact with metal. This situation generates a symmetric carrier profile, reducing the recombination at rear contact. The comparative J-V curve for the benchmarked device and modified HDTHTL device is depicted in Fig. 4.11 (c). The HDHTL device reported efficiency of 19.99% with reduced recombination.

Further, we investigated the impact of hole density on the metal contacts' work function. The requirement of high work function metal is perceived to be lowered when we have heavily doped HTL. The influence of the hole density and work function on the device's efficiency is depicted in Fig. 4.11 (d). Even at a low work function, efficiency is optimal when we have highly doped HTL.

The final optimized device architecture is depicted in Fig. 4.12. The performance parameters corresponding to the respective optimized methodology are tabulated in Table 4.2. The final optimized J-V curve, total and interface recombination currents are depicted in Fig. 4.12 (a-b). Our simulated results are compared with the experimental work reported previously and are summarized in Table 4.2.

Table 4.2 Performance Parameters for the optimized methodologies employed.

Optimization	**V_{OC} (V)**	**J_{SC} (mA/cm^2)**	**FF (%)**	**Efficiency (%)**	**Ref.**
Benchmark device	1.060	22.87	76.79	18.62	[22]
LPDTA	1.102	23.64	77.82	20.28	This work
HNDTA	1.12	22.72	75.70	19.39	This work
WBGTA	1.13	22.96	75.31	19.55	This work
Donor defect	1.19	22.93	79.70	21.81	This work
Acceptor defect	0.99	22.89	72.35	16.55	This work
HDHTL	1.13	22.93	76.23	19.81	This work
Optimized device	1.29	24.56	81.20	25.81	This work

In the literature, the best efficiency of 18.62 % has been achieved for PSC. It is evident from Table 4.2 that device modeling of PSC by incorporating LPDTA, WBGTA, HDHTL and considering donor defects beneath the CBM has an effective influence on the optimization of device performance by increasing the efficiency of V_{OC}, FF and decreasing the interface recombination. The final optimized device is achieved by incorporating all the methods (LPDTA, WBGTA, HDHTL, donor defect), which has increased efficiency, FF and V_{OC} by 38.61%, 5.5%, 21.69%, respectively.

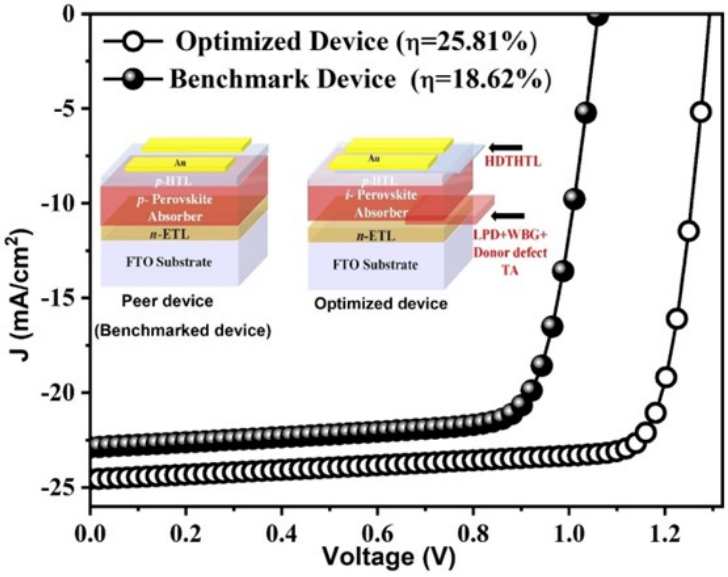

Figure 4.12 The final comparative JV characteristics curve of benchmark and optimized device. The performance parameters such as Efficiency, V_{OC}, J_{SC} and FF all improved in the optimized device. Inset shows the benchmark device and the optimized device configuration.

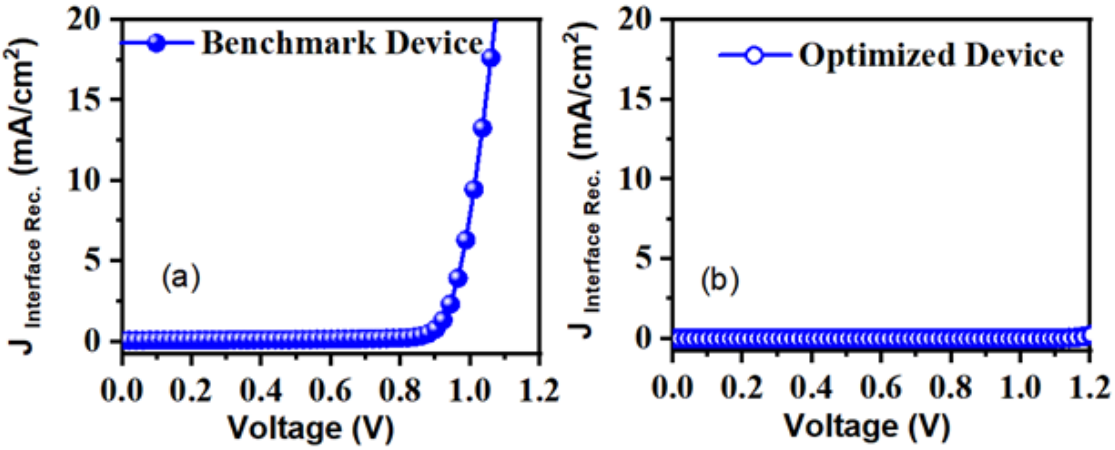

Figure 4.13 (a) The interfacial recombination current in the benchmark device. (b) The reduced interface recombination current in the optimized device after incorporating modification of LPDTA, WBGTA and HDHTL.

Table 4. 3 Performance Comparison and Recommendations

Parameter	Best achieved metrics	Suggested Control Parameters
V_{OC}	1.3248 V	Improve interface quality using LPDTA.
J_{SC}	22.93 mA/cm²	Enhance light absorption and minimize parasitic resistances.
FF	79.39%	Optimize charge transport layers and back contact work function.
PCE	23.22%	Implement defect passivation and ensure high shunt resistance.

Table 4.3 synthesizes the recommendations from the best achieved metrics, experimentalists can identify critical areas for optimization. Improving interface quality, optimizing doping profiles, managing defects, ensuring high shunt resistance, and fine-tuning the back contact work function are key strategies. These recommendations are expected to drive significant advancements in PSC performance, paving the way for achieving efficiencies comparable to, or exceeding, the simulated metrics. Through these insights, the chapter not only enhances our understanding of $MAPbI_3$-based solar cells but also provides a robust framework for experimentalists to enhance the efficiency and stability of PSCs.

4.4. Outcomes

- *Reduced Recombination at Interfaces*: Implementation of various absorber optimization techniques successfully mitigated internal recombination at interfaces in the Perovskite Solar Cell (PSC) configuration. These techniques included LPDTA for achieving an asymmetric doping profile, WBGTA for widening the band gap in the absorber surface region, managing interface donor defects, and varying doping levels in the Hole Transport Layer (HTL).
- *Insights into Design Parameters*: The study provided valuable insights into the influence of design parameters, including carrier density, doping profile, and bandgap, on the recombination mechanism and overall photovoltaic action in the PSC.
- *Effective Reduction in Charge Carrier Recombination*: Results demonstrated that the recombination of charge carriers at the interface was notably decreased by reducing hole density in the absorber vicinity through LPDTA. Additionally, the increased interface recombination barrier achieved by WBGTA further contributed to reducing recombination.
- *Beneficial Role of Donor Defects*: The study highlighted that band bending remained benign when interface states were occupied by donor defects as opposed to acceptor defects. This observation has significant implications for enhancing device performance.
- *Lowered Interfacial Recombination at HTL/Metal Contact*: The incorporation of a heavily doped thin hole transport layer (HDTHL) effectively lowered interfacial recombination at the HTL/metal contact, further contributing to improved device performance.
- *Optimized Device Efficiency*: By integrating all the absorber optimizations, the study achieved an optimized solar cell efficiency of 25.81%. This was complemented by a

high open-circuit voltage (V_{OC}) of 1.29 V, a fill factor (FF) of 81.20%, and a respectable short-circuit current (J_{SC}) of 24.56 mA/cm².

These outcomes collectively demonstrate the effectiveness of the implemented absorber optimization techniques in minimizing interfacial recombination and achieving a high-performance perovskite solar cell with significant implications for the advancement of photovoltaic technology.

4.5 Summary

In this chapter, we delved into the intricate realm of absorber optimization techniques aimed at elevating the performance of perovskite solar cells (PSCs) with a specific configuration of Au/HTL/Perovskite ($MAPbI_3$)/ETL/FTO. The paramount objective was to mitigate internal recombination at interfaces, a critical factor influencing the efficiency of PSC devices. Through meticulous analysis, we scrutinized the role of pivotal design parameters such as carrier density, doping profile, and bandgap in governing recombination mechanisms and overall photovoltaic action in PSCs. One of the central strategies employed was the integration of LPDTA at the absorber/ETL interface, effectively achieving an asymmetric doping profile. Additionally, we leveraged the WBGTA technique to widen the band gap in the absorber's surface region. These techniques collectively contributed to a substantial reduction in charge carrier recombination at the interface, a crucial advancement for enhancing device efficiency.

Our investigation revealed a critical insight regarding the impact of defects on band bending within the PSC device. Notably, we observed that when interface states were occupied by donor defects rather than acceptor defects, band bending remained benign. This discovery holds profound implications for minimizing recombination and optimizing the fill factor (FF) in PSCs. Furthermore, we meticulously examined the sensitivity of FF to the shunt resistance of the device. Our findings underscored the imperative of a shunt resistance surpassing 5 $K\Omega cm^2$ for achieving optimal FF, open-circuit voltage (Voc), and overall efficient device performance. Additionally, we delved into the influential role of the back contact work function in optimizing FF, emphasizing its capacity to reduce recombination and fine-tune FF in the PSC device.

By synthesizing these derived design parameters, we successfully engineered an optimized PSC device. This pinnacle achievement demonstrated a marked improvement in performance metrics, boasting a Voc of 1.3248 V, short-circuit current (Jsc) of 22.93 mA/cm^2, FF of 79.39%, and power conversion efficiency (PCE) of 23.22%. This chapter represents a significant stride forward in comprehending the intricate interplay of performance parameters with the absorber

configuration of $MAPbI_3$-based solar cells. The insights gleaned offer actionable guidance for the design and optimization of PSCs, promising enhanced efficiency and stability. This work not only paves the way for future research but also provides a blueprint for advancing renewable energy technologies through identified parameters and optimized designs.

CHAPTER 5

Bandgap Graded Perovskite Solar Cell for Above 30% Efficiency

In this chapter, we delve into an intriguing concept bandgap grading to enhance the light-absorbing capabilities of the perovskite absorber material. The idea involves adjusting the bandgap within a range of 1 to 2 eV through variations in stoichiometry. The ultimate objective is to achieve an efficiency that comes close to the SQ limit of pristine absorber device. Our exploration includes a detailed analysis of linear bandgap grading, considering different profiles of the absorber conduction band slope. Throughout this process, we aim to optimize device performance, account for defect tolerances, and maximize optical absorption.

Remarkably, our findings confront the notion that a wide range of bandgap grading is necessary for optimal efficiency. Instead, we discover that a well-optimized small range, specifically between 1.4 and 1.2 eV at the two ends of the absorber layer, can result in an impressive 31% power conversion efficiency. This innovative approach not only pushes the boundaries of perovskite solar cell performance but also highlights the importance of precise tuning for achieving optimal outcomes.

5.1 Introduction

Currently, perovskite solar cells are being investigated with great scientific interest for stabilizing the performance [253] and enhancing the efficiency beyond Shockley Queisser (SQ) limit [103]. The optimization of the perovskite material composition might augment spectrum absorption resulting in high device performance, thus needs to be investigated with great scientific interest.

In this regard, bandgap engineering of perovskite materials enables wide absorption of the spectrum. Moreover, a range of different bandgaps is obtained by compositional engineering of ABX_3 perovskite semiconductors, where methylammonium (MA) [254, 255], formamidinium (FA) [256], and Cesium (Cs) [257] are commonly utilized as monovalent A-cations within the perovskite lattice. In addition, higher bandgap perovskite absorbers have been realized through halide alloying [258]. Contemporary literature demonstrated the potential to obtain desired absorption onsets in hybrid perovskites by [259] alloying of metal halide perovskites. In this chapter, we proposed a configuration of PSC employing its wide bandgap tuneability to numerically examine PCE performance. We compared the experimental device performance metrics such as the power conversion efficiency, the short circuit current, fill-factor (FF), and the open-circuit voltage of single-junction devices as a function of the

bandgap profile of the perovskite absorber to assess various grading configurations to achieve PCE beyond SQ limit of pristine absorber device. Moreover, we have analyzed and highlighted the performance enhancement in engineering hybrid perovskite-based solar cell device technology for bandgap tunability via compositional grading.

5.2 Guidelines for Bandgap graded solar cells

The schematic of the inverted planar p-i-n configuration of the PSC device with a single uniform bandgap throughout its thickness is shown in Fig. 5.1(a). A solar cell device with a single bandgap could only absorb photons of energy greater than or equal to the bandgap of the absorber layer material. Conversely, a variable bandgap absorber could efficiently utilize the spectrum as shown in Fig 5.1 (b), reducing the thermalization and non-absorption losses in the device [260, 261]. This would lead to a higher J_{SC} value resulting in efficiency beyond the SQ limit. The schematic of the bandgap graded p-i-n configuration of the perovskite device is shown in Fig. 5.1 (b). The optimal band gap grading addresses the major losses in SQ limit i.e., thermalization and non-absorption, and could harvest all the visible region photons that are incident on the device [262]. Thermalization and non-absorption are the major losses in the detailed balance limit, combinedly responsible for 50% loss. Thus, rectifying them will result in a device with about 50% efficiency [263]. Seeing these advantages, bandgap grading is experimentally attempted in perovskite absorbers showing absorption and carrier collection enhancement. The position-dependent bandgap has an in-built electric field that will have directional carrier drift thus resulting in higher carrier mobility, reduced recombination velocity, and higher carrier collection [208]. For carrier collection enhancement, if the bandgap profile is considered at the two ends as 1 and 2 eV respectively, it provides an inbuilt slope ΔE_C = 1 eV, assuming the length of the absorber to be 0.6μm in linearly graded perovskite layer, the quasi-electric field ($\varepsilon = \Delta E_C/\Delta X$) caused by grading ($\Delta E_C$ = 1 eV) will be approximately around 10^6 eV/m. This additional drift field is favorable for carrier collection at the hetero-junction and lowers the electron-hole recombination in the bulk absorber. The proposed bandgap graded design will have a new effective recombination velocity for carriers in the engineered device ($S_{n\,eff}$), which can be estimated from the Eq. (5.1).

$$S_{n\,eff} = S_n - \mu_n \varepsilon \qquad (5.1)$$

where μ_n is the electron mobility, S_n represents the recombination velocity of the conventional design and ε is the electric field that occurred from the use of the graded band-gap profile given by [208].

With variable bandgap at the front and rear of the absorber layer, the absorption co-efficient will change with the bandgap is given by Eq. (5.2).

$$\alpha_c = A(hv - E_{gmin})^{1/2} \quad (5.2)$$

we can write an expression that is valid for the whole range of photon energies and values of b as follows

$\alpha_{eff} = 0$ $\quad hv < E_{g\ low}$

$\alpha_{eff} = 2/3(\alpha_{c\ hv-Eglow} / (E_{ghigh} - E_{glow})$ $\quad Eg\ low < hv < (3E_{g\ high} - E_{g\ low})/2$

$\alpha_{eff} = \alpha_c$ $\quad hv < (3E_{g\ high} - E_{g\ low})/2$

We have chosen the front bandgap higher as this will be advantageous for the gradual absorption of lower energy photons throughout the absorber layer. This scenario will have a quasi-electric field caused by grading in direction of the p-i-n electric field.

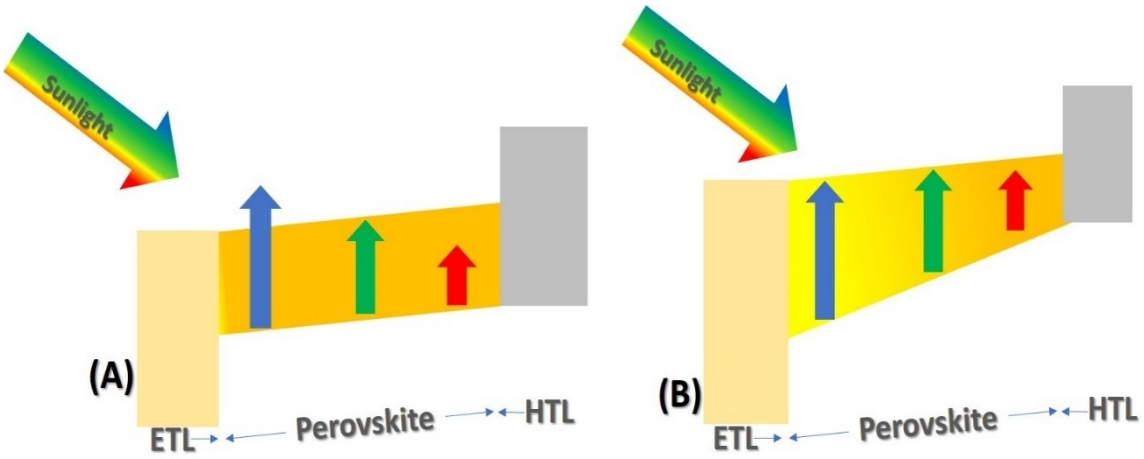

Figure 5.1 (a) The inverted planar p-i-n perovskite solar cell with a constant bandgap. The constant bandgap has non-absorption and thermalization loss as marked by the red and blue arrows. (b) The bandgap graded perovskite layer has efficient absorption of a photon. The variable energy photons marked by red, green, and blue arrows are efficiently absorbed.

One of the advantages of the perovskite is the tailoring ability of its wide bandgap depending upon the composition and stoichiometry. Halide (X), Metal (B), and A site variation in ABX_3 make hybrid organo-inorganic halide perovskite $MAPb(X_{1-x}X'_x)_3$ a highly tunable (bandgap) material, in which the bandgap can be modulated by changing the halide, A and B composition respectively [258, 264, 265]. Generally, B composition variation (by Sn doping and replacing Pb atoms), varies the bandgap from 1 to 1.5 eV, X site variation increases the bandgap from 1.5 to 3 eV [266]. Thus, providing a practically feasible way for bandgap adjustment by

incorporating doping [267, 268]. The empirical dependence of bandgap on each site composition is given by Eq. (5.3-5.5). For X (halide) site variation [266]

$$E_g(x)=E_g[ABX_3]+x(E_g[ABX'_3]- E_g[ABX_3]-b)+bx^2 \quad (5.3)$$

For B (metal) site variation[192]

$$E_g(x)=(1-x)E_g[ABX_3]+xE_g[AB'X_3]-bx(1-x) \quad (5.4)$$

The relation between the bandgap (E_g) and the composition of the perovskite based on the formula of $Cs_aFA_bMA_{(1-a-b)}Pb(Cl_xBr_yI_{(1-x-y)})_3$ is given below [269]

$$E_g = 1.587 - 0.039a - 0.102b + 1.543x + 0.669y \quad (5.5)$$

Where a, b are compositions for A site variation, x, y are compositions of doped halide. If we considered only halide doping leaving A and B cations of perovskite constant, then the Eq. reduces to $E_g = 1.587 + 0.669y$ (where y is the doping concentration of bromine). The bandgap engineering is reported for perovskite via composition variation of Sn and Br in $MASn_xPb_{1-x}(Br_xI_{1-x})_3$. We have obtained various stoichiometry by varying the composition (x, y) in the perovskite absorber layer with the bandgap range from 1 to 2 eV. The wide variation of bandgap (from 1-3 eV) in perovskite with variation in B site and X site is shown in Fig 5.2.

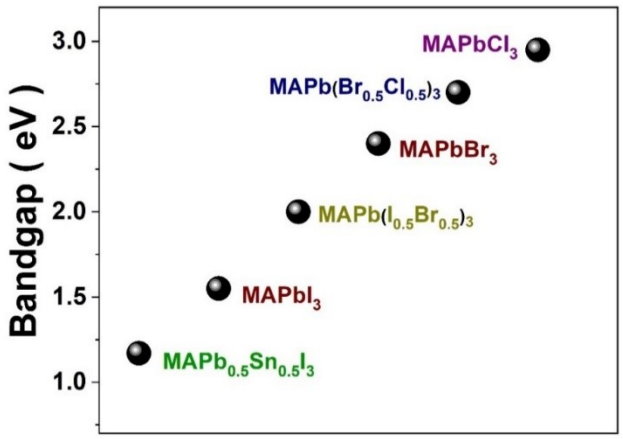

Figure 5.2 The wide variation of bandgap in perovskite with variation in composition. B site variation can tune bandgap in the range from 1.17-1.5eV whereas the X site variation has bandgap variation in the range 1.5- 3eV. [23-24].

5.3 Proposed configuration and modeling approach

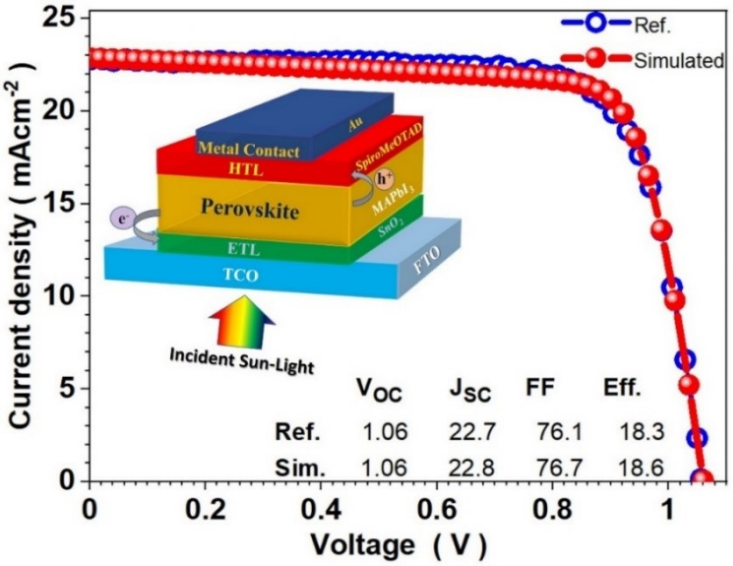

Figure 5.3.The J-V plot for our simulated device (as marked by spheres) benchmarked with the experimental device (as marked by an open circle) taken from reference [260]. Inset shows the schematic of inverted-planar/superstate perovskite solar cell (p-i-n configuration) as utilized in simulation.

Table 5.1 Device parameters as used in simulation [190, 192, 193, 270]

Material parameter	FTO	SnO_2	$MAPBI_3$	Spiro-MeOTAD
Thickness (µm)	0.1	0.05	0.6	0.05
Bandgap (eV)	3.6	3.3	1.55	3
Electron affinity (eV)	4.2	4	3.9	2.45
Dielectric permittivity (eV)	9	9	6.5	3
CB effective density of states (cm^{-3})	10^{18}	$1.2*10^{18}$	$2.76*10^{18}$	$2.8*101^{9}$
VB effective density of states (cm^{-3})	10^{18}	$1.8*10^{18}$	$3.90*10^{18}$	101^{9}
Electron mobility (cm^2/Vs)	200	100	5	$2*10^{-4}$
Hole mobility (cm^2/Vs)	100	25	5	$2*10^{-4}$

Donor density ND (cm^{-3})	$5*10^{18}$	10^{18}	0	0
Acceptor density NA (cm^{-3})	0	0	$2*10^{13}$	10^{17}
Absorption coefficient (cm^{-1})	10^5 [271]	10^5 [272]	10^5[271]	10^5 [271]

Defect model		
Total defect density (cm^{-3})	$8*10^{16}$	$5*10^{10}$
Defect type	Donor	Acceptor
Energetic distribution	Uniform	Uniform
Reference energy level	Above the Highest E_V	Above the Highest E_V
Capture cross section of electron (cm^2)	10^{-19}	10^{-19}
Capture cross section of hole (cm^2)	10^{-19}	10^{-19}

A planar heterojunction halide PSC is replicated theoretically by employing a solar cell capacitance simulator (SCAPS-1D). It solves electrostatic Poisson eq., drift-diffusion, and continuity eq. at the junction under various illumination and biasing conditions to simulate J(V), C(V), and C(f), quantum efficiency curve, band diagram, recombination current, etc. across p-i-n heterojunctions optoelectrical solar cell device. Applying relevant boundary conditions at the interfaces and different contacts, SCAPS solves the coupled differential equations in (Ψ, n, p) or (Ψ, E_{Fn}, E_{Fp}).

$$J_n = -\frac{\mu_n n}{q}\frac{dE_{Fn}}{dx} \tag{5.6}$$

$$J_p = \frac{\mu_p p}{q}\frac{dE_{Fp}}{dx} \tag{5.7}$$

$$-\frac{dJ_n}{dx} - U_n + G = \frac{dn}{dt} \tag{5.8}$$

$$-\frac{dJ_p}{dx} - U_p + G = \frac{dp}{dt} \tag{5.9}$$

$$\frac{d}{dx}\left(\varepsilon_0\varepsilon_r\frac{d\Psi}{dx}\right) = -q(p - n + N_D^+ - N_A^- + \frac{\rho_{def}}{q}) \tag{5.10}$$

where Ψ is the electrostatic potential, ε_0, ε_r is the permittivity of vacuum and semiconductor, n and p are the respective carrier density and N_D^+, N_A^- is the density of donors and acceptors, ρ_{def} is the charge density of defects, J_n, J_p is the respective electron and hole current density, E_{Fn}, E_{Fp} is the electron and hole Fermi level $\mu_{p/e}$ is the hole/electron mobility, G is the generation rate, U is the recombination rate. Eq. (5.6&5.7) are the charge carrier transport, and Eq. (5.8&5.9) are the electron- and hole-continuity equations; Eq. (5.10) is the Poisson equation. SCAPS can replicate experimentally observed phenomena in solar cell devices such as light soaking, impurity photovoltaic effect, multijunction, tunneling effect, J-V hysteresis, bandgap grading, etc. using appropriate conditions, defect models, script files, recorder setup, etc. We performed benchmarking of our numerical device with an experimentally reported device [194].

The simulated device has all device parameters reasonably matching with the experimental device i.e., superstate configuration of (FTO/ETL/perovskite-absorber layer/HTL). Tin Oxide (SnO_2, bandgap of 3.3 eV) is used as an electron transport material and Spiro-OMeTAD (bandgap of 3 eV) is used as a hole transport material. In addition, methylammonium lead halide ($CH_3NH_3PbI_3$) (bandgap of 1.55 eV) is used as an absorber layer. Fluorine doped tin oxide is used as a window layer along with gold (Au) as anode contact. The initial parameters that are required to simulate the device structure in SCAPS viz., the thickness of the layers, electron affinity, density of carriers, interfacial and bulk defect density are used as reported in the previous literature and are summarized thoroughly in Table 5.1. Initially, we simulated the performance parameters of the device configuration as shown in the inset of Fig. 5.3 and matched it with an experimental device that reported an efficiency of 18%. Fig. 5.3 shows the J-V curve of the simulated device along with the experimental device. The overlapping of the two J-V plots reveals that the simulated device corroborates well with the experimental device. The experimental data is collated from [271] by using GetData™. The simulated device has performance parameters values, efficiency, V_{OC}, $J_{SC,}$ and fill factor of 18%, 1.06V, 22mA/cm^2, and 76% respectively that provide the precise matching with the experimental device. In this configuration of the matched device, we have incorporated and analyzed the bandgap grading [194, 271, 273].

5.4 Results and discussion

The linearly graded bandgap of perovskite solar cell, with the different slopes of absorber band levels, is represented in Fig. 5.4. The difference of the bandgap at the two ends is given by $E_{g\ High} - E_{g\ Low}$. Initially the front side of the bandgap, $E_{g\ High}$ is fixed at 2 eV and the rear edge of

the bandgap $E_{g\ Low}$ is fixed at 1eV. The Pb-based $MAPbX_3$ has a bandgap of 2 eV and Sn-based $MASnX_3$ has a bandgap of ~1.17 eV. We observed the differential slope of the conduction band E_C and the valence band E_V upon variation of bandgap at one of the ends while keeping fixed the other end bandgap as depicted in Fig 5.4. This slope in the conduction band level provides an additional drift for photogenerated electrons in the conduction band and hole in the valence band. In addition, the highly doped HTL, ETL layer provides built-in voltage throughout the intrinsic layer and the bandgap grading provides an additional drift field. The higher bandgap can be seen toward the front, ETL which is also the illuminated side and has a gradual decrease throughout the length of the absorber. It can be concluded that the higher energy photons are absorbed in the front and the lower energy photons are absorbed in the lower bandgap end at the rear side (HTL), thus leading to maximized absorption. An efficient bandgap grading requires the front and back contact to be near ohmic contact to avoid Schottky junction formation by suitably taking suitable work functions of ETL and HTL layers.

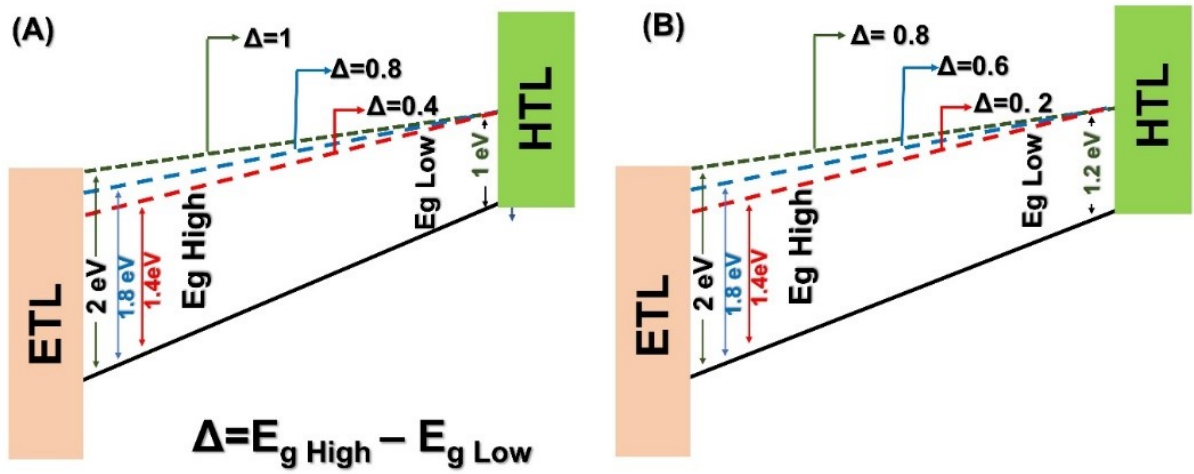

Figure 5.4 (a) Schematic of bandgap grading with E_g (high bandgap) variation at a fixed rear bandgap (E_g Low) of 1 eV. (b) The schematic of bandgap grading with E_g high bandgap variation at a fixed rear bandgap (E_g Low) of 1.2 eV.

The various grading profiles simulated are schematically shown in Fig. 5.4 (a-b). The rear bandgap is fixed at 1 eV and the front bandgap is varied from 2eV -1.4eV in a linear fashion as schematically shown in Fig. 5.4 (a). SCAPS can grade bandgap in various profiles such as linear, logarithmic, parabolic (two laws), power law, exponential, or any user-defined fashion. If the composition of the material is $A_{1-y}B_y$, SCAPS gives the user an option to define the

properties of the pure compounds named A and B, and the composition grading y(x) over the thickness of the layer: thus, defining the composition values y at the left and right side of the layer, and by specifying some grading law in between. All material properties (in this case bandgap, E_g) are then derived from the local composition parameter y(x), that is, $E_g[y(x)]$ is evaluated. Linear grading laws are utilized for the composition grading y(x) over a layer, as well as to set the composition dependence $E_g(y)$ of a property. Linear grading of the bandgap is given by $E_{gA}(Y_B\text{-}Y)+E_{gB}(Y\text{-}Y_A)/Y_B\text{-}Y_A$.

The schematic of the slope of the conduction band and valence band in the absorber in as shown in Fig 5.4 (b). The rear bandgap (E_{gLow}) is fixed at 1.2 eV and the front bandgap is varied from 2 -1.4eV in a linear fashion. We simulate rear bandgap (E_{gLow}) values of 1-1.4 eV. This is to maximize absorption of incident visible photons and drift field within the absorber layer.

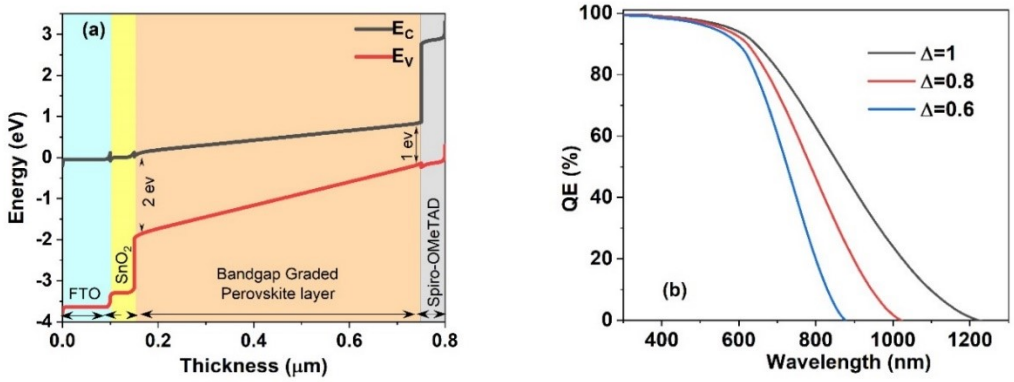

Figure 5.5 (a) The simulated band diagram of bandgap graded perovskite solar cell. It shows the variable E_g throughout the absorber thickness. (b) The simulated quantum efficiency of the device. The black line shows the QE for $E_{g\ Low}$ 1 eV and $E_{g\ high}$ 2 eV (Δ =1; $\Delta=E_{g\ High}-E_{g\ Low}$), and the red line shows the QE for $E_{g\ Low}$ 1.2eV and $E_{g\ High}$ 2 eV (Δ =0.8), the blue line shows the QE for $E_{g\ Low}$ 1.4 eV and $E_{g\ High}$ 2 eV (Δ =0.6).

The simulated band diagram is shown in Fig. 5.5 (a). This band diagram plot shows the actual slope of conduction energy level and valence band energy level, band banding profile across the perovskite layer, and interface offsets in the graded device. The quantum efficiency (QE) for the variable bandgap grading profile is simulated and shown in Fig. 5.5 (b). The higher QE for the bandgap grading shows a higher extent of spectrum absorption i.e., higher wavelength photons, and the difference between the high and low bandgaps at the two edges of the absorber layer is marked by Δ i.e., $\Delta = E_{g\ High} - E_{g\ Low}$. It can be observed that the QE is different for distinct Δ values.

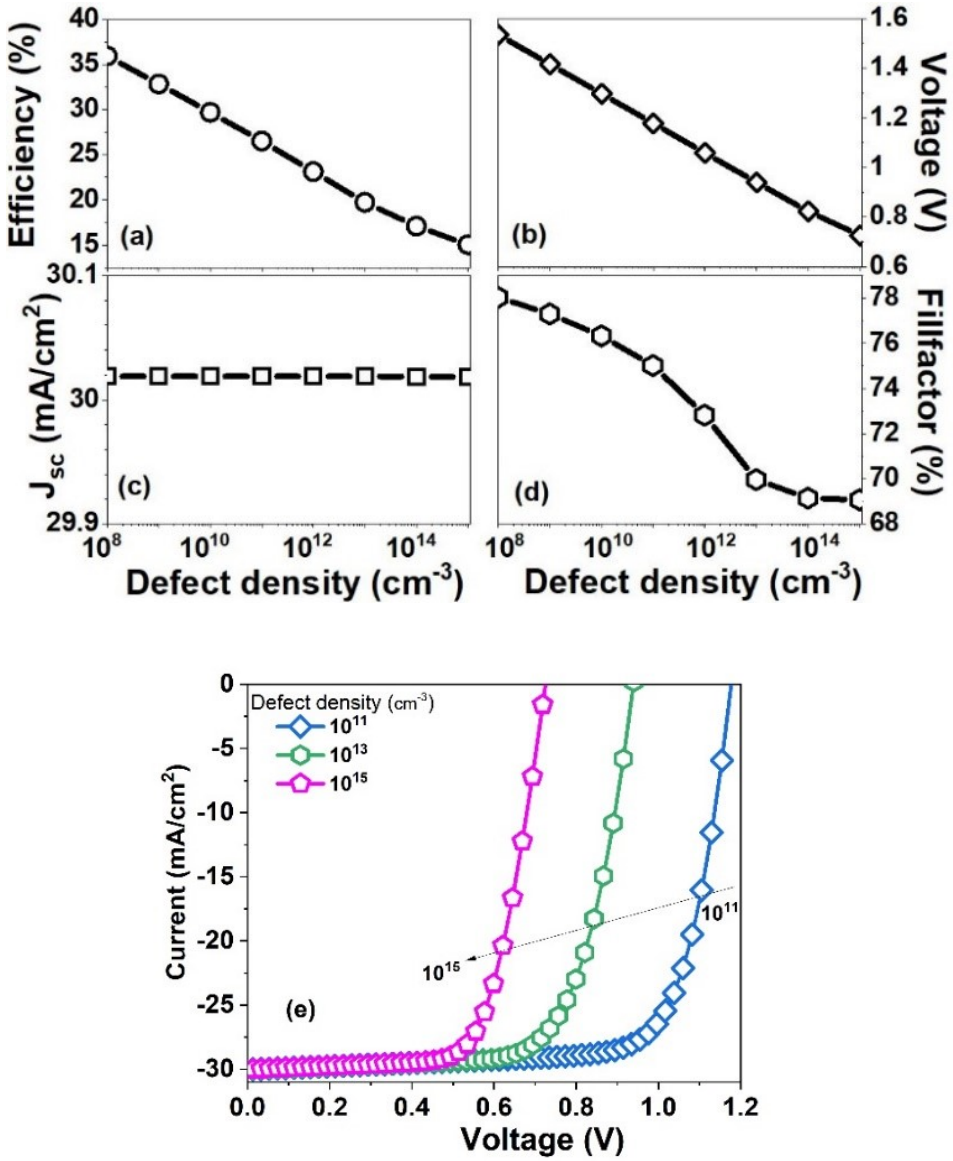

Figure 5.6 (a-d) The device performance as a function of bandgap graded PSC defect density. Efficiency V_{OC}, and FF falls steeply with defects. (e) The simulated J-V curve of the bandgap graded device as a function of bulk defect density.

The absorption of longer wavelength increases for different bandgap profiles depending on Δ, the wavelength range of 400-1200 nm, 400-1000 nm, and 400-880 nm for the bandgap pairs ($E_{g\ High}$ and $E_{g\ Low}$) of 2-1eV, 2-1.2 eV and 2 -1.4 eV respectively. It's been observed that the absorption onset reached a maximum for the bandgap grading with a low bandgap of 1eV ($E_{g\text{-}Low}$) and a high bandgap of 2 eV ($E_{g\text{-}High}$). This shows the response of wide bandgap perovskite to absorb the spectrum in the infra-red region and results in a high current generation. The quantum efficiency for the case of Δ= 0.6 is in good agreement with the general experimental result in the literature, with the absorption tail positioned in 885 nm wavelength for the bandgap in the range of 1.4 eV. The bandgap of 1.4 eV corresponds to 885 nm wavelength. Similarly,

the bandgap of 1.5eV corresponds to 826 nm wavelength. This is a persistent experimental observation in literature for $MAPbI_3$ with bandgap of 1.4-1.55 eV. In simulation when we took 1.4 eV bandgap in the grading profile, QE corresponds to 880 nm which matches with the general experimental data reported previously in literature. The bandgap grading in the lower bandgap region is enhanced at the spectrum absorption and this is suitable for achieving higher short circuit current.

Fabricating a variable composition layer for achieving a graded bandgap might result in some vacancies, substitution, or interstitial bulk defects. These defects can act as a recombination center and the higher defect density may decrease the lifetime of the charge carrier and increases the recombination rate. Therefore, the advantage of bandgap grading of PSC in the absorption of the spectrum is analyzed under bulk defect density variation. The device used for Fig 5.6 simulation has a bandgap grading profile of 2-1.2 eV at the two ends of device. We simulated this bandgap graded configuration under the impact of absorber bulk defect in the range 10^8 to 10^{15} cm^{-3}. The bandgap graded configuration shows strong sensitivity toward defect density as shown in Fig. 5.6 (a-d). The efficiency of the bandgap graded perovskite solar cell falls linearly with increasing defect density and for the lower defect density of 10^8 cm^{-3} efficiencies is reaching nearly 35% and drop to 15% for bulk defect density of 10^{15} cm^{-3}.

The presence of higher defect density leads to accelerated trapped assisted recombination and is evident by the voltage reduction to 0.8 V and by the fill factor (FF) degradation from 78% to 69% over the defect density variation of 10^8 to 10^{15} cm^{-3}. There is no significant change found in the short circuit current, J_{sc} concerning the defect density variation from 10^8 to 10^{15} cm^{-3}. J_{sc} is stabilized with the increasing defect density due to robust and increased absorption by the bandgap graded absorber layer pointing toward the advantageous charge collection provided by this configuration. The experimental defect density reported in the literature for the perovskite is of the order of 10^{11} cm^{-3} [15]. J-V curve under the influence of defect density variation for the graded configuration is represented in Fig 6. Bulk defect density in the range of 10^8 cm^{-3} is generally seen in crystalline silicon solar cells. The perovskites are semicrystalline and have reported defect density in the range of 10^{11} to 10^{15} cm^{-3}. It can be deduced from the simulation in Fig. 5.6 that the density of the defect above 10^{11} cm^{-3} has a significant impact on the performance of the PSC device. Fig. 5.6 (e) shows the simulated J-V curve for the device at various defect densities within the range 10^{11} to 10^{15} cm^{-3}.

A comparison of nongraded device and bandgap graded device under the influence of increasing defect density is shown in Fig 5.7. It is observed that the high efficiency of graded device is highly sensitive to defects. The efficiency falls from 38% to 15% under the influence of increasing defect density from 10^8 - 10^{15} cm^{-3}. For the non-graded device, the efficiency remains linear for low defect density and falls for higher defect density. At higher defect density bandgap graded device decay faster as compared to the non-graded.

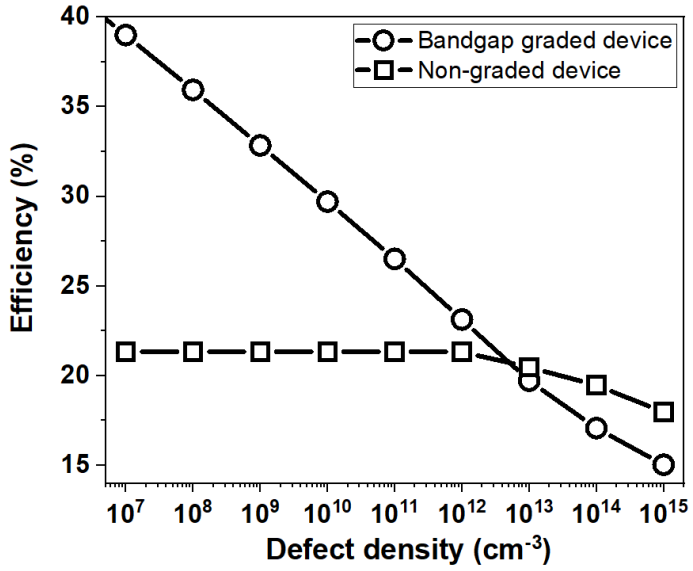

Figure 5.7 The comparative performance (in presence of increasing defect density) of graded PSC and non-graded device with single bandgap of 1.5eV.

To bring out the ideal profile of bandgap grading resulting in the optimal performance of the device, we optimized the bandgap grading configuration. The first configuration is shown in Fig. 5.4(a) where the rear bandgap is fixed at 1 eV and the front bandgap is made varied from 2 - to 1.4 eV. The impact of this profiling is analyzed for overall device performance. In the case of Fig. 5.4 (b), we have fixed the rear bandgap at 1.2eV and the wide front bandgap is varied from 2-1.4 eV. The impact of this variation is simulated, and optimized bandgap profiling is generated with optimal efficiency. We decreased the front wide bandgap and increased the lower rear bandgap to maximize the incident spectrum absorption. Fig 5.8 shows the contour plot for J_{SC} and efficiency as a function of different bandgaps for $E_{g\ High}$ (varied from2 - 1.4 eV), $E_{g\ Low}$ (varied from 1 - 1.4 eV). The obtained short circuit current is higher for the configuration having $E_{g\ Low}$ bandgap is 1 eV and $E_{g\ High}$ is 1.4eV respectively. The lower bandgap of the absorber tends to absorb most of the incident spectrum thus resulting in a higher current. However, a lower bandgap will have lower V_{OC} output and lower FF output. An optimized bandgap profiling is required where overall efficiency maximizes. In bandgap

grading, J_{SC} increase with lower Δ, however, other parameters such as V_{OC} and FF are observed to be decreasing with lowering Δ. With increasing Δ i.e., $E_{g\ High}$ - $E_{g\ Low}$, the conduction band slope (dE_C/dX) increases. For Δ = 1, ($E_{g\ High}$= 2, $E_{g\ Low}$=1) the slope is highest, but the J_{SC} values are not optimal, thus efficiency is not maximum for such large bandgap grading.

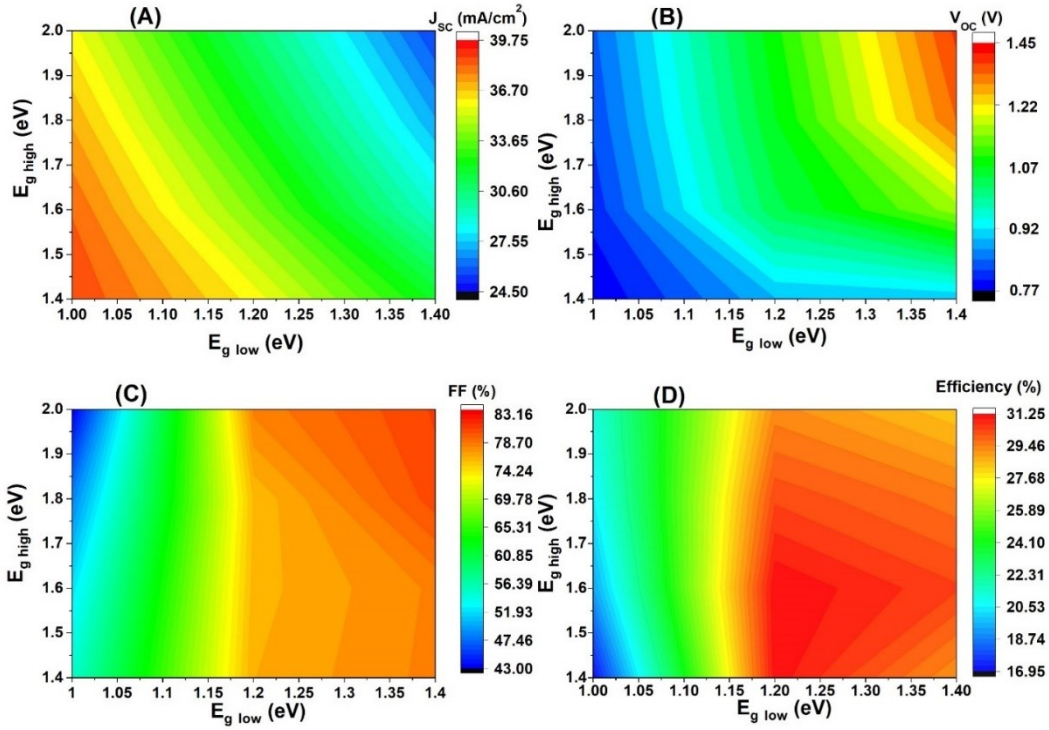

Figure 5.8 (a) The simulated J_{SC} parameters of the bandgap grading device as a function of bandgap grading in the absorber layer, when the high bandgap is varied from 2eV-1.4eV and the low bandgap is 1eV-1.4eV. (b-d) The contour plot of efficiency, V_{OC}, FF as a function of bandgap grading, when the high bandgap is varied from 2eV-1.4eV and the low bandgap is 1eV-1.4eV. The efficiency maximizes in the region when $E_{g\ High}$ is 1.4-1.6 eV and $E_{g\ Low}$ is 1.2eV.

In grading configuration efficiency is a trade-off between two competing parameters J_{SC} (required low bandgap), V_{OC} (require high bandgap), and FF (require high bandgap). A higher slope of grading might give a higher drifts field for higher Δ, but limits J_{SC} values as seen in Fig 5.8 (a). Thus, the bandgap at two ends of the absorber should be such that J_{SC} and V_{OC} should be optimal, and efficiency is maximized. The contour plot in Fig. 5.8 is evident that at fixed $E_{g\ Low}$ J_{SC} consistently reduces with lowering in $E_{g\ High}$ and efficiency maximizes in a narrow region where Eg low values are approximately 1.2eV and $E_{g\ High}$ values of 1.4eV. The optimal pair of bandgaps at the two ens achieving best efficiency and leading to optimal bandgap grading is $E_{g\ High}$ - $E_{g\ Low}$ = 1.4-1.2eV i.e a Δ = 0.2eV. This small value of the slope is achieving optimal efficiency as this value is achieving the best tradeoff among various competing factors. A higher power conversion efficiency of 31% has been observed for the bandgap grading from 1.4 – 1.2eV, while a PCE of

21% has been observed for the bandgap grading from 2 to 1eV. The perovskite absorber layer is graded from lower front bandgap to higher rear bandgap in the range 1 to 2 eV, the V_{oc} and FF decreased however a considerable enhancement has in the J_{sc}. Here the lower front bandgap is kept constant, and the higher rear bandgap is varied, generating a grading throughout the thickness of the absorber. With the initial bandgap grading from 2 to 1 eV, V_{oc} has been observed as 1.1 V and J_{sc} as 30 mA/cm^2.

As the higher bandgap is varied from 2 eV to the lowest value of 1.4 eV for which the value of V_{oc} changes minutely but J_{sc} has recorded a considerable enhancement in its value. The efficiency of the PSC graded in this methodology has shown an increase with a decrease in the higher bandgap. Power conversion efficiency reaches as high as 31.2% for the linear bandgap profile of 1.4 eV at the front bandgap and 1.2 eV at the rear bandgap side. This increase in the efficiency of the optimized device near to SQ limit is due to the efficient absorption of the spectrum resulting in higher PCE. Table 5.2 summarizes the various bandgap grading ranges with their corresponding efficiencies. A comparison with the single bandgap for the benchmarked device is made to highlight the efficiency improvement in the bandgap grading scheme.

Table 5. 2 Efficiency of band graded versus single bandgap PSC device.

Single bandgap PSC		**Bandgap graded PSC**	
Single bandgap (eV)	**Efficiency (%)**	**Bandgap Range (eV)**	**Efficiency (%)**
1	12.01	1-1.4	16.99
1.1	16.65	1-1.6	19.29
1.2	18.04	1-1.8	20.49
1.3	19.61	1-2	21.08
1.4	19.72	1.2-1.4	31.24
1.5	19.49	1.2-1.6	31.14
1.6	18.40	1.2-1.8	30.30
1.7	16.50	1.2-2	29.28
1.8	14.06	1.4-1.6	30.41
1.9	12.14	1.4-1.8	29.59
2	10.22	1.4-2	28.35

5.5 Outcomes

- Accurate Replication of Experimental Efficiency: Successfully reproduced an 18% efficiency in perovskite solar cell (PSC) through meticulous numerical analysis and parameter adjustments, closely aligning with experimental data.
- Bandgap Grading for Enhanced Performance: Implemented bandgap grading leveraging the tunability of perovskite materials, effectively optimizing the benchmarked device for superior spectral matching and enhanced carrier collection.
- Variable Bandgap Approach for improved Efficiency: Proposed a variable bandgap strategy, addressing the limitations of a fixed bandgap absorber, to achieve efficiency matching the Shockley-Queisser (SQ) limit of the pristine absorber device, showcasing the potential for significant efficiency gains.
- Critical Factors for Efficiency Improvement: Identified crucial parameters for bandgap grading optimization, emphasizing the importance of low bulk defect density (below 10^{11} cm^{-3}) and a well-defined bandgap grading profile.
- Optimal Bandgap Range for Peak Efficiency: Contrary to common assumptions, simulations revealed that a narrow bandgap variation range (1.4 to 1.2 eV) at the absorber ends yielded a remarkable power conversion efficiency (PCE) of 31.2%, emphasizing the significance of targeted bandgap engineering.

These findings underscore the potential for significant advancements in perovskite solar cell technology. The variable bandgap approach, coupled with meticulous consideration of defect density and bandgap grading, offers a promising pathway towards achieving efficiencies approaching the theoretical limits set by the SQ efficiency of pristine absorber device. This research contributes to the development of highly efficient and adaptable perovskite solar cells.

5.6 Summary

In this chapter, we conducted an extensive analysis and numerical reproduction of a high-efficiency perovskite solar cell (PSC) based on the experimentally reported efficiency of 18%. This approach involved careful selection of device parameters and defect models, resulting in a commendable alignment with the experimental device performance.

Exploiting the remarkable wide bandgap tunability inherent to perovskite materials, we implemented a bandgap grading modification strategy. This was aimed at fine-tuning the performance of the matched or benchmarked device. Recognizing the limitations of a single bandgap absorber in terms of spectral matching, we advocated for the adoption of a variable

bandgap approach. This not only demonstrated superior spectrum matching but also facilitated high carrier collection, ultimately driving the efficiency towards the SQ limit of the pristine absorber device. A detailed scrutiny of the critical parameters influencing bandgap grading ensued. Among these, the bulk defect density and the profile of bandgap grading emerged as pivotal factors. It was established that achieving a defect density lower than 10^{11} cm^{-3} is imperative to foresee any meaningful efficiency gain. To further elucidate the impact of different bandgap profiling scenarios, we conducted a thorough comparative analysis. This encompassed examination of varying bandgap ranges and slopes of the conduction band, shedding light on their influence on device parameters.

Contrary to conventional assumptions, these simulations provided compelling evidence that an extensive range of bandgap tunability is not a prerequisite for achieving maximum efficiency. Instead, we revealed that a judiciously optimized, modest range of bandgap variation from 1.4 to 1.2 eV at the two extremes of the absorber yielded an impressive power conversion efficiency (PCE) of 31.2%. This chapter not only offers a meticulous examination of the intricacies involved in achieving high efficiency in perovskite solar cells but also presents a groundbreaking variable bandgap approach that holds significant promise for advancing the field. The critical role played by defect density and bandgap grading profiles in determining efficiency underscores the importance of precise material engineering. This research represents a substantial step towards the realization of highly efficient and adaptable perovskite solar cells.

CHAPTER 6

Double Absorber Perovskite Solar Cells: Computational Insights and Optimization

This chapter introduces a cutting-edge advancement in perovskite solar cell design - the integration of a double absorber layer structure. This innovative configuration comprises a carefully engineered Narrow Bandgap Absorber (NBGA) adjacent to the Hole Transport Layer (HTL), and a Wide Bandgap Absorber (WBGA) positioned near the Electron Transport Layer (ETL). The NBGA, precisely tailored to efficiently absorb lower energy photons, demonstrates a remarkable capacity for harnessing sunlight in the infrared spectrum. Simultaneously, the WBGA, optimized to capture higher energy photons in the visible and ultraviolet range, significantly expands the cell's absorption capabilities. This strategic combination empowers the solar cell to leverage a broader spectrum of incident light, thus enhancing its overall energy conversion efficiency. Further we utilized the Random Forest algorithm to develop predictive models for efficiency estimation in perovskite structures. Leveraging a dataset of 3800 samples, each characterized by 20 input features and four attributes, our accurate predictions underscore the effectiveness of the RF algorithm in capturing complex relationships between input parameters and resulting efficiency.

This research not only advances the understanding of solar cell engineering. The findings of this study hold great promise for the continued development and deployment of perovskite solar cells, marking a significant stride towards a more sustainable energy future.

6.1 Introduction

The double absorber layer structure is demonstrated to achieve high efficiency. The integration of a double absorber layer in perovskite solar cells offers advantages beyond single-layer counterparts. Double absorber layered perovskite solar cells expand spectral absorption with two distinct bandgap absorber layers, reducing thermalization losses and minimizing carrier recombination for improved power conversion efficiency. A protective wide bandgap layer enhances stability, while their adaptability and integration potential promise efficiency and reliability advancements in photovoltaic technology.

The Double Absorber Layer Concept involves the integration of two distinct perovskite absorber layers within a single solar cell. These layers are carefully composed to have specific bandgap properties. The first absorber layer typically consists of a Narrow Bandgap Absorber (NBGA), which has a bandgap optimized for absorbing low-energy photons (longer wavelengths) from the solar spectrum. This allows it to efficiently capture a significant portion

of sunlight, particularly in the infrared range. The second absorber layer incorporates a Wide Bandgap Absorber (WBGA), which is designed to absorb high-energy photons (shorter wavelengths). This ensures that the solar cell can also harness the higher energy photons in the visible and ultraviolet range of the spectrum. Surrounding these absorber layers are the ETL and HTL. These layers play crucial roles in facilitating the movement of charge carriers (electrons and holes) within the solar cell.

The NBGA is typically composed of a perovskite material with a bandgap optimized to absorb lower energy photons. This is achieved by adjusting the composition of the perovskite, often involving the inclusion of specific elements or doping to tune the bandgap. The NBGA is positioned adjacent to the HTL. This placement ensures that holes generated in the NBGA can easily access the HTL for efficient collection and transport. The WBGA is fabricated with a perovskite material that has a wider bandgap. This allows it to effectively absorb higher energy photons from the solar spectrum. The WBGA is positioned closer to the ETL in the cell structure. This placement ensures that electrons generated in the WBGA have a shorter path to the ETL for efficient extraction and transport.

The primary function of the NBGA is to absorb lower energy photons, which predominantly fall in the infrared region of the electromagnetic spectrum. This region constitutes a significant portion of sunlight. By efficiently capturing these low-energy photons, the NBGA ensures that the solar cell maximizes its utilization of solar energy. The WBGA is designed to absorb higher energy photons, mainly in the visible and ultraviolet regions of the spectrum. By incorporating the WBGA, the solar cell can effectively harvest the energy from higher energy photons, further enhancing the overall efficiency. The Double Absorber Layer Concept strategically integrates a NBGA and a WBGA within a perovskite solar cell. These layers are positioned between the ETL and the HTL. This configuration maximizes the cell's ability to capture a wide range of solar photons, optimizing overall efficiency.

Selecting two bandgap systems for photovoltaic applications involves critical constraints such as material compatibility, band alignment, thermal stability, absorption properties, and interface quality. Ensuring lattice matching is essential to minimize defects and improve efficiency, as lattice mismatch can lead to recombination centers [274]. Proper band alignment facilitates efficient charge carrier separation [275], while thermal stability ensures materials maintain their properties under operational conditions. Bandgap engineering allows for the tuning of materials' electronic properties to optimize light absorption and carrier transport [276].

Complementary absorption spectra maximize solar spectrum utilization, enhancing device efficiency [277]. Interface engineering techniques like surface passivation reduce defect density, improving performance [278].

The incorporation of machine learning [279] aids in easing to find out the suitable pairs to form a double absorber by deciphering complex relationships between input parameters and efficiency, enabling predictive modeling, optimization, and accelerated advancements in their design and performance. The Random Forest (RF) algorithm is a versatile machine learning technique that combines multiple decision trees to enhance predictive accuracy and mitigate overfitting. It operates by constructing a multitude of decision trees during training and making predictions based on the majority vote of these individual trees. Random Forests are well-suited for both classification and regression tasks, offering robustness and flexibility in handling complex datasets [280]. In the realm of perovskite solar cell research, MATLAB proves instrumental in preprocessing experimental data, training and evaluating ML models, and optimizing hyper parameters. The platform's capabilities are harnessed to predict material properties, optimize device architectures, and enhance solar cell performance. By leveraging MATLAB, researchers can unravel the complexities of perovskite solar cells more efficiently, leading to advancements in efficiency, stability, and performance prediction.

6.2 Modeling the Device Structure

A novel and distinctive approach can be adopted by amalgamating the pivotal advantages of both the 2D-3D structure and the 2D-3D conversion process. This approach promotes the integration of a double-layer perovskite structure, meticulously composed of two perovskite absorber layers enclosed between an ETL and HTL. One of these absorber layers serves as a narrow bandgap absorber (NBGA), while the other performs as a wide bandgap absorber (WBGA). The implementation of this proposed structure can be implemented in two stages: firstly, by the establishment of a 2D-3D synergy structure [281], followed by the conversion of the 2D absorber within the second absorber layer into a 3D absorber [282]. The culmination of these processes can yield a sophisticated double absorber layered perovskite solar cell characterized by a 3D/3D configuration. Moreover, the realization of this structure can also be achieved through sequential spray deposition, as elaborated in [283]. The utilization of these techniques imparts flexibility in designing and can be tailored to accommodate different types of absorbers, addressing the need for diverse material considerations.

The performance improvement of $MAPbI_3$ is simulated by considering the 12 different perovskite absorbers as the second layer to create double absorber layer structure. The PCE of all single absorber layers is tabulated in Table. 6.1. Stacking of two absorber layers with different bandgaps results in a broader overall absorption range and increased efficiency, as each layer absorbs a different portion of the solar spectrum. Additionally, the use of a NBGA layer on top of the WBGA layer can minimize the loss of high-energy photons due to thermalization, resulting in an improved V_{OC}. Fig. 6.1 depicts the device structure of the double absorber layer i.e., narrow band absorber and wide band absorber laid on top of each other sandwiched between ETL and HTL. This structure has a two-stage absorption process that enhances the device efficiency as it can capture a broader range of solar photons and convert them into electrical energy. The schematic of energy level diagrams of all 13 perovskite absorbers used for the study is depicted in Fig. 6.2. The perovskite absorbers $MAGeI_3$ (1.9 eV), $MAPbBr_3$ (2 eV), $MASnBr_3$ (2.15 eV), $CsPbI_3$ (1.73 eV), $CsSnGeI_3$ (1.6 eV), $CsPbBr_3$ (2.3 eV), $CsSnBr_3$ (1.64 eV), $CsSnCl_3$ (2.97 eV) forms wide band gap (WBG) counterparts with $MAPbI_3$ (1.55 eV) and are termed as wide bandgap absorbers (WBGA) in further discussion.

Table 6.1 Single absorber perovskite solar cell device power conversion efficiencies from literature.

Absorber Material	**PCE (%)**	**Ref.**
$MAPbI_3$	20.22	[284]
$MASnI_3$	22.30	[285]
$MAGeI_3$	21.62	[286]
$MAPbBr_3$	10	[287]
$MASnBr_3$	8.38	[193, 288]
$CsPbI_3$	19	[289]
$CsSnI_3$	26.4	[290]
$CSGeI_3$	17.26	[291]
$CsPbBr_3$	9.72	[292]
$CsSnBr_3$	10.96	[293]
$CsSnCl_3$	9.66	[293]
$FAPbI_3$	25.5	[294]
$FASnI_3$	14.6	[295]

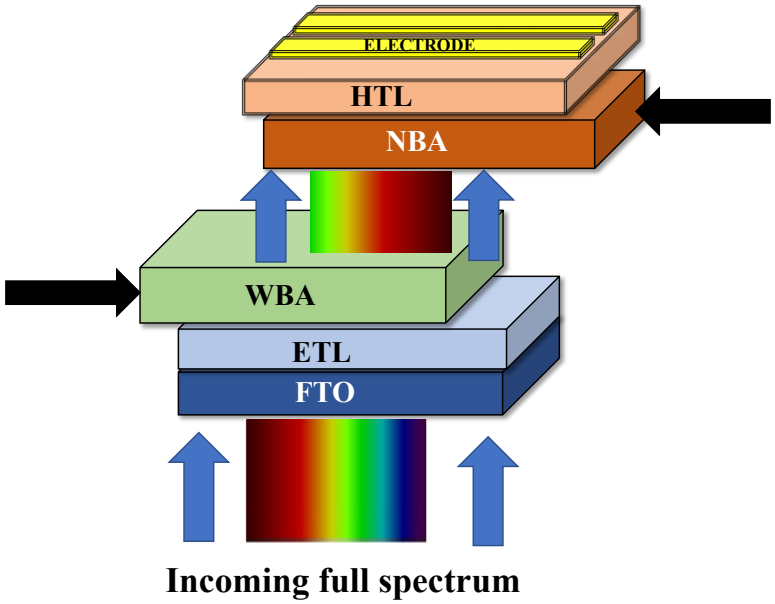

Figure 6.1 Schematics of double absorber layer perovskite solar cell illustrating the structural layout of a perovskite solar cell with two absorber layers.

The perovskite absorbers $MASnI_3$ (1.3 eV), $CsSnI_3$ (1.3 eV), $FASnI_3$ (1.5 eV), $FAPbI_3$ (1.41 eV) forms narrow bandgap (NBG) counterparts with $MAPbI_3$. These are termed as narrow bandgap absorbers (NBGA) in further discussion. The schematics of band profile for the all the absorber layer perovskite is depicted in Fig. 6.2.

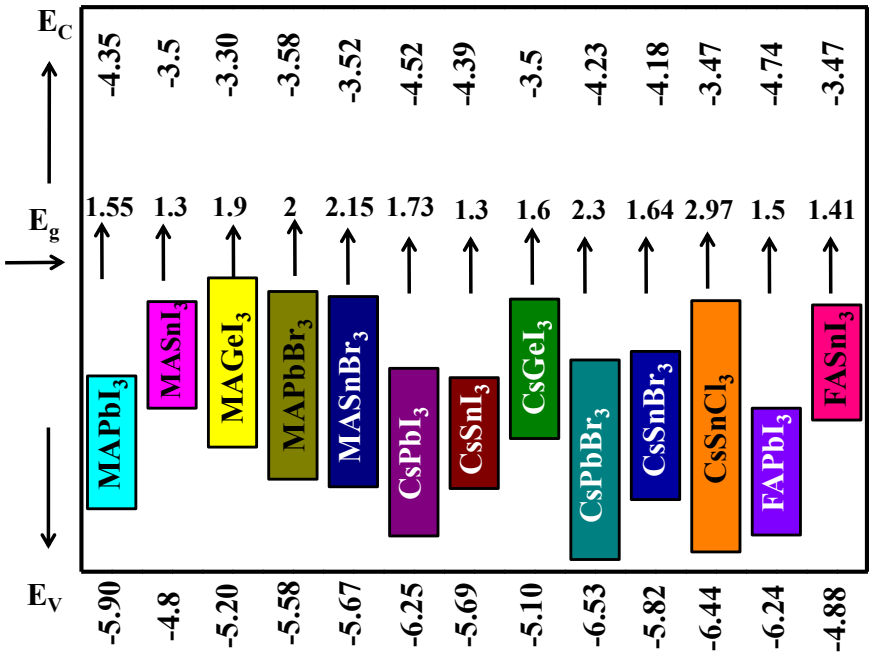

Figure 6.2 Schematics energy level diagrams of all 13 perovskite absorbers used for the study.

Table 6.2 Physical parameters of different perovskite absorbers used for the single simulation study for generating single reference set.

Parameters/ Materials	E_g (eV)	χ (eV)	ε_r	CB DOS (cm^{-3})	VB DOS (cm^{-3})	μ_n (cm^2/ Vs)	μ_p (cm^2/ Vs)	ND (cm^{-3})	NA (cm^{-3})	Ref
$MAPbI_3$	1.55	3.9	6.5	10^{18}	10^{18}	50	50	-	10^{13}	[284]
$MASnI_3$	1.3	4.1	8.2	$2*10^{18}$	$2*10^{18}$	1.6	1.6	$1*10^{19}$	-	[285]
$MAGeI_3$	1.9	3.5	10	$1*10^{16}$	$1*10^{15}$	16.2	10.1	$1*10^{9}$	$1*10^{9}$	[286]
$MAPbBr_3$	2	3.36	6.5	$2.2*10^{19}$	$2.2*10^{18}$	1.9	1.9	10^{15}	10^{17}	[287]
$MASnBr_3$	2.15	3.39	8.2	10^{18}	10^{18}	1.6	1.6	-	10^{18}	[193, 288]
$CsPbI_3$	1.73	3.95	6	$1.1*10^{20}$	$8.2*10^{20}$	25	25	-	$1*10^{15}$	[289]
$CsSnI_3$	1.3	3.6	9.93	10^{18}	10^{19}	1500	585	10^{16}	10^{15}	[290]
$CsSnGeI_3$	1.6	3.52	18	10^{18}	10^{19}	20	20	-	$2*10^{16}$	[296]
$CsPbBr_3$	2.3	3.4	4.17	10^{18}	10^{18}	378	290	-	10^{16}	[292, 297-299]
$CsSnBr_3$	1.64	4.07	5.35	10^{18}	10^{18}	511	356	-	10^{16}	[293, 298, 299]
$CsSnCl_3$	2.97	3.47	4.80	10^{18}	10^{18}	212	147	-	10^{16}	[293, 298, 299]
$FAPbI_3$	1.5	4.0	6.6	$1.2*10^{19}$	$2.5*10^{21}$	2.7	1.8	$1.3*10^{16}$	$1.3*10^{16}$	[300] [294]
$FASnI_3$	1.41	3.52	8.2	10^{18}	10^{18}	22	22	-	$7*10^{16}$	[295, 301]

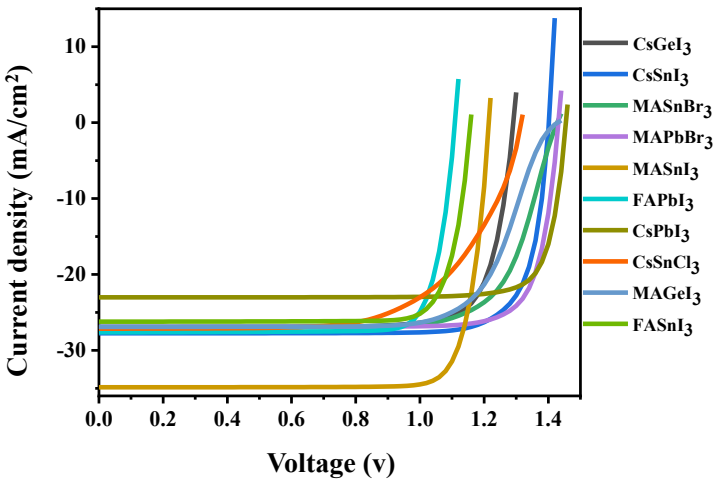

Figure 6.3 Simulated JV characteristics of all 13 combinations of double perovskite absorbers depicting the current density-voltage (JV) curves for all 13 possible combinations of double perovskite absorber layers, highlighting the variations in electrical performance parameters.

The double absorber structure is simulated by choosing $MAPbI_3$ as absorber I layer and varying the absorber II layer. The physical parameters of all the 13 absorber layers for single simulation are tabulated in Table. 6.2. The perovskite absorbers $MAPbBr_3$, $MASnBr_3$, $CsPbBr_3$, $MAGeI_3$, $CsPbI_3$, $CsSnBr_3$, $CsSnCl_3$ and $CsGeI_3$ act as WBGA while acting as a combination layer with $MAPbI_3$ which itself acts as an NBGA. Whereas the perovskite absorbers $CsSnI_3$, $MASnI_3$, $FAPbI_3$ and $FASnI_3$ acts as NBA and $MAPbI_3$ acts as WBA.

Fig. 6.3 depicts the JV curves of all the double absorber combinations. The performance parameters are tabulated in the Table. 6.3. The combination of the absorbers, $CsPbBr_3$ and $CsSnBr_3$ resulted in poor efficiency and cannot be considered to form a double absorber layer structure with $MAPbI_3$ and hence does not have a JV curve as depicted in Fig 6.3. The combination of the absorbers $CsSnCl_3$, $FAPbI_3$ and $FASnI_3$ have resulted in nominal efficiency which can be achieved through single $MAPbI_3$ absorber layer with little effort.

Table 6.3 Perovskite solar cells performance parameters with varied second absorber.

A-II	V_{OC} (V)	J_{SC} (mA/cm^2)	FF (%)	PCE (%)
$CsGeI_3$	1.29	26.96	80.72	28.1
$CsPbBr_3$	1.51	0.74	67.65	0.7
$CsPbI_3$	1.45	23.01	84.23	28.2
$CsSnBr_3$	1.05	0.25	51.36	0.14
$CsSnCl_3$	1.31	27.13	64.54	23
$CsSnI_3$	1.40	27.74	81.14	31.5
$MAGeI_3$	1.42	26.9	71.48	27.4
$MAPbBr_3$	1.43	26.89	82.70	31.8
$MASnBr_3$	1.427	26.89	74.64	28.6
$MASnI_3$	1.21	34.86	83.9	35.5
$FAPbI_3$	1.1	27.62	83.3	25.5
$FASnI_3$	1.15	26.21	82.9	25.1

$CsGeI_3$ stacked on $MAPbI_3$ simulation resulted in the improved efficiency of 28.11%. $CsPbI_3$, $MAGeI_3$ and $MASnBr_3$ almost result in the same efficiency as that of $CsGeI_3$ i.e., 28.2%, 27.46% and 28.64% respectively. The combination of $MAPbI_3$ and $MAPbBr_3$ simulation resulted in the improved efficiency of 31.84%. $CsSnI_3$ almost have same efficiency range as

that of $MAPbBr_3$. The type-II band alignment between $MAPbI_3$ and $MASnI_3$ resulted in the improved efficiency of 35.54% which is the best efficiency compared with all the remaining 11 absorbers and the single absorber PSCs of Table. 6.1.

6.2.1 Band Alignment in double absorber perovskite solar cell

There are various factors that influence the performance of the double absorber viz., band alignment, extent of absorption, generation and recombination of charge carriers. All these parameters will be discussed below for one efficient and one in efficient combination to understand the underlying device physics of the proposed structure. Fig.6.4 depicts the general schematics of the proposed structure that depicts the charge carrier transfer mechanism.

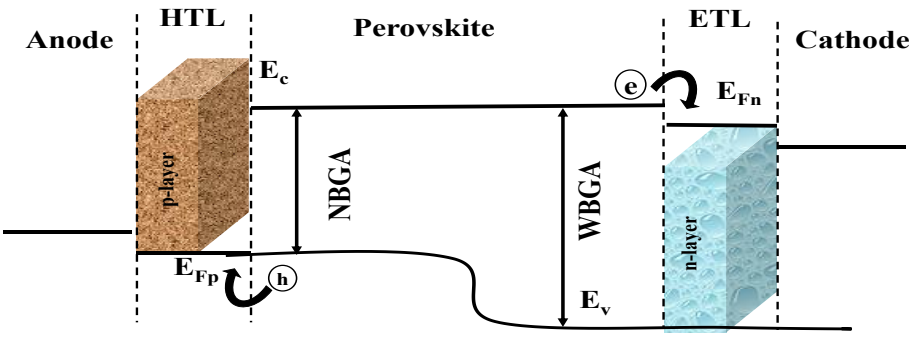

Figure 6. 4 Schematic of band alignment in double absorber layer perovskite solar cell showing the relative positions of the conduction and valence bands for each layer, as well as the electron and hole transport layers, to illustrate how efficient charge separation and transport are achieved within the device.

The built-in potential [302] for a double absorber layer structure can be calculated by deducing from the fundamental physics using the Eq. (6.1).

$$\Delta V_{bi} = \left(E_{V,WBA} - E_{C,NBGA}\right) - \left(E_{f,ETL} - E_{f,WBGA}\right) - \Delta E_{WBGA/ETL} - \left(E_{f,HTL} - E_{f,NBGA}\right) - \Delta E_{NBGA/HTL} - E_{g,NBGA} \quad (6.1)$$

Where, ΔV_{bi}- built-in potential, $E_{V,WBGA}$ - valence band energy of the WBGA, $E_{C,NBGA}$ - conduction band energy of the NBGA, $E_{g,NBGA}$- band gap energy of the NBGA, $E_{f,ETL}$ - fermi level of the ETL, $E_{f,NBGA}$ - Fermi level of the NBGA, $\Delta E_{WBGA/ETL}$ - energy level offset between the ETL and the WBGA, $E_{f,HTL}$ - fermi level of the HTL, $E_{f,WBGA}$- fermi level of the WBGA, $\Delta E_{NBGA/HTL}$ - energy level offset between the NBGA and the HTL.

Fig. 6.5 depicts the simulated band profile of the double absorber layer with NBA and WBA acting as perovskite absorber layers. The combination of these NBGA and WBGA layers forms a heterojunction. The energy levels of the narrow-bandgap material shift towards the

conduction band minima (CBM) of the wide-bandgap material. This is because the CBM of the wide-bandgap material has higher energy than the CBM of the narrow-bandgap material, and as a result, electrons from NBGA material will transfer to the WBGA material to equalize the Fermi levels resulting a staggered band type-II alignment.

From Fig. 6.5 it is evident that the conduction band of $MASnI_3$ is situated at a higher energy level than that of $MAPbI_3$. This means that electrons have a higher energy in $MASnI_3$'s conduction band. Consequently, if these materials are brought into contact, as depicted in Fig. 6.4 electrons from the conduction band of $MASnI_3$ could potentially move to the conduction band of $MAPbI_3$ due to the energy difference. This transfer of electrons would facilitate electron flow from $MASnI_3$ to $MAPbI_3$. Thereby electrons from $MAPbI_3$ will be collected by the ETL supporting the efficient transfer of electrons. The valence band of $MAPbI_3$ is situated at a higher energy level than that of $MASnI_3$. This suggests that holes in the valence band of $MASnI_3$ could move to the valence band of $MAPbI_3$. This hole transfer would facilitate hole flow from $MAPbI_3$ to $MASnI_3$. Thereby holes from $MASnI_3$ will be collected by the HTL supporting the efficient transfer of holes.

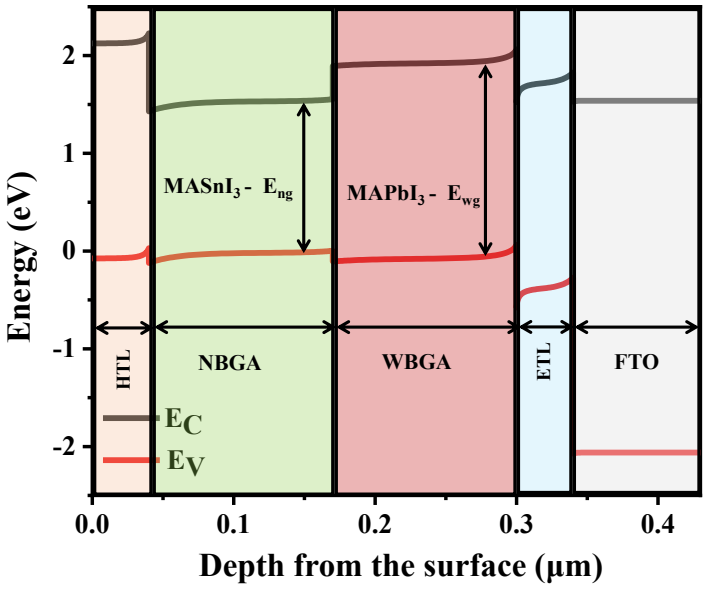

Figure 6.5 Simulated band profile of $MASnI_3$ (NBA)- $MAPbI_3$ (WBA) double absorber/absorber layer perovskite solar cell.

Similarly, from Fig. 6.6 it is evident that the conduction band of $MAPbI_3$ is situated at a higher energy level than that of $CsSnBr_3$. Consequently, if these materials are brought into contact, electrons from the conduction band of $MAPbI_3$ likely tend to move to the conduction band of $CsSnBr_3$ due to the energy difference. But from Fig. 6.6 $CsSnBr_3$ is associated with HTL and

transfer of holes to $CsSnBr_3$ increases the efficiency of the device based on working principle of the perovskite solar cell. Instead, the device architecture is such that the $MAPbI_3$ transfers electrons to $CsSnBr_3$ decreasing the overall performance of the device.

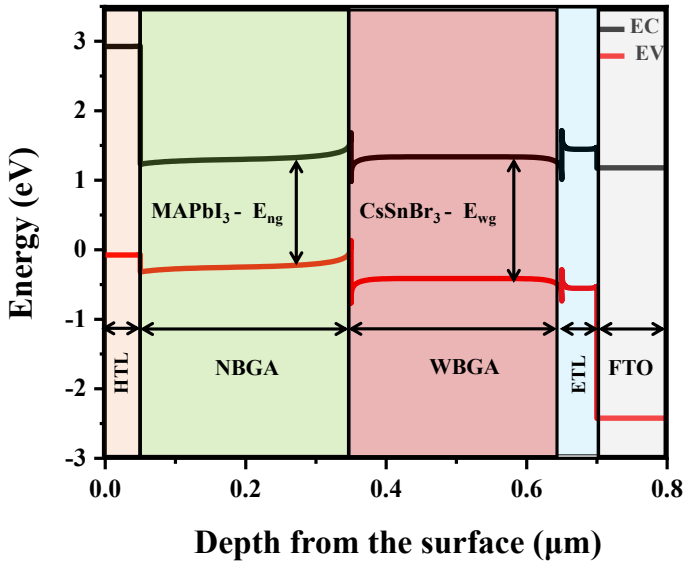

Figure 6.6 Simulated band profile of $MAPbI_3$ (NBA)-$CsSnBr_3$ (WBA) double absorber/absorber layer perovskite solar cell.

6.2.2 Generation and Recombination profiles in double absorber perovskite solar cell

The generation profile refers to the spatial distribution of charge carriers generated within the perovskite absorber layer upon exposure to incident light. It indicates where and how quickly electrons and holes are created in response to photons. In a perovskite solar cell, the absorption of photons generates electron-hole pairs. The generation profile is affected by factors such as the absorption coefficient of the perovskite material, the incident light intensity, and the photon energy spectrum. Understanding the generation profile helps in optimizing the thickness and composition of the absorber layer, ensuring that a high percentage of incident photons lead to effective charge carrier generation.

The recombination profile illustrates the spatial distribution and rate at which electrons and holes recombine within the perovskite layer. Recombination is a crucial process that can limit the efficiency of a solar cell. Perovskite solar cells are susceptible to various recombination mechanisms, including radiative (recombination with photon emission) and non-radiative (recombination without photon emission) processes. These mechanisms occur at interfaces, defects, and grain boundaries within the perovskite layer. Understanding the recombination profile is essential for minimizing losses due to carrier recombination. Strategies to passivate

defects, improve material quality, and enhance interface engineering are employed to mitigate recombination effects. By tailoring the material properties and device architecture, researchers aim to reduce recombination rates and prolong the lifetime of charge carriers, leading to higher solar cell efficiency. The generation and recombination profiles in perovskite solar cells provide crucial insights into how charge carriers are created and lost within the device. Optimizing these profiles is fundamental for achieving high-efficiency solar cells, and it involves strategies such as material engineering, interface passivation, and defect mitigation.

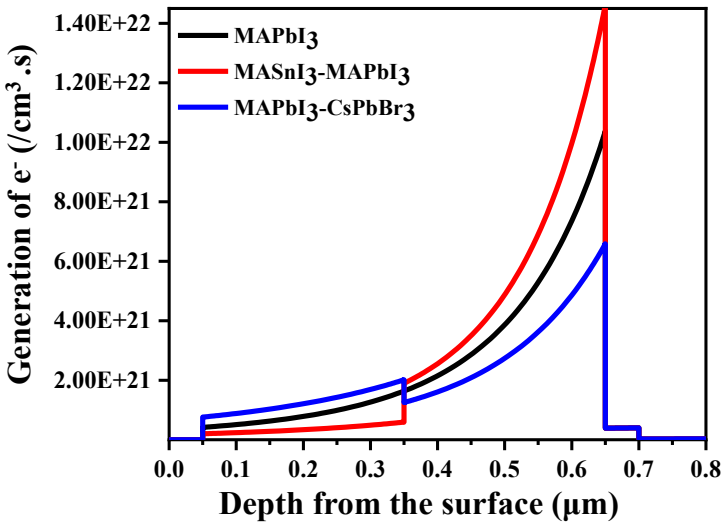

Figure 6.7 Generation profile of electrons in single absorber ($MAPbI_3$) and double absorber ($MASnI_3$-$MAPBI_3$& $MAPbI_3$-$CsSnBr_3$) layered perovskite solar cell.

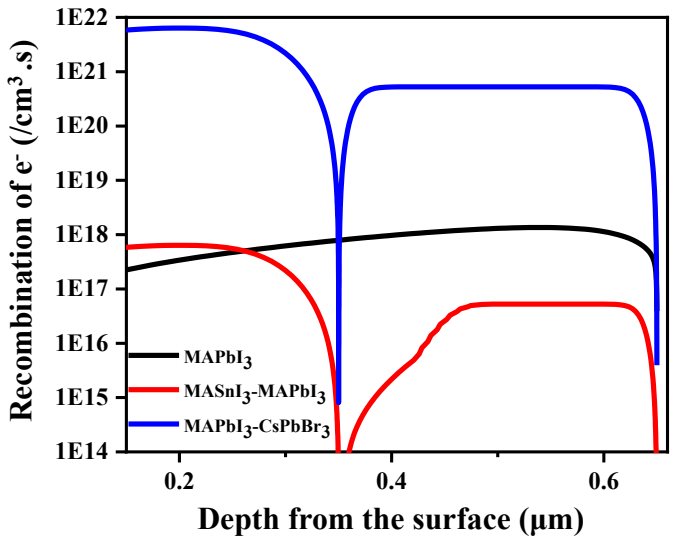

Figure 6.8 Recombination profile of electrons in single absorber ($MAPbI_3$) and double absorber ($MASnI_3$-$MAPBI_3$& $MAPbI_3$-$CsSnBr_3$) layered perovskite solar cell.

The generation and recombination of the electrons in the absorber layer and at interfaces is also a crucial parameter to estimate the device performance. Fig. 6.7 depicts the generation of profile of electrons in the absorber layer of PSCs. $MASnI_3$-$MAPbBr_3$ double absorber PSC shows greater generation profile compared with single absorber $MAPbI_3$ PSC. Whereas $MAPbI_3$-$CsSnBr_3$ double absorber PSC shows low generation profile compared with single absorber $MAPbI_3$ PSC. The same trend is followed for the recombination profile as depicted in Fig. 6.8. Both the generation and recombination profiles support the favorable condition of forming $MASnI_3$-$MAPbI_3$ double absorber layered PSC.

6.2.3 Quantum efficiency profile in double absorber perovskite solar cell

Optimizing the absorption of photons and understanding the quantum efficiency (QE) profile is a crucial aspect in the design of a double absorber perovskite solar cell, which typically consists of two different perovskite layers with varying bandgaps. Tailoring the absorption process, especially in the case of double absorber cells, where different layers are tailored to capture distinct portions of the solar spectrum, is crucial. The Quantum Efficiency (QE) profile serves as a valuable tool in assessing how efficiently incident photons are converted into charge carriers within each specific wavelength range. This information aids in the precise identification of absorption overlaps between the two absorber layers, ensuring that each layer captures photons with maximum efficiency, avoiding redundancy or loss.

Achieving a balanced absorption profile across the various layers is fundamental in double absorber cells. The QE profile plays a pivotal role in this process, assisting in the customization of each layer to absorb photons at specific wavelengths. This equilibrium ensures that the entire solar spectrum is effectively harnessed, ultimately leading to a higher overall efficiency. Efficient charge extraction and minimizing carrier recombination are paramount for attaining high efficiency in perovskite solar cells. The QE profile, by providing insights into absorption characteristics, enables researchers to design interfaces and charge transport layers that facilitate the effective extraction of carriers, particularly in regions of high absorption. Furthermore, the QE profile informs the selection of bandgap combinations for the two absorber layers. Through a meticulous analysis of the absorption properties of each layer, researchers can opt for bandgaps that complement one another, thereby maximizing the overall device efficiency.

Understanding potential areas of energy loss within the device is critical. The QE profile serves as a valuable guide in identifying such areas, allowing for the development of strategies to

mitigate losses stemming from non-radiative recombination and other factors. Moreover, knowledge of the QE profile directly influences material selection and device engineering endeavors. Researchers can leverage this information to fine-tune material properties, thicknesses, and interfaces, ultimately enhancing the performance of double absorber perovskite solar cells. This targeted approach holds the key to advancing the efficiency and viability of this promising solar technology. Determining the quantum efficiency profile in a double absorber perovskite solar cell is essential for tailoring the device to efficiently capture and convert photons, thereby improving its overall efficiency. This understanding guides material choices, layer thicknesses, and device architecture, ultimately leading to more efficient solar energy conversion.

Each material $MAPbI_3$, $MASnI_3$ and $CsSnBr_3$, has its own optimal range of wavelengths of light that it can absorb efficiently as depicted in Fig. 6.9. $MAPbI_3$, $MASnI_3$, $CsSnBr_3$ have higher absorption efficiencies for wavelengths lesser than 600nm. $MASnI_3$-$MAPbI_3$ combination depicts an efficiency of over 90% for the wavelengths till 800nm showing excellent absorption characteristics. Whereas the $MAPbI_3$-$CsSnBrI_3$ combination depicts an efficiency of 20% showing deprived absorption characteristics owing to the low generation profile of electrons as depicted in Fig. 6.7.

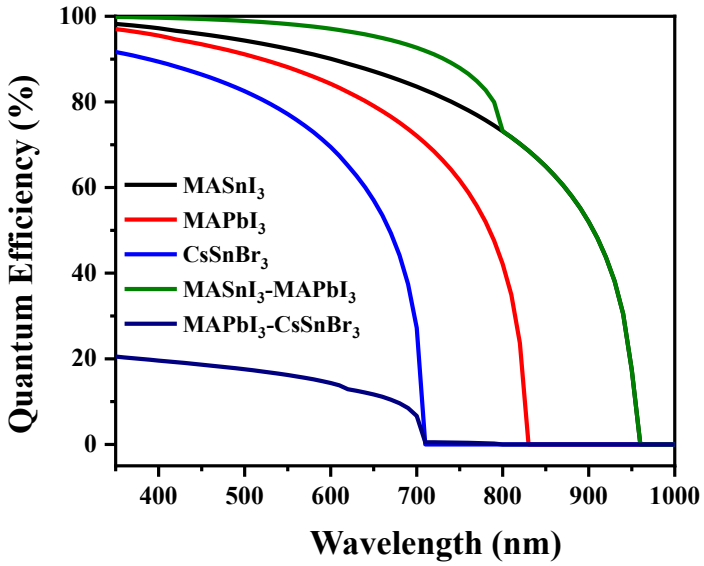

Figure 6. 9 Quantum efficiency of the single absorber ($MAPbI_3$, $MASnI_3$, $CsSnBr_3$) and double absorber ($MASnI_3$-$MAPbBr_3$& $MAPbI_3$-$CsSnBr_3$) perovskite solar cell.

The favorable condition of band alignment as depicted in Fig. 6.5 supports the increased efficiency along with the and lattice alignment. The double absorber layer configuration of $MAPbI_3$ and $MASnI_3$ involves having closely matched lattice constants between the two

materials. When the lattice constants of both $MAPbI_3$ and $MASnI_3$ are relatively close, the crystal lattices of the two materials can stack together with minimal strain or distortion at the interface.

This lattice alignment is beneficial because it reduces the likelihood of lattice mismatch-induced defects, strain, and disruptions at the interface between the two layers. When the crystal lattices match well, the atoms can fit together more smoothly, resulting in a coherent and continuous interface. This coherent interface facilitates efficient charge transfer and minimizes recombination losses, enhancing the overall performance of the double-layer structure.

$CsSnBr_3$ stacked below $MAPbI_3$ simulation resulted in the declined efficiency of 0.14%. The main reason in the declined efficiency is due to probable mismatch in their lattice and is the probable reason for the higher recombination profile as depicted in Fig. 6.8. Crystal structures and their lattices play a vital role in depicting the efficiency of the double absorber layered PSC. $MAPbI_3$ crystal structure consists of corner-sharing octahedra of PbI_6 formed by lead and iodine atoms, with the organic methylammonium cations occupying the spaces between these octahedra. $CsSnBr_3$ also belongs to the family of perovskite materials. Similar to $MAPbI_3$, $CsSnBr_3$'s crystal structure is characterized by corner-sharing octahedra, where tin and bromine atoms form octahedral structures, and cesium cations occupy the spaces between these octahedra.

In the case of $MAPbI_3$ and $CsSnBr_3$, even though both materials have octahedral structures, the sizes of the ions involved are not exactly the same. The difference in ionic radii between lead and tin cations, as well as between iodine and bromine anions, contributes to lattice mismatch. When layers of these materials are stacked, the lattice mismatch can lead to strain at the interface, which distorts the regular crystal lattice. This strain can create localized defects, dislocations, and even changes in the electronic properties of the materials. These lattice mismatch-induced defects can act as recombination centers for charge carriers, reducing the efficiency of the device.

Careful engineering of interfaces, choosing appropriate buffer layers, and optimizing deposition techniques are essential strategies to mitigate these lattice mismatch-related issues and enhance the compatibility between these materials for efficient optoelectronic devices.

6.2.4 WBGA and NBGA Defect Profile

The exploration of WBGA and NBGA defect profiles is a critical facet. Understanding the defect landscape within wide bandgap materials is pivotal for optimizing their performance, as defects play a dual role: influencing electronic properties and offering avenues for deliberate engineering to tailor material characteristics.

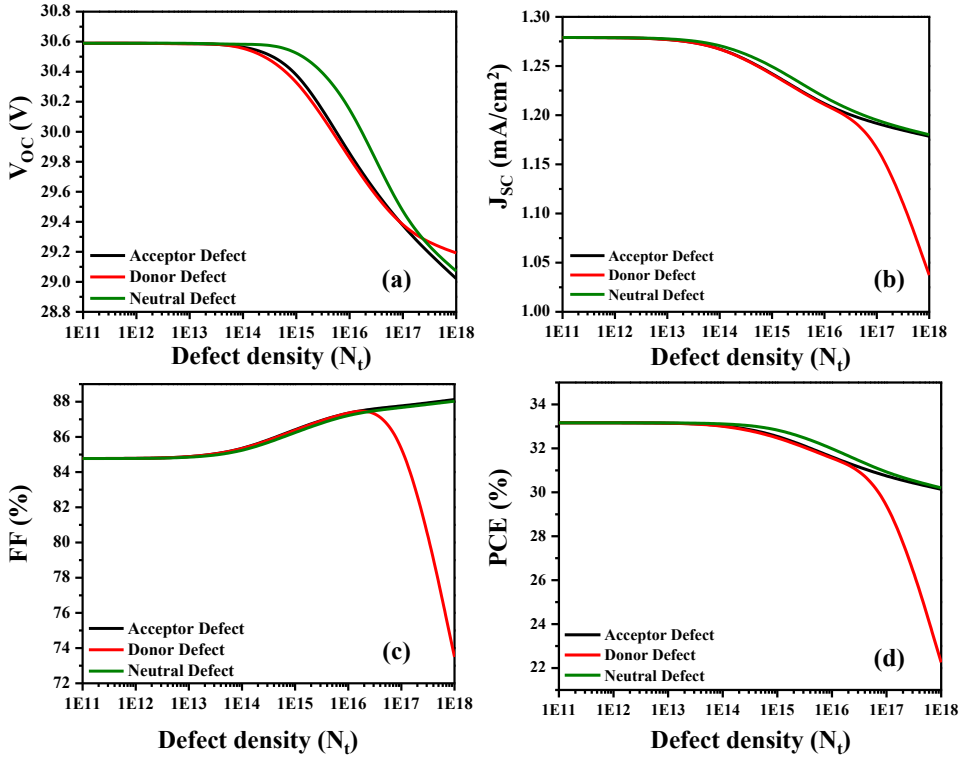

Figure 6.10 Wide band gap absorber defect density Profiling depicting the impact of defect density in a narrow band gap absorber on four key performance parameters of a perovskite solar cell: (a) open circuit voltage, (b) short circuit current density, (c) fill factor and (d) power conversion efficiency.

The effects of different defects on WBGA are simulated by varying the acceptor, donor and neutral defect density from 10^{11} to 10^{18} cm^{-3}. In the investigation of defects within Wide Band Gap Absorber (WBGA) perovskite solar cells, a systematic analysis reveals distinctive trends across critical performance parameters. Notably, the presence of Neutral defects exhibits consistent behavior across various defect concentrations, with the efficiency remaining stable. This constancy can be ascribed to the limited impact of Neutral defects on charge carrier dynamics, ensuring reliable efficiency outcomes. Similarly, the Open-Circuit Voltage (Voc) as depicted in Fig. 6.10 (a) remains relatively constant, indicating that Neutral defects introduce minimal energy barriers for charge carriers, exerting a negligible effect on Voc. While the Short-Circuit Current (Jsc) as depicted in Fig. 6.10 (b) remains stable at lower defect

concentrations, a subtle decrease is observed at higher concentrations, suggesting that Neutral defects may modestly influence charge generation, particularly with increasing defect density. Remarkably, the Fill Factor (FF) as depicted in Fig. 6.10 (c) maintains stability, emphasizing that Neutral defects do not significantly impede charge transport and extraction efficiency, contributing to the constancy of the fill factor. As depicted in Fig. 6.10 (d) the efficiency remains stable.

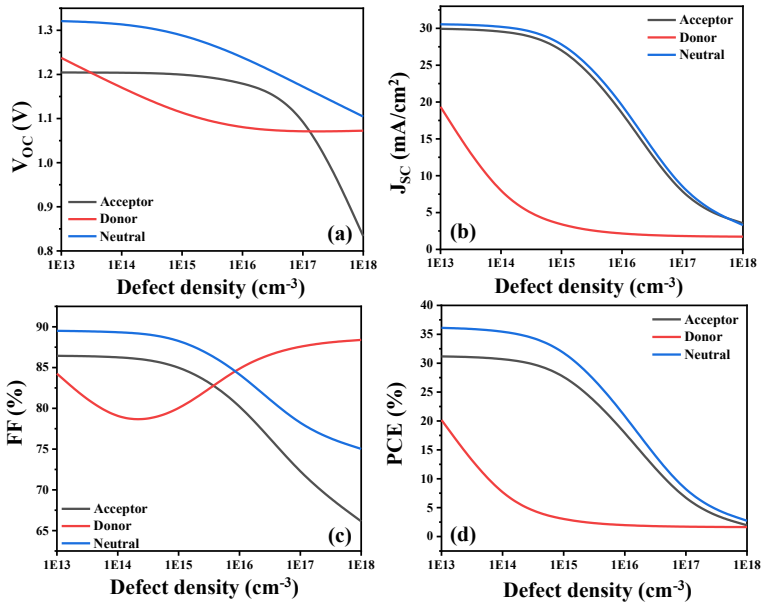

Figure 6.11 Narrow band gap absorber defect density Profiling depicting the impact of defect density in a narrow band gap absorber on four key performance parameters of a perovskite solar cell: (a) open circuit voltage, (b) short circuit current density, (c) fill factor and (d) power conversion efficiency

Turning attention to Donor defects in perovskite solar cells, a parallel theme of stability emerges across key performance parameters. Efficiency remains consistent across diverse defect concentrations as shown in Fig. 6.10 (d), underscoring the limited influence of donor defects on charge carrier dynamics and ensuring stable efficiency outcomes. Voc remains stable, as shown in Fig. 6.10 (a), signifying that donor defects introduce negligible energy barriers for charge carriers, exerting minimal impact on Voc. Moreover, Jsc as shown in Fig. 2(b), displays relative steadiness, highlighting that donor defects do not substantially affect charge generation, contributing to the stability of the short-circuit current. The Fill Factor also remains relatively stable, indicating that donor defects do not exert a significant impact on charge transport and extraction efficiency, contributing to the constancy of the fill factor as shown in Fig. 6.10 (c). Both Neutral and Donor defects demonstrate a trend of stability in performance parameters, indicating consistent efficiency across diverse defect concentrations.

This stability underscores the potential for nuanced modifications in defect characteristics to mitigate adverse impacts on efficiency, presenting avenues for targeted improvements.

In the context of Voc, slight enhancements are observed at higher defect concentrations. This suggests that Acceptor defects, potentially reducing the energy barrier for charge carriers, contribute to improvements in open-circuit voltage, exerting a positive influence on this key performance parameter. Similarly, Short-Circuit Current (Jsc) exhibits modest improvements at higher defect concentrations as shown in Fig. 6.10 (b). The presence of Acceptor defects may play a role in enhancing charge generation or mitigating specific recombination mechanisms, resulting in an overall improvement in short-circuit current. The Fill Factor also sees slight improvements at higher defect concentrations as shown in Fig. 6.10 (c) indicating that characteristics associated with Acceptor defects may contribute to enhanced charge transport and extraction efficiency. These improvements collectively lead to an augmented fill factor, showcasing the potential positive impact of tailored defect characteristics on overall device performance.

Fig. 6.11 depicts the influence of NBGA different defects on the device. The presence of acceptor defect shows a steep slope in the value of VOC with the increased defect density and falls to the lowest values of 0.7 V as shown in Fig. 6.11 (a). The acceptor and the neutral defects follow the same trend throughout the varied density for JSC, FF and PCE as depicted in Fig. 6.11 (b), (c) & (d) respectively.

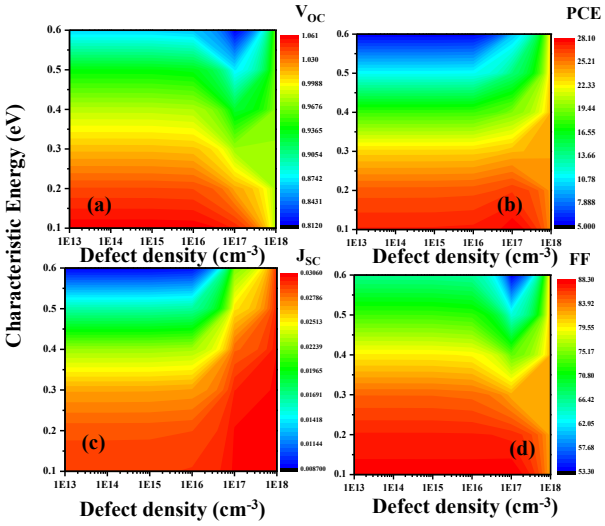

Figure 6.12 Defect Density Profiling of wide band gap absorbers: correlation with characteristic energy of defects (a) open circuit voltage, (b) power conversion efficiency, (c) short circuit current density and (d) fill factor

The characteristic energy of defects plays a key role in modulating the charge carrier dynamics, affecting processes such as charge generation, recombination, and transport within the solar

cell. Exploring how variations in the characteristic energy of defects influence the overall device parameters is essential for advancing the design and efficiency of the device. A donor defect with increased characteristic energy tends to introduce an energy level within the bandgap that is relatively closer to the conduction band. This implies that it acts as a trap for holes, making it easier for them to transition from the valence band to this donor energy level. The impact of donor defect on the performance parameter is studied with respective to the characteristic energy of the defect for both WBGA and NBGA.

An elevated characteristic energy WBGA reduces the energy barrier for charge carriers, particularly holes, especially at higher defect densities (Fig. 6.12 (a)). This phenomenon leads to a decrease in the VOC, influencing charge transport and extraction efficiency. Systematic variation in the characteristic energy of donor defects, ranging from 0.1 eV to 0.6 eV, reveals a discernible impact on PCE (Fig. 6.12 (b)). Generally, there's a decreasing trend in PCE with increasing characteristic energy for each defect density. Similarly, a decreasing trend in JSC values is observed with higher characteristic energies (Fig. 6.12 (c)), indicating a diminishing impact on charge generation efficiency. Higher defect densities correlate with lower JSC values, signifying compromised short-circuit current under heightened defect concentrations.

6.3 Machine Learning Approach

Machine learning (ML) plays a substantial role in predicting the PCE of PSCs by analyzing and identifying the relationships among various factors affecting their performance [303]. ML optimize the manufacturing process of perovskite solar cells by predicting the optimal conditions for producing high-efficiency cells. By analyzing data from various stages of the manufacturing process, machine learning algorithms can identify the most significant factors affecting cell efficiency and provide recommendations for process improvements [279, 304]. The rapid growth of perovskite solar cell research has been accompanied by the integration of machine learning algorithms, offering new avenues for addressing critical challenges and optimizing device performance. We have wide variety of ML algorithms. We categorize and analyze a range of ML algorithms that have found applications in perovskite solar cell research [305-308]. These include Random Forests, Support Vector Machines, Neural Networks, Genetic Algorithms etc.

6.3.1 Data Sets

The focus of this paper is to investigate the performance of double absorber layer PSC. We have considered ten different absorbers for perovskite solar cells (PSC), each with ten input features. There is no wide range up-to-date research to determine the improved efficiency of

PSCs by combining two different perovskite absorbers. Therefore, to address the lack of an experimental dataset, we utilized SCAPS simulations to create the necessary data.

The dataset composed with 3490 performance data points of PSC. We extracted the input features of perovskite absorbers from 250 articles published between 2016 to 2022 through literature survey. The data set was considered from the literature, which presented the device's physical parameters for simulating through SCAPS. ETL, HTL and electrodes for creating the device were maintained consistent. The first and second perovskite absorber layers stacked on each other depending on the band gap were varied by varying the input features. The performance metrics viz., V_{OC}, J_{SC}, FF and PCE which are crucial in validating the PSC devices, are chosen as the target attributes. We have considered 10 physical parameters of the absorber that influence the performance metrics are as follows:

Bandgap (E_G): In solid-state physics, a band gap is a range of energy levels in a crystal that an electron cannot possibly occupy. A material's band structure, or the continuum of permitted and prohibited electron energy levels, will typically contain several band gaps. The bandgap of the materials determines the energy levels at which the electrons can be excited to produce a photocurrent. Metal may also produce current on shining light but that is not due to bandgap. The bandgap of the perovskite layer is particularly important as it must match the energy of the incoming photons for efficient light absorption [309, 310].

Electron affinity (χ): The electron affinity of the materials determines how readily the materials donate or accept electrons. This is important for determining the flow of charge carriers within the device [311, 312].

Doping concentration (N_A, N_D): The doping concentration of the different layers can significantly affect the electrical performance of the device. For example, the concentration of charge carriers in the absorber layer affects the carrier transport and recombination within the device [313].

Layer thicknesses (T): The thicknesses of the different layers in the solar cell can affect light absorption and the recombination of charge carriers. The thicker absorber layer absorbs more light and might also have more recombination sites [89, 314].

Mobility of electrons (μ_n): The mobility of electrons refers to the ease with which electrons can move through a material when subjected to an electric field. Electrons' mobility influences the solar cell's efficiency because it affects the rate at which electrons move through the device.

Thus, it affects the overall current output of the device. A high electron mobility results in a higher photocurrent output and thus increases the device's overall efficiency [315].

Mobility of holes (μ_p): The mobility of holes refers to the ease with which holes can move through the material when subjected to an electric field. The mobility of holes influences the efficiency of the solar cell because it affects the rate at which holes move through the device, and thus, it affects the overall current output of the device. A high hole mobility results in a higher photocurrent output and thus increases the device's overall efficiency [315].

Conduction band DOS(N_C): The conduction band DOS determines the density of available states for electrons to occupy when excited across the band gap. Thus, it affects electron concentration and mobility [316].

Valence band DOS(N_V): The valence band DOS determines the density of available states for holes to occupy when excited across the band gap. Thus, it affects the hole concentration and mobility [316].

Dielectric permittivity (ε_r): Dielectric permittivity describes the material's ability to store electrical energy in an electric field. In a PSC, the presence of an electric field affects the movement of charge carriers. Thus, the dielectric permittivity plays a critical role in determining the charge transport properties of the material. In particular, the dielectric permittivity affects the screening of electrostatic interactions between charged particles, such as electrons and holes. A high dielectric permittivity leads to a stronger screening of electrostatic interactions, resulting in a decrease in the Coulombic interaction between charged particles, which can reduce recombination rates and increase the device's efficiency [317, 318].

Since we are implementing this for a double layer structure with a narrow and wide band gap absorber, we have a combination of 20 input features. By varying the input features of each absorber, we have formulated 3490 input samples for which simulations are carried out in SCAPS for formulating the performance parameter to map with the target attributes. Finally, we have created the dataset, which was built predominantly using SCAPS. The other input parameters were kept constant for all the datasets, i.e., the defect density (N_t) of all the perovskite absorbers is considered as 10^{15} and the thermal velocity of holes and electrons are considered as 10^7 cm/s. The simulation is carried out under the standard illumination at AM1.5.

Table 6.4 Sample compilation of absorber parameters ($MAPbI_3$ & $MASnI_3$) in perovskite solar cells.

Parameter / Material	T (μm)	E_g (eV)	χ (eV)	ε_r	CB DOS (cm^{-3})	VB DOS (cm^{-3})	μ_n (cm^2/Vs)	μ_p (cm^2/Vs)	ND (cm^{-3})	NA (cm^{-3})	Ref
$MAPbI_3$	0.45	1.5	3.93	30	$2.5*10^{20}$	$2.5*10^{20}$	50	50	-	-	[165]
$MAPbI_3$	0.4	1.5	3.93	30	$2.5*10^{20}$	$2.5*10^{20}$	50	50	-	$2.1*10^{17}$	[168]
$MAPbI_3$	0.1-2	1.55	3.9	6.5	-	-	50	50	0	10^{14}	[319]
$MAPbI_3$	0.85	1.55	3.9	30	$2*10^{18}$	$2*10^{19}$	10	10	-	10^{17}	[320]
$MAPbI_3$	0.1-1	1.5	3.9	30	$2.5*10^{20}$	$2.5*10^{19}$	50	50	0	10^{18}	[165]
$MAPbI_3$	0.4	1.55	3.93	31	$2*10^{18}$	$1.8*10^{18}$	10	10	10^{12}	10^{14}	[321]
$MAPbI_3$	-	1.55	3.9	18	$2.2*10^{18}$	$1.8*10^{19}$	2	2	$5.21*10^9$	$5.2*10^9$	[322]
$MAPbI_3$	-	1.55	3.93	10	$2.75*10^{18}$	$3.9*10^{18}$	1	1	10^9	10^{19}	[323]
$MAPbI_3$	0.55	1.55	3.9	6.6	$1.2*10^{19}$	$2.9*10^{19}$	0.5	0.5	$1.3*10^{16}$	$1.3*10^{16}$	[324]
$MAPbI_3$		1.61	3.9	6.5	$2.75*10^{18}$	$3.9*10^{18}$	2	2		10^{10}	[325]
$MASnI_3$	0.45	1.3	4.2	8.2	$1*10^{18}$	$1*10^{18}$	1.6	1.6	10^{14}	-	[320]
$MASnI_3$		1.3	4.17	6.5	$1*10^{18}$	10^{19}	1.6	1.6	-	-	[326]
$MASnI_3$	0.44	1.3	4.2	10	$1*10^{18}$	10^{18}	1.6	1.6	-	$3.2*10^{15}$	[327]
$MASnI_3$	0.45	1.45	4	8.2	10^{18}	10^{18}	22	22	-	$7*10^{16}$	[328]
$MASnI_3$	-	1.35	4.17	6.5	10^{18}	10^{19}	1.6	1.6	-	-	[329]
$MASnI_3$	0.5	1.3	4.17	8.2	10^{18}	10^{19}	1.6	1.6	-	10^{16}	[193]
$MASnI_3$	0.45	1.3	4.17	8.2	10^{18}	10^{19}	2000	300	-	10^{15}	[330]
$MASnI_3$	0.6	1.3	4.17	8.2	-	-	2	2		10^{15}	[331]

Data Collection: Information from different research papers on the physical parameters of all the 13 absorber materials is gathered. These parameters include 10 different characteristics as discussed. Each literature source provides values based on their experimental or theoretical findings.

Data Compilation: The collected parameter values from different literature sources are organized into a structured dataset. Each row of the dataset represents a set of parameter values associated with a specific configuration or experimental condition of the different absorber material. A sample set of parameter values from each reference is tabulated in Table. 6.4 for reference.

Dataset Creation: Using the compiled data, different combinations of absorber parameter values based on the available literature are generated to create the input dataset. This input dataset is used to generate the V_{OC}, J_{SC}, FF and PCE for all the possible combinations. Now, these values are combined with the input dataset accordingly to create the original dataset to

feed the ML algorithm. This results in a diverse dataset containing multiple parameter combinations for different absorber materials.

6.3.2 Framework for Machine Learning Approach

The Random Forest Algorithm is a supervised ML technique widely used for solving regression and classification problems [332-334]. The algorithm is based on the idea of a forest, comprising numerous decision trees on various dataset subsets [335, 336]. The algorithm is based on the idea of a forest, comprising numerous decision trees on various dataset subsets. As the number of trees in a random forest algorithm increase, so does its accuracy and problem-solving capability. The algorithm acts as a classifier, taking the average of multiple decision trees to enhance the accuracy of prediction for the given dataset.

We used MATLAB to implement the ML algorithm. The dataset comprises of 3490 rows and 20 columns, each column representing a feature of a solar cell and four attributes making it to 24 columns. Prior to training the machine learning model, the data was preprocessed by cleaning using the following Eq. (6.2).

$$z = \frac{x_i - \frac{1}{n}\sum_{i=1}^{n} x_i}{\sqrt{\frac{1}{n}\left(\sum_{i=1}^{n}\left[x_i - \frac{1}{n}\sum_{i=1}^{n} x_i\right]^2\right)}} \tag{6.2}$$

Where n is the number of values in the set, x is a value in the set.

The data is split into 60% train data set, 20% validation data set and 20% test data set categories for training the model. The RF regression is trained by using all 20 features and 4 target attributes by varying the hyper parameters. Then we predict the performance parameters of the PSC for the test set using the `predict` function on the trained model as depicted in Fig. 6.13. Later, the RF classification algorithm is implemented to classify 4 different classes which are Good, better, nominal and not suitable as depicted in Fig. 6.13. These classes are used to identify the suitability of stacking the perovskite absorber layers on one another.

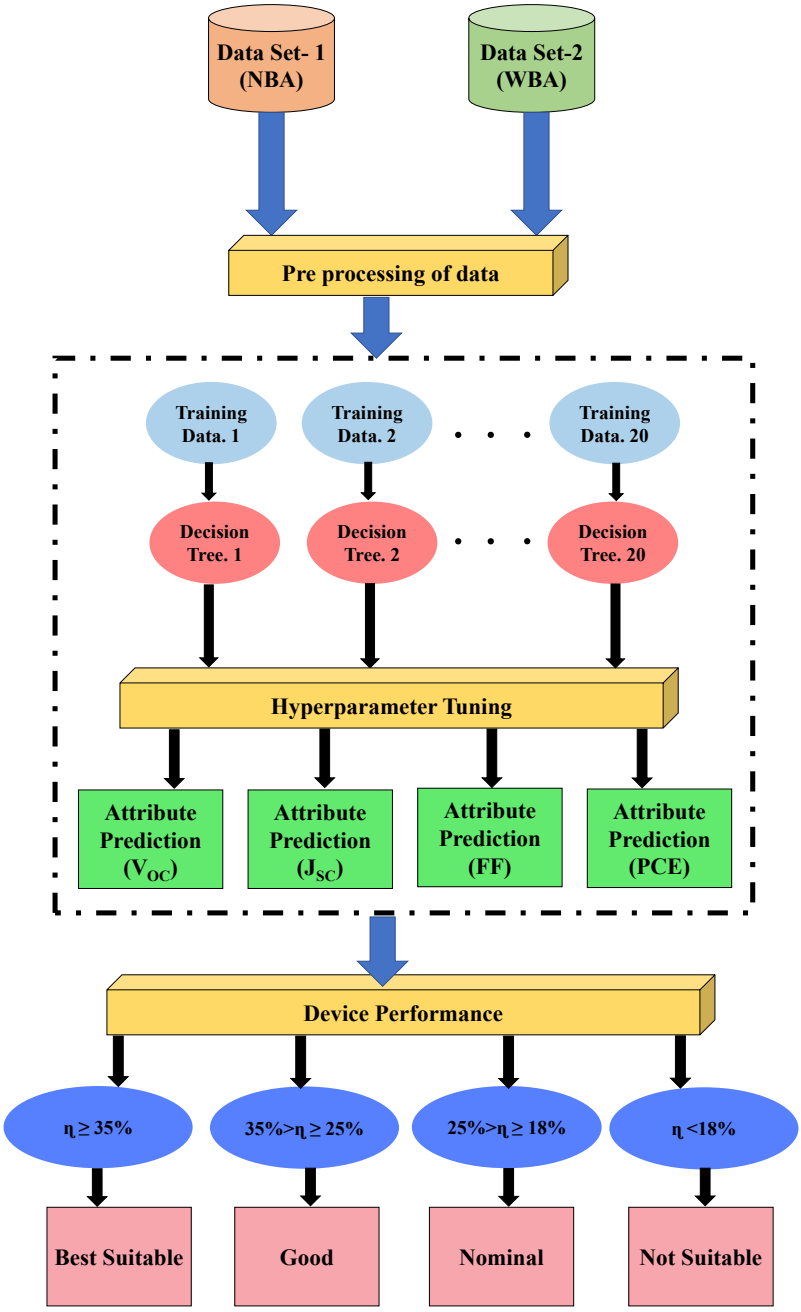

Figure 6.13 Process flow for predicting and classifying the suitable set of double absorber perovskite pair.

6.4 Regression Analysis

The RF regression model has 20 features, 10 for each absorber layer. Fig. 6.14 depicts the feature importance of all the 20 features in predicting all the four attributes J_{SC}, V_{OC}, FF and PCE. In predicting the attribute J_{SC} the highest feature importance for both the absorber layers was depicted as the thickness of the perovskite absorber layer. The thickness of the absorber is a critical parameter because it determines the amount of light that is absorbed by the material and the efficiency of the device.

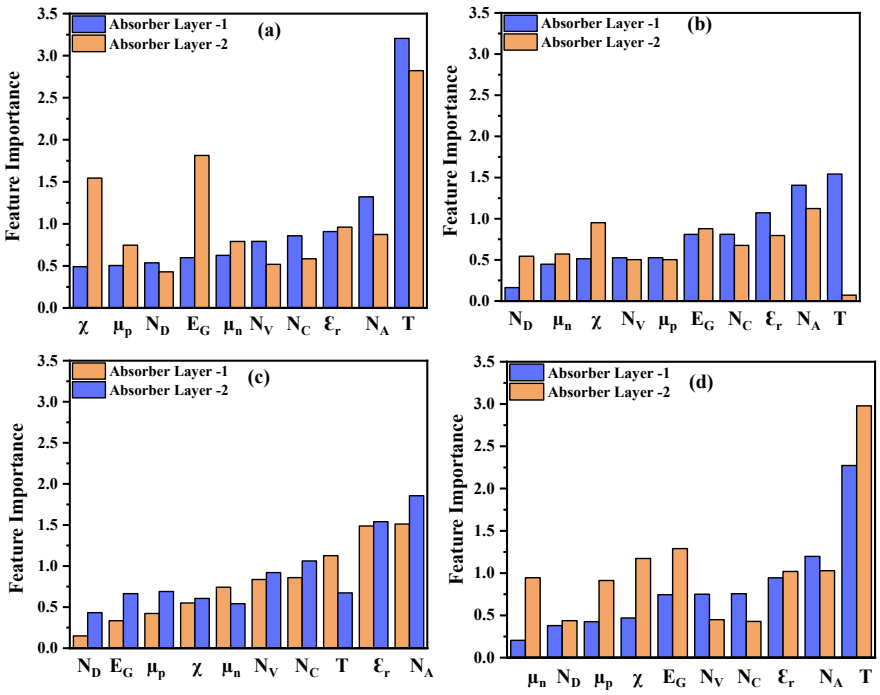

Figure 6.14 Relative importance of the physical parameters of perovskite absorber layer to predict the (a) short circuit current density (J_{SC}) (b) open circuit voltage V_{OC} (c) fill factor (FF) and (d) power conversion efficiency (PCE)

*(Absorber layer-2 depicts the physical parameters of narrow bandgap absorber (NBGA) Absorber layer-1 depicts the physical parameters of wide bandgap absorber (WBGA) layer)

The thickness of the absorber layer plays a vital role in influencing the J_{SC} of a PSC as depicted in Fig. 6.14 (a) because it affects the absorption and charge carrier generation efficiency of the material. When stacking two different perovskite absorber layers on top of one another, the thickness of each layer should be adjusted to achieve the desired J_{SC}. Therefore, improving the thickness of the absorber layers is critical to achieve the maximum J_{SC} in a perovskite solar cell with stacked absorber layers and hence has a greater importance in predicting the attribute J_{SC}.

The bandgap of the perovskite absorber layer is crucial in determining the V_{OC} of a PSC as depicted in Fig. 6.14 (b) because it dictates the amount of energy required for the formation of electron hole pairs in the material. Therefore, choosing the appropriate bandgap of each perovskite absorber is crucial to optimize the performance of a double absorber layer PSC. Hence both the layers have equal importance for the feature E_G. The attributes FF and PCE are correlated with the attributes J_{SC} and V_{OC} as depicted in Fig. 6.14 (c, d) respectively. Their feature importance in predicting their values is a combination of the feature importance of J_{SC} and V_{OC} accordingly as depicted in Fig. 6.11.

The plot depicted in Fig.6.15 shows how the out of bag regression (OOB) error changes with the increase in decision trees of the RF model. Typically, as the number of trees increases, the OOB error decreases for all the 4 attributes. However, the rate of decrease in OOB error slows down as the number of trees increases. The significant enhancement in the performance of the RF regression model is almost attained for the count of 20 decision trees.

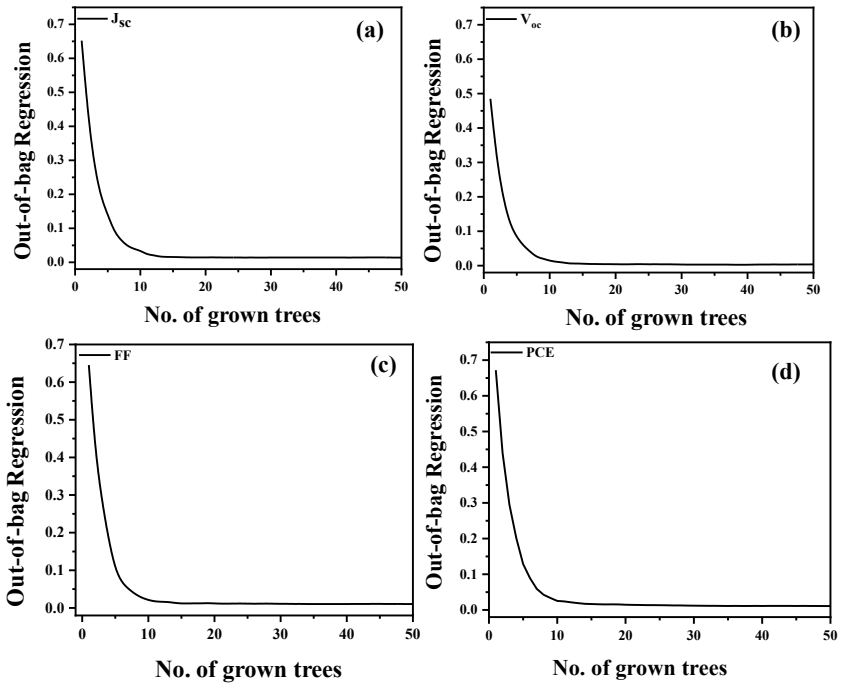

Figure 6.15 Out-of-bag regression error rate concerning varying numbers of decision trees for predicting the attributes: (a) short-circuit current density (J_{SC}), (b) open-circuit voltage (V_{OC}), (c) fill factor (FF), and (d) power conversion efficiency (PCE).

The performance of the machine learning algorithm in predicting each attribute can be interpreted based on the provided regression error values with varying numbers of decision trees. For J_{SC}, as depicted in Fig. 6.15 (a) the initial regression error of 0.65 at lesser number of trees indicates poor predictive capability at lower number of trees. However, there is an improvement as the number of trees increases to 10, resulting in a reduction in the error. This trend continues with no substantial enhancement beyond 10 trees. This indicates that the algorithm gains some predictive power, with even less number of trees. In contrast, for V_{OC}, as depicted in Fig. 6.15 (b) the regression error starts at 0.475 and rapidly reduces to 0 at 10 trees. This implies that the algorithm is highly effective in predicting VOC, as it achieves accurate results even with a small number of trees. The error remains at 0 for 50 trees, reinforcing the algorithm's proficiency in capturing V_{OC} patterns.

Similarly, for FF, as depicted in Fig. 6.15 (c) the initial regression error of 0.65 at 0 trees again signifies limited predictive ability. However, as with J_{SC}, its error diminishes at 10 trees and maintains a consistent performance up to 50 trees. For PCE, as depicted in Fig. 6.15 (d) the highest initial regression error of 0.675 is recorded initially. The error diminishes at 10 trees and maintains consistency from 10-50 trees, indicating that the algorithm reaches a stable level of performance. This shows that predicting V_{OC} achieved impeccable accuracy even with a limited number of trees. It demonstrates commendable performance in capturing J_{SC} and FF trends, with a remarkable reduction in error at 10 trees. While its accuracy in predicting PCE also follows the same trend, the algorithm maintains a reliable and consistent performance across all attributes from 10 to 50 trees. This suggests that the algorithm is equally proficient in predicting all the attributes, and it generally achieves stable and satisfactory performance in predicting all four attributes.

Fig. 6.16 depicts the predicting accuracy for all the four attributes. The graphical depiction provides insights into the concurrence of predicted and observed values, facilitating an understanding of the algorithm's performance in accurately estimating these critical attributes in the context of photovoltaic applications. The testing is performed on 20% of the initial dataset considered. As depicted in Fig. 6.15 the prediction of V_{OC} is very close with the measured values from the data set as shown in Fig. 6.16 (b). The predictive performance of J_{SC}, as depicted in Fig. 6.16 (a), while noteworthy, exhibits a slightly lower level of accuracy when compared to V_{OC}. This is evident from the comparatively higher deviations observed in J_{SC} predictions compared to those in V_{OC}. The predictive performance of FF, as depicted in Fig. 6.16 (c), is noteworthy for the higher values while it deviates slightly for the lower values. As depicted in Fig. 6.16 (d) the PCE prediction follows the same trend as J_{SC} and follows the same notion in predicting all the values of PCE from 0-35%.

The model's performance is assessed using root mean square error (RMSE) and the R-squared (R^2) error, mean squared error (MSE), mean absolute error (MAE), explained variance (EV), median absolute error (MedAE), coefficient of determination (CD) are also calculated for all the four attributes and are tabulated in Table. 6.5. Based on the metrics as depicted in Table. 6.5 the model is performing well on the datasets. Hence, this model suits in predicting all the four attributes. Based on the metrics as depicted in Table. 6.5 the model is performing well on all three datasets (train, validation, and test). is performing The RMSE values are low relatively, signifying that the predictions of the model are generally close to the actual values. The R^2

values are close to 1, which means that the model explains a high proportion of the variance in the data.

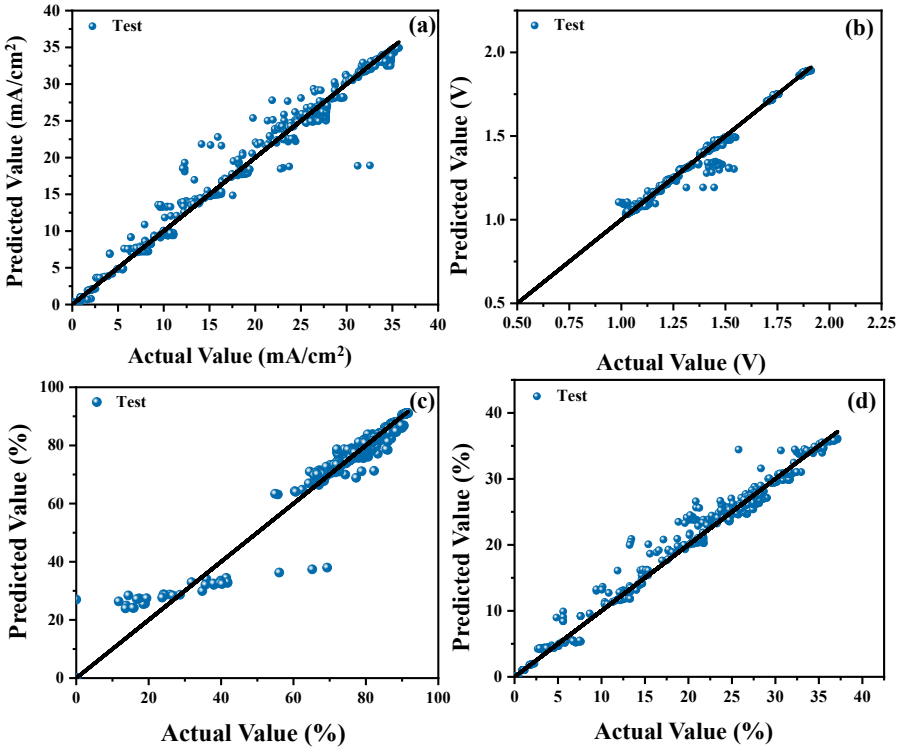

Figure 6.16 Comparative Analysis between Experimentally Measured and Algorithmically Predicted Values for Key Photovoltaic Parameters: (a) Short-Circuit Current Density (J_{SC}), (b) Open-Circuit Voltage (V_{OC}), (c) Fill Factor (FF), and (d) Power Conversion Efficiency (PCE).

The MAE values are also relatively low, indicating that the model's predictions are generally accurate. The EV and CD values are close to 1, which means that the model's predictions are highly correlated with the actual values. The MSE values are also relatively low, indicating that the model's predictions have low variance.

Table 6.5 Evaluation metrics of all the attributes for the train, validation and test data set

Attributes	**Metric/ Dataset type**	**RMSE**	**R^2**	**MAE**	**EV**	**MSE**	**MedAE**	**CD**
V_{OC}	Train	0.0721	0.995	0.019	0.995	0.005	0.0059	0.995
	Validation	0.0707	0.994	0.021	0.994	0.005	0.0068	0.994
	Test	0.0652	0.995	0.020	0.995	0.004	0.0072	0.995

J_{SC}	Train	0.1135	0.987	0.062	0.987	0.012	0.0362	0.987
	Validation	0.1302	0.983	0.066	0.983	0.017	0.0347	0.983
	Test	0.1031	0.989	0.060	0.989	0.010	0.0373	0.989
FF	Train	0.0944	0.991	0.039	0.990	0.008	0.012	0.990
	Validation	0.1173	0.987	0.051	0.987	0.013	0.0152	0.987
	Test	0.0846	0.992	0.037	0.992	0.007	0.0132	0.992
PCE	Train	0.0876	0.992	0.053	0.992	0.007	0.0331	0.992
	Validation	0.086	0.992	0.054	0.992	0.007	0.0376	0.992
	Test	0.089	0.992	0.053	0.992	0.007	0.0327	0.992

6.5 Classification Analysis

The suitability of stacking the layers on top of each other to form a double absorber layer structure is categorized in to 4 classes. If the PCE of a combination is greater than or equal to 35% then that combination is referred to best suitable (BS) class. Between the values 35% and 25% is referred to the class "GOOD". PCE of the combination in between the values 25% and 18% is referred to the class "NOMINAL". PCE of a combination less than18% is referred to the class not suitable ("NS"). As 20% of the total data set is chosen as test set, we have 698 data sets for evaluation to categorize into the 4 classes.

Fig. 6.17 depicts the percentage of absorber combinations that fall under each class. 30.4% of the absorber's combinations have led to the increased efficiency of the PSC devices. Fig. 6.18 depicts the confusion matrix of the test set. The total available data sets for best suitable class are 145 whereas 134 are identified exactly and 11 are misjudged as good class. The total available data sets for good class are 234 whereas 226 are identified exactly and 8 are misjudged as best suitable class.

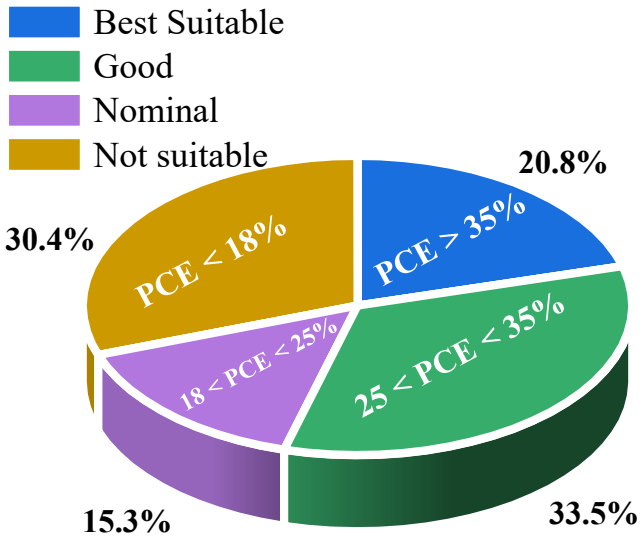

Figure 6.17 Pie-Chart of Absorber classes under random forest classification illustrating the proportions of various absorber materials used in perovskite solar cells and highlighting the prevalence and diversity of materials within the provided classification range.

The total available data sets for nominal class are 107 whereas 86 are identified exactly whereas 19 are misjudged as good class and 3 are misjudged as best suitable class. The total available data sets for not suitable class are 212 whereas 210 are identified exactly and 2 are misjudged as good class and the metrics were tabulated in Table. 6.6.

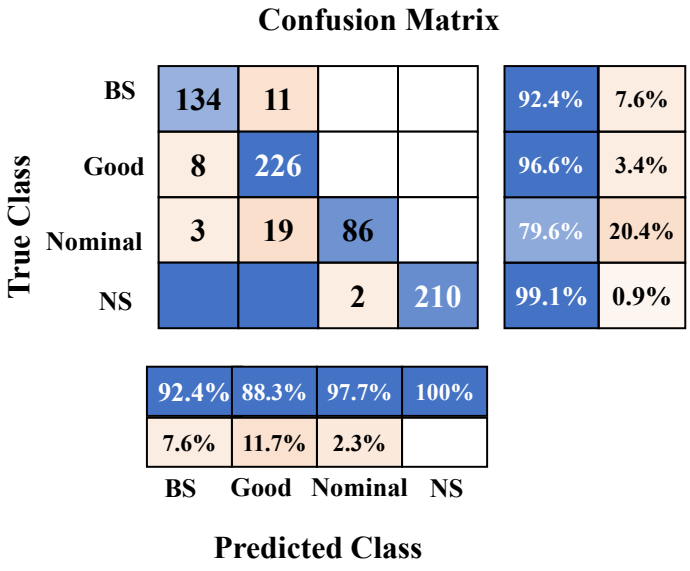

Figure 6.18 Confusion matrix of random forest classification model on the test data set showing the true positive, true negative, false positive, and false negative rates for each absorber class, thereby illustrating the model's accuracy, precision, and ability to correctly classify the different absorber materials.

For the "Good" class, the accuracy is higher at 96.58%, but some samples in this class were misclassified as other classes, leading to a lower recall of 88.28%. However, both precision and F1-score for this class are 96.58%. The "Nominal" class has the lowest accuracy of 79.63%. However, it achieved the highest recall of 97.73%, indicating that most samples in this class were correctly identified. The precision and F1-score for this class are also 79.63%. For the "Not Suitable" class, the model performed exceptionally well with a very high accuracy of 99.06%, correctly identifying 99.06% of the samples in this class. The precision and F1-score for this class are also high at 99.06% and 99.53%, respectively. Based on the results shown in Table. 6.6, the model achieved an overall accuracy of 92.41% for the "Best Suitable" class. This means that it correctly identified 92.41% of the samples in that class. The precision, recall, and F1-score for this class are also 92.41%.

Table 6.6 Evaluation metrics for the RF classification.

Class/ Metrics	Best Suitable	Good	Nominal	Not Suitable
Accuracy	0.92	0.96	0.79	0.99
Precision	0.92	0.96	0.79	0.99
Recall	0.92	0.88	0.97	1.00
F1-Score	0.92	0.92	0.87	0.99

Overall, the model performed well in identifying the "Best Suitable" and "Not Suitable" classes but has little deviations for the "Good" and "Nominal" classes.

6.4 Outcomes

- A staggered band type-II alignment observed between NBGA and WBGA layers enhances electron and hole transport, maximizing charge carrier extraction.
- The MASnI3-$MAPbI_3$ configuration exhibits superior generation and recombination profiles, signifying enhanced charge carrier generation and reduced recombination losses compared to single absorber $MAPbI_3$ PSC.
- The $MASnI_3$-$MAPbI_3$ combination demonstrates excellent absorption efficiency up to 800nm, while the $MAPbI_3$-$CsSnBrI_3$ combination shows lower efficiency due to
- This study achieves impressive efficiencies exceeding 35%, affirming the substantial potential of perovskite materials for robust energy generation in solar cells.

- Leveraging the Random Forest algorithm, the research successfully develops accurate predictive models, based on a dataset of 3800 samples and 20 input features, showcasing the algorithm's efficacy in capturing intricate relationships impacting efficiency.
- The application of RF classification enables the categorization of perovskite structures into four distinct classes, offering a valuable tool for systematic design categorization and a deeper understanding of each class's characteristics.

6.5 Summary

This study provides a comprehensive analysis of double absorber perovskite solar cells (PSCs), emphasizing the operational insights gained from simulated band profiles, energy level alignment, and lattice matching. The staggered band type-II alignment between Narrow Bandgap Absorber (NBGA) and Wide Bandgap Absorber (WBGA) layers facilitates efficient charge carrier transport and extraction. Material comparison highlights the superiority of $MASnI_3$-$MAPbI_3$ over $MAPbI_3$-$CsSnBr_3$, showcasing enhanced charge carrier generation and reduced recombination losses. Absorption characteristics underscore the importance of spectral response, with $MASnI_3$-$MAPbI_3$ demonstrating exceptional efficiency up to 800nm. Lattice matching analysis reveals a coherent interface between $MAPbI_3$ and $MASnI_3$, minimizing lattice mismatch-induced defects and promoting efficient charge transfer. This detailed exploration contributes significant insights into the interplay of material properties, band alignment, and lattice matching in double absorber layered PSCs, paving the way for advancements in perovskite solar cell technology for sustainable and efficient renewable energy solutions. Additionally, the study involves a systematic investigation of various absorber layers in PSCs, achieving high efficiencies surpassing 35%. Machine learning, particularly the Random Forest algorithm, is employed to develop predictive models and classify perovskite structures into four distinct classes. These models offer a valuable tool for categorizing designs and understanding underlying characteristics, contributing to the optimization and design of perovskite solar cells for a cleaner and more sustainable energy future.

CHAPTER 7

Conclusions & Future scope

7.1 Conclusions

In this chapter, we embarked on a comprehensive exploration of absorber optimization techniques aimed at enhancing the performance of perovskite solar cells (PSCs) employing the configuration of Au/HTL/Perovskite ($MAPbI_3$)/ETL/FTO. Our focal point was to mitigate internal recombination at interfaces, a critical factor impacting PSC efficiency. This investigation provided crucial insights into design parameters, including carrier density, doping profiles, and bandgap characteristics, governing recombination mechanisms and overall photovoltaic action in PSCs.

Through meticulous analysis, various factors such as doping, resistance, and internal and interfacial recombination processes are identified, contributing to the observed fill factor (FF) deficits in contemporary PSCs. Our findings highlighted that FF emerged as the performance-limiting parameter in the studied PSC devices. Notably, we established that a robust p-type absorber with a mid-range acceptor density of 10^{16} cm^{-3} was pivotal for achieving high FF and overall efficiency in PSCs. Furthermore, the chapter underscored the sensitivity of FF to the shunt resistance of the device, emphasizing that a shunt resistance exceeding 5 $K\Omega cm^2$ was imperative for optimal FF, open-circuit voltage (V_{oc}), and efficient device operation. Additionally, we delved into the pivotal role of the back contact work function in optimizing FF by reducing recombination.

Expanding the exploration, we delved into the realm of bandgap grading modification, leveraging the wide bandgap tunability inherent in perovskite materials. This approach demonstrated superior spectrum matching and high carrier collection, propelling efficiency towards the Shockley-Queisser limit. Moreover, the research investigated the impact of different bandgap profiling scenarios, ranges, and slopes of the conduction band on device parameters. Surprisingly, our simulations revealed that an extensive range of bandgap tunability was not a prerequisite for achieving maximum efficiency. Instead, a judiciously optimized, modest range of bandgap variation from 1.4 to 1.2 eV at the two extremes of the absorber yielded an impressive power conversion efficiency (PCE) of 31.2%.

Additionally, this study incorporated a pioneering machine learning approach. Leveraging the Random Forest algorithm and a dataset consisting of 3800 samples characterized by 20 input

features and four attributes, we developed predictive models for efficiency estimation. The high accuracy of our predictions demonstrated the effectiveness of the RF algorithm in capturing complex relationships between input parameters and efficiency.

In conclusion, this chapter constitutes a significant stride forward in comprehending the intricate interplay of performance parameters with the structural configuration of perovskite solar cells. The insights garnered offer actionable guidance for the design and optimization of PSCs, promising enhanced efficiency and stability. This work not only paves the way for future research but also provides a blueprint for advancing renewable energy technologies through identified parameters and optimized designs. The collective contributions in this chapter set the stage for an exciting era of innovation and progress in the field of perovskite solar cell technology.

7.2 Future Scope

The exploration of absorber optimization techniques in this chapter lays the foundation for several promising avenues of future research in the field of perovskite solar cell (PSC) technology. Here are some potential directions for further investigation:

Deeper insights into defect engineering and effective passivation strategies could lead to substantial improvements in PSC performance. Investigating advanced passivation materials and techniques tailored to specific interface properties may further reduce recombination. The quest for new perovskite materials with improved optoelectronic properties remains a critical area of research. Exploring alternative perovskite compositions and heterostructures may yield materials with enhanced stability, efficiency, and light-harvesting capabilities. Long-term stability and reliability of PSCs under real-world operating conditions are crucial for their practical deployment. Systematic studies on degradation mechanisms, encapsulation strategies, and material robustness will be instrumental in advancing the commercial viability of PSC technology.

The future integration of Machine Learning (ML) algorithms in perovskite solar cell (PSC) research holds immense promise for advancing renewable energy technology. Researchers can delve into more advanced ML models, potentially incorporating deep learning techniques like Convolutional Neural Networks (CNNs) or Recurrent Neural Networks (RNNs) for intricate pattern recognition and prediction tasks. Transfer learning, where pre-trained models are fine-tuned for PSC-specific tasks, can expedite accurate predictive modeling. Ensemble learning methods, such as Random Forests or Gradient Boosting, offer potential for combining diverse

information sources for robust predictions. Emphasis on explainability and interpretability in ML models can provide valuable insights into the factors shaping PSC performance. Techniques like SHapley Additive exPlanations (SHAP) values or LIME can enhance model transparency. Augmenting datasets through techniques like Generative Adversarial Networks (GANs) or Variational Autoencoders (VAEs) can overcome limitations posed by limited experimental data. Active learning approaches can strategically select data points for validation, optimizing resource utilization. Integration of ML with multi-objective optimization techniques enables balanced trade-offs between efficiency, stability, and cost-effectiveness. Finally, translating ML-based optimizations to large-scale manufacturing environments is pivotal for practical implementation in commercial PSC production. These avenues collectively represent a dynamic future for the intersection of ML and PSC technology, poised to revolutionize the renewable energy landscape.

Transitioning from laboratory-scale to large-scale manufacturing is a critical step for the widespread adoption of PSCs. Research focused on scalable fabrication techniques, cost-effective materials, and production processes will be pivotal in realizing the commercial potential of PSCs. By delving into these future research avenues, the field of perovskite solar cell technology stands poised to make significant strides towards achieving sustainable and efficient renewable energy solutions for the global energy landscape.

References

[1] P. Voosen, "Global temperatures in 2020 tied record highs," ed: American Association for the Advancement of Science, 2021.

[2] J. P. Aryal, T. B. Sapkota, D. B. Rahut, P. Marenya, and C. M. Stirling, "Climate risks and adaptation strategies of farmers in East Africa and South Asia," *Scientific reports,* vol. 11, no. 1, p. 10489, 2021.

[3] S. Kumar and A. Pandey, "Current developments in biotechnology and bioengineering and waste treatment processes for energy generation: an introduction," in *Current developments in biotechnology and bioengineering*: Elsevier, 2019, pp. 1-9.

[4] https://www.iea.org/reports/key-world-energy-statistics-2021 (accessed 2021).

[5] G. J. Herbert, S. Iniyan, E. Sreevalsan, and S. Rajapandian, "A review of wind energy technologies," *Renewable and sustainable energy Reviews,* vol. 11, no. 6, pp. 1117-1145, 2007.

[6] J. Romero-Ramos, J. Gil, J. Cardemil, R. Escobar, I. Arias, and M. Pérez-García, "A GIS-AHP approach for determining the potential of solar energy to meet the thermal demand in southeastern Spain productive enclaves," *Renewable and Sustainable Energy Reviews,* vol. 176, p. 113205, 2023.

[7] H. Kulasekara and V. Seynulabdeen, "A review of geothermal energy for future power generation," in *2019 5th International Conference on Advances in Electrical Engineering (ICAEE)*, 2019: IEEE, pp. 223-228.

[8] J. Zhang, W. Zhang, H.-M. Cheng, and S. R. P. Silva, "Critical review of recent progress of flexible perovskite solar cells," *Materials Today,* vol. 39, pp. 66-88, 2020.

[9] S. Gorjian, H. Sharon, H. Ebadi, K. Kant, F. B. Scavo, and G. M. Tina, "Recent technical advancements, economics and environmental impacts of floating photovoltaic solar energy conversion systems," *Journal of Cleaner Production,* vol. 278, p. 124285, 2021.

[10] M. Kumar, H. M. Niyaz, and R. Gupta, "Challenges and opportunities towards the development of floating photovoltaic systems," *Solar Energy Materials and Solar Cells,* vol. 233, p. 111408, 2021.

[11] K. Yoshikawa *et al.*, "Silicon heterojunction solar cell with interdigitated back contacts for a photoconversion efficiency over 26%," *Nature energy,* vol. 2, no. 5, pp. 1-8, 2017.

[12] D. M. Chapin, C. S. Fuller, and G. L. Pearson, "A new silicon p-n junction photocell for converting solar radiation into electrical power," *Journal of applied physics,* vol. 25, no. 5, pp. 676-677, 1954.

[13] M. A. Green, "Third generation photovoltaics," 2006.

[14] https://www.nrel.gov/pv/assets/images/efficiency-chart.png (accessed 2021).

[15] C. Waida, A. Alivisatos, and D. Kammen, "Material availability expands the opportunity for large-scale photovoltaic development," *Environ. Sci. Technol,* vol. 43, pp. 2072-2077, 2009.

[16] M. A. Green, "Crystalline and thin-film silicon solar cells: state of the art and future potential," *Solar energy,* vol. 74, no. 3, pp. 181-192, 2003.

[17] R. E. Schropp and M. Zeman, *Amorphous and microcrystalline silicon solar cells: modeling, materials and device technology*. Springer, 1998.

[18] M. Green, E. Dunlop, J. Hohl-Ebinger, M. Yoshita, N. Kopidakis, and X. Hao, "Solar cell efficiency tables (version 57)," *Progress in photovoltaics: research and applications,* vol. 29, no. 1, pp. 3-15, 2021.

[19] J. Ramanujam *et al.*, "Flexible CIGS, CdTe and a-Si: H based thin film solar cells: A review," *Progress in Materials Science,* vol. 110, p. 100619, 2020.

[20] F. C. Krebs, "Fabrication and processing of polymer solar cells: A review of printing and coating techniques," *Solar energy materials and solar cells,* vol. 93, no. 4, pp. 394-412, 2009.

[21] A. J. Nozik, "Quantum dot solar cells," *Physica E: Low-dimensional Systems and Nanostructures,* vol. 14, no. 1-2, pp. 115-120, 2002.

[22] T. Tiedje, E. Yablonovitch, G. D. Cody, and B. G. Brooks, "Limiting efficiency of silicon solar cells," *IEEE Transactions on electron devices,* vol. 31, no. 5, pp. 711-716, 1984.

[23] S. De Wolf, A. Descoeudres, Z. C. Holman, and C. Ballif, "High-efficiency silicon heterojunction solar cells: A review," *green,* vol. 2, no. 1, pp. 7-24, 2012.

[24] H. J. Snaith, "Present status and future prospects of perovskite photovoltaics," *Nature materials,* vol. 17, no. 5, pp. 372-376, 2018.

[25] Y. Sawle and M. Thirunavukkarasu, "Techno-economic comparative assessment of an off-grid hybrid renewable energy system for electrification of remote area," in *Design, analysis, and applications of renewable energy systems*: Elsevier, 2021, pp. 199-247.

[26] A. Ameur, A. Berrada, K. Loudiyi, and R. Adomatis, "Performance and energetic modeling of hybrid PV systems coupled with battery energy storage," in *Hybrid Energy System Models*: Elsevier, 2021, pp. 195-238.

[27] I. M. Alarifi, "Advanced selection materials in solar cell efficiency and their properties-A comprehensive review," *Materials Today: Proceedings,* 2021.
[28] E. F. Fernández, A. J. García-Loureiro, and G. P. Smestad, "Multijunction concentrator solar cells: analysis and fundamentals," *High concentrator photovoltaics: fundamentals, engineering and power plants,* pp. 9-37, 2015.
[29] Q. Liu *et al.*, "18% Efficiency organic solar cells," *Science Bulletin,* vol. 65, no. 4, pp. 272-275, 2020.
[30] K. Zhao *et al.*, "Boosting power conversion efficiencies of quantum-dot-sensitized solar cells beyond 8% by recombination control," *Journal of the American Chemical Society,* vol. 137, no. 16, pp. 5602-5609, 2015.
[31] H. Rao, M. Zhou, Z. Pan, and X. Zhong, "Quantum dot materials engineering boosting the quantum dot sensitized solar cell efficiency over 13%," *Journal of Materials Chemistry A,* vol. 8, no. 20, pp. 10233-10241, 2020.
[32] Z. Yang, A. Rajagopal, and A. K. Y. Jen, "Ideal bandgap organic–inorganic hybrid perovskite solar cells," *Advanced Materials,* vol. 29, no. 47, p. 1704418, 2017.
[33] H. Wang, X. Liu, and Z. M. Zhang, "Absorption coefficients of crystalline silicon at wavelengths from 500 nm to 1000 nm," *International Journal of Thermophysics,* vol. 34, no. 2, pp. 213-225, 2013.
[34] H.-S. Kim *et al.*, "Lead iodide perovskite sensitized all-solid-state submicron thin film mesoscopic solar cell with efficiency exceeding 9%," *Scientific reports,* vol. 2, no. 1, p. 591, 2012.
[35] M. Grätzel, "The light and shade of perovskite solar cells," *Nature materials,* vol. 13, no. 9, pp. 838-842, 2014.
[36] S. Brittman, G. W. P. Adhyaksa, and E. C. Garnett, "The expanding world of hybrid perovskites: materials properties and emerging applications," *MRS communications,* vol. 5, no. 1, pp. 7-26, 2015.
[37] C. Longeaud, A. F. Allah, J. Schmidt, M. El Yaakoubi, S. Berson, and N. Lemaitre, "Determination of diffusion lengths in organic semiconductors: Correlation with solar cell performances," *Organic Electronics,* vol. 31, pp. 253-257, 2016.
[38] D. Shi *et al.*, "Low trap-state density and long carrier diffusion in organolead trihalide perovskite single crystals," *Science,* vol. 347, no. 6221, pp. 519-522, 2015.
[39] A. Kojima, K. Teshima, Y. Shirai, and T. Miyasaka, "Organometal halide perovskites as visible-light sensitizers for photovoltaic cells," *Journal of the American Chemical Society,* vol. 131, no. 17, pp. 6050-6051, 2009.
[40] M. A. Green, A. Ho-Baillie, and H. J. Snaith, "The emergence of perovskite solar cells," *Nature photonics,* vol. 8, no. 7, pp. 506-514, 2014.
[41] M. A. Green and A. Ho-Baillie, "Perovskite solar cells: the birth of a new era in photovoltaics," *ACS Energy Letters,* vol. 2, no. 4, pp. 822-830, 2017.
[42] A. Rohatgi *et al.*, "26.7% Efficient 4-Terminal Perovskite–Silicon Tandem Solar Cell Composed of a High-Performance Semitransparent Perovskite Cell and a Doped Poly-Si/SiO x Passivating Contact Silicon Cell," *IEEE Journal of Photovoltaics,* vol. 10, no. 2, pp. 417-422, 2020.
[43] https://www.nrel.gov/pv/cell-efficiency.html (accessed 2023).
[44] S. Kashyap, R. Pandey, J. Madan, and M. K. Mohammed, "Reliability Test of 21% Efficient Flexible Perovskite Solar Cell under Concave, Convex and Sinusoidal Bending," *IEEE Transactions on Device and Materials Reliability,* 2023.
[45] S. Mazumdar, Y. Zhao, and X. Zhang, "Stability of perovskite solar cells: degradation mechanisms and remedies," *Frontiers in Electronics,* vol. 2, p. 712785, 2021.
[46] K. Domanski *et al.*, "Not all that glitters is gold: metal-migration-induced degradation in perovskite solar cells," *ACS nano,* vol. 10, no. 6, pp. 6306-6314, 2016.
[47] M. A. Davis, R. Sweat, and Z. Yu, "Predictive Modeling of Cracking Behaviors in Flexible Perovskite Solar Cells," *IEEE Journal on Flexible Electronics,* vol. 1, no. 4, pp. 231-235, 2022.
[48] J.-P. Correa-Baena *et al.*, "Promises and challenges of perovskite solar cells," *Science,* vol. 358, no. 6364, pp. 739-744, 2017.
[49] C. Eames, J. M. Frost, P. R. Barnes, B. C. O'regan, A. Walsh, and M. S. Islam, "Ionic transport in hybrid lead iodide perovskite solar cells," *Nature communications,* vol. 6, no. 1, p. 7497, 2015.
[50] Z. Chen, H. Li, Y. Tang, X. Huang, D. Ho, and C.-S. Lee, "Shape-controlled synthesis of organolead halide perovskite nanocrystals and their tunable optical absorption," *Materials Research Express,* vol. 1, no. 1, p. 015034, 2014.
[51] A. Bhalla, R. Guo, and R. Roy, "The perovskite structure—a review of its role in ceramic science and technology," *Materials research innovations,* vol. 4, no. 1, pp. 3-26, 2000.
[52] T. Baikie *et al.*, "Synthesis and crystal chemistry of the hybrid perovskite (CH 3 NH 3) PbI 3 for solid-state sensitised solar cell applications," *Journal of Materials Chemistry A,* vol. 1, no. 18, pp. 5628-5641, 2013.

[53] C. C. Stoumpos, C. D. Malliakas, and M. G. Kanatzidis, "Semiconducting tin and lead iodide perovskites with organic cations: phase transitions, high mobilities, and near-infrared photoluminescent properties," *Inorganic chemistry,* vol. 52, no. 15, pp. 9019-9038, 2013.
[54] H. J. Snaith, "Perovskites: the emergence of a new era for low-cost, high-efficiency solar cells," *The journal of physical chemistry letters,* vol. 4, no. 21, pp. 3623-3630, 2013.
[55] S. D. Stranks and H. J. Snaith, "Metal-halide perovskites for photovoltaic and light-emitting devices," *Nature nanotechnology,* vol. 10, no. 5, pp. 391-402, 2015.
[56] H. S. Jung and N. G. Park, "Perovskite solar cells: from materials to devices," *small,* vol. 11, no. 1, pp. 10-25, 2015.
[57] F. M. Rombach, S. A. Haque, and T. J. Macdonald, "Lessons learned from spiro-OMeTAD and PTAA in perovskite solar cells," *Energy & Environmental Science,* vol. 14, no. 10, pp. 5161-5190, 2021.
[58] B. Tan *et al.*, "LiTFSI-free spiro-OMeTAD-based perovskite solar cells with power conversion efficiencies exceeding 19%," *Advanced Energy Materials,* vol. 9, no. 32, p. 1901519, 2019.
[59] S. Y. Park and K. Zhu, "Advances in SnO2 for efficient and stable n–i–p perovskite solar cells," *Advanced materials,* vol. 34, no. 27, p. 2110438, 2022.
[60] J. Luo, Y. Wang, and Q. Zhang, "Progress in perovskite solar cells based on ZnO nanostructures," *Solar Energy,* vol. 163, pp. 289-306, 2018.
[61] Y. Wang *et al.*, "PTAA as Efficient Hole Transport Materials in Perovskite Solar Cells: A Review," *Solar RRL,* vol. 6, no. 8, p. 2200234, 2022.
[62] J. Kong *et al.*, "CO2 doping of organic interlayers for perovskite solar cells," *Nature,* vol. 594, no. 7861, pp. 51-56, 2021.
[63] Q. Wang, C.-C. Chueh, M. Eslamian, and A. K.-Y. Jen, "Modulation of PEDOT: PSS pH for efficient inverted perovskite solar cells with reduced potential loss and enhanced stability," *ACS Applied Materials & Interfaces,* vol. 8, no. 46, pp. 32068-32076, 2016.
[64] K. Jiang *et al.*, "Inverted planar perovskite solar cells based on CsI-doped PEDOT: PSS with efficiency beyond 20% and small energy loss," *Journal of Materials Chemistry A,* vol. 7, no. 38, pp. 21662-21667, 2019.
[65] P. K. Kung *et al.*, "A review of inorganic hole transport materials for perovskite solar cells," *Advanced Materials Interfaces,* vol. 5, no. 22, p. 1800882, 2018.
[66] I. Hussain, H. P. Tran, J. Jaksik, J. Moore, N. Islam, and M. J. Uddin, "Functional materials, device architecture, and flexibility of perovskite solar cell," *Emergent Materials,* vol. 1, pp. 133-154, 2018.
[67] P. Wang *et al.*, "Advances in the structure and materials of perovskite solar cells," *Research on Chemical Intermediates,* vol. 42, pp. 625-639, 2016.
[68] L. Wang, G.-R. Li, Q. Zhao, and X.-P. Gao, "Non-precious transition metals as counter electrode of perovskite solar cells," *Energy Storage Materials,* vol. 7, pp. 40-47, 2017.
[69] K. Wu *et al.*, "Temperature-dependent excitonic photoluminescence of hybrid organometal halide perovskite films," *Physical Chemistry Chemical Physics,* vol. 16, no. 41, pp. 22476-22481, 2014.
[70] Y. Kanemitsu, "Luminescence spectroscopy of lead-halide perovskites: materials properties and application as photovoltaic devices," *Journal of Materials Chemistry C,* vol. 5, no. 14, pp. 3427-3437, 2017.
[71] W. E. Sha, X. Ren, L. Chen, and W. C. Choy, "The efficiency limit of CH3NH3PbI3 perovskite solar cells," *Applied Physics Letters,* vol. 106, no. 22, p. 221104, 2015.
[72] L. Yue, B. Yan, M. Attridge, and Z. Wang, "Light absorption in perovskite solar cell: Fundamentals and plasmonic enhancement of infrared band absorption," *Solar Energy,* vol. 124, pp. 143-152, 2016.
[73] Z. Xu *et al.*, "Balancing energy-level difference for efficient nip perovskite solar cells with Cu electrode," *Energy Material Advances,* vol. 2022, 2022.
[74] J. Wu *et al.*, "A comparison of charge carrier dynamics in organic and perovskite solar cells," *Advanced Materials,* vol. 34, no. 2, p. 2101833, 2022.
[75] A. Niemegeers, M. Burgelman, K. Decock, J. Verschraegen, and S. Degrave, "SCAPS manual," *University of Gent,* vol. 13, 2014.
[76] T. Minemoto and M. Murata, "Device modeling of perovskite solar cells based on structural similarity with thin film inorganic semiconductor solar cells," *Journal of applied physics,* vol. 116, no. 5, p. 054505, 2014.
[77] M. Burgelman, K. Decock, A. Niemegeers, J. Verschraegen, and S. Degrave, "SCAPS manual," *February,* 2016.
[78] K. Chakraborty, M. G. Choudhury, and S. Paul, "Numerical study of Cs2TiX6 (X= Br−, I−, F− and Cl−) based perovskite solar cell using SCAPS-1D device simulation," *Solar Energy,* vol. 194, pp. 886-892, 2019.

[79] M. Kumar, A. Raj, A. Kumar, and A. Anshul, "An optimized lead-free formamidinium Sn-based perovskite solar cell design for high power conversion efficiency by SCAPS simulation," *Optical Materials,* vol. 108, p. 110213, 2020.
[80] D. Dwivedi, "Modeling of Photovoltaic Solar Cell Based on $CuSbS_2$ Absorber for the Enhancement of Performance," *IEEE Transactions on Electron Devices,* vol. 68, no. 3, pp. 1121-1128, 2021.
[81] B. S. Sengar, V. Garg, A. Kumar, and P. Dwivedi, "Numerical simulation: Design of high-efficiency planar pn homojunction perovskite solar cells," *IEEE Transactions on Electron Devices,* vol. 68, no. 5, pp. 2360-2364, 2021.
[82] A. Kaity, S. Singh, and S. K. Pandey, "Optimal design and photovoltaic performance of eco friendly, stable and efficient perovskite solar cell," *Superlattices and Microstructures,* vol. 156, p. 106972, 2021.
[83] M. Mousa, F. Z. Amer, R. I. Mubarak, and A. Saeed, "Simulation of optimized high-current tandem solar-cells with efficiency beyond 41%," *IEEE Access,* vol. 9, pp. 49724-49737, 2021.
[84] D. Chakraborty, S. Somay, and S. K. Pandey, "Numerical analysis of a novel HTL-free perovskite solar cell with gradient doping and a WS_2 interlayer," *Micro and Nanostructures,* vol. 163, p. 107149, 2022.
[85] S. K. Pandey and S. Somay, "Device engineering approach toward stable, efficient, and eco-friendly perovskite solar cell," *IEEE Transactions on Electron Devices,* vol. 68, no. 3, pp. 1142-1148, 2021.
[86] R. Shukla, R. R. Kumar, and S. K. Pandey, "Theoretical study of charge carrier lifetime and recombination on the performance of eco-friendly perovskite solar cell," *IEEE Transactions on Electron Devices,* vol. 68, no. 7, pp. 3446-3452, 2021.
[87] H.-S. Kim *et al.*, "Lead iodide perovskite sensitized all-solid-state submicron thin film mesoscopic solar cell with efficiency exceeding 9%," *Scientific reports,* vol. 2, no. 1, pp. 1-7, 2012.
[88] J. Burschka *et al.*, "Sequential deposition as a route to high-performance perovskite-sensitized solar cells," *Nature,* vol. 499, no. 7458, pp. 316-319, 2013.
[89] M. Liu, M. B. Johnston, and H. J. Snaith, "Efficient planar heterojunction perovskite solar cells by vapour deposition," *Nature,* vol. 501, no. 7467, pp. 395-398, 2013.
[90] J. Liang *et al.*, "All-inorganic perovskite solar cells," *Journal of the American Chemical Society,* vol. 138, no. 49, pp. 15829-15832, 2016.
[91] J. Liang *et al.*, "CsPb0. 9Sn0. 1IBr2 based all-inorganic perovskite solar cells with exceptional efficiency and stability," *Journal of the American Chemical Society,* vol. 139, no. 40, pp. 14009-14012, 2017.
[92] J. Liang, J. Liu, and Z. Jin, "All-Inorganic Halide Perovskites for Optoelectronics: Progress and Prospects," *Solar Rrl,* vol. 1, no. 10, p. 1700086, 2017.
[93] S. D. Stranks *et al.*, "Electron-hole diffusion lengths exceeding 1 micrometer in an organometal trihalide perovskite absorber," *Science,* vol. 342, no. 6156, pp. 341-344, 2013.
[94] G. Xing *et al.*, "Long-range balanced electron-and hole-transport lengths in organic-inorganic CH3NH3PbI3," *Science,* vol. 342, no. 6156, pp. 344-347, 2013.
[95] C. Wehrenfennig, G. E. Eperon, M. B. Johnston, H. J. Snaith, and L. M. Herz, "High charge carrier mobilities and lifetimes in organolead trihalide perovskites," *Advanced materials,* vol. 26, no. 10, pp. 1584-1589, 2014.
[96] B. Derkowska-Zielinska *et al.*, "Photovoltaic cells with various azo dyes as components of the active layer," *Solar Energy,* vol. 203, pp. 19-24, 2020.
[97] W. Yan *et al.*, "Determination of complex optical constants and photovoltaic device design of all-inorganic CsPbBr 3 perovskite thin films," *Optics express,* vol. 28, no. 10, pp. 15706-15717, 2020.
[98] Y. Xia *et al.*, "Pseudohalide substitution and potassium doping in FA0. 98K0. 02Pb (SCN) 2I for high-stability hole-conductor-free perovskite solar cells," *Journal of Power Sources,* vol. 494, p. 229781, 2021.
[99] W. Tress, "Perovskite solar cells on the way to their radiative efficiency limit–insights into a success story of high open-circuit voltage and low recombination," *Advanced Energy Materials,* vol. 7, no. 14, p. 1602358, 2017.
[100] R. E. Brandt, V. Stevanović, D. S. Ginley, and T. Buonassisi, "Identifying defect-tolerant semiconductors with high minority-carrier lifetimes: beyond hybrid lead halide perovskites," *Mrs Communications,* vol. 5, no. 2, pp. 265-275, 2015.
[101] A. Buin *et al.*, "Materials processing routes to trap-free halide perovskites," *Nano letters,* vol. 14, no. 11, pp. 6281-6286, 2014.
[102] Q. Lin, A. Armin, R. C. R. Nagiri, P. L. Burn, and P. Meredith, "Electro-optics of perovskite solar cells," *Nature Photonics,* vol. 9, no. 2, pp. 106-112, 2015.
[103] W. Shockley and H. J. Queisser, "Detailed balance limit of efficiency of p-n junction solar cells," *Journal of applied physics,* vol. 32, no. 3, pp. 510-519, 1961.
[104] M. A. Green and S. P. Bremner, "Energy conversion approaches and materials for high-efficiency photovoltaics," *Nature materials,* vol. 16, no. 1, pp. 23-34, 2017.

[105] Z. Chen *et al.*, "Single-crystal MAPbI3 perovskite solar cells exceeding 21% power conversion efficiency," *ACS Energy Letters,* vol. 4, no. 6, pp. 1258-1259, 2019.
[106] Y. Cao *et al.*, "Efficient and stable MAPbI3 perovskite solar cells achieved via chlorobenzene/perylene mixed anti-solvent," *Solar Energy,* vol. 220, pp. 251-257, 2021.
[107] X. Zheng *et al.*, "Defect passivation in hybrid perovskite solar cells using quaternary ammonium halide anions and cations," *Nature Energy,* vol. 2, no. 7, pp. 1-9, 2017.
[108] N. J. Jeon *et al.*, "A fluorene-terminated hole-transporting material for highly efficient and stable perovskite solar cells," *Nature Energy,* vol. 3, no. 8, pp. 682-689, 2018.
[109] M. Abdi-Jalebi *et al.*, "Maximizing and stabilizing luminescence from halide perovskites with potassium passivation," *Nature,* vol. 555, no. 7697, pp. 497-501, 2018.
[110] C. Ma and N.-G. Park, "A realistic methodology for 30% efficient perovskite solar cells," *Chem,* vol. 6, no. 6, pp. 1254-1264, 2020.
[111] C. M. Wolff, F. Zu, A. Paulke, L. P. Toro, N. Koch, and D. Neher, "Reduced Interface-Mediated Recombination for High Open-Circuit Voltages in CH3NH3PbI3 Solar Cells," *Advanced materials,* vol. 29, no. 28, p. 1700159, 2017.
[112] D. Luo *et al.*, "Enhanced photovoltage for inverted planar heterojunction perovskite solar cells," *Science,* vol. 360, no. 6396, pp. 1442-1446, 2018.
[113] H. Tan *et al.*, "Efficient and stable solution-processed planar perovskite solar cells via contact passivation," *Science,* vol. 355, no. 6326, pp. 722-726, 2017.
[114] M. I. Saidaminov *et al.*, "Suppression of atomic vacancies via incorporation of isovalent small ions to increase the stability of halide perovskite solar cells in ambient air," *Nature Energy,* vol. 3, no. 8, pp. 648-654, 2018.
[115] Z. Wang, Q. Lin, F. P. Chmiel, N. Sakai, L. M. Herz, and H. J. Snaith, "Efficient ambient-air-stable solar cells with 2D–3D heterostructured butylammonium-caesium-formamidinium lead halide perovskites," *Nature Energy,* vol. 2, no. 9, pp. 1-10, 2017.
[116] Y. Hou *et al.*, "A generic interface to reduce the efficiency-stability-cost gap of perovskite solar cells," *Science,* vol. 358, no. 6367, pp. 1192-1197, 2017.
[117] M. Stolterfoht *et al.*, "Visualization and suppression of interfacial recombination for high-efficiency large-area pin perovskite solar cells," *Nature Energy,* vol. 3, no. 10, pp. 847-854, 2018.
[118] M. Saliba *et al.*, "Incorporation of rubidium cations into perovskite solar cells improves photovoltaic performance," *Science,* vol. 354, no. 6309, pp. 206-209, 2016.
[119] H. Tan *et al.*, "Dipolar cations confer defect tolerance in wide-bandgap metal halide perovskites," *Nature communications,* vol. 9, no. 1, pp. 1-10, 2018.
[120] K. A. Bush *et al.*, "Compositional engineering for efficient wide band gap perovskites with improved stability to photoinduced phase segregation," *ACS Energy Letters,* vol. 3, no. 2, pp. 428-435, 2018.
[121] G. Longo, C. Momblona, M.-G. La-Placa, L. n. Gil-Escrig, M. Sessolo, and H. J. Bolink, "Fully vacuum-processed wide band gap mixed-halide perovskite solar cells," *ACS Energy Letters,* vol. 3, no. 1, pp. 214-219, 2017.
[122] W. S. Yang *et al.*, "Iodide management in formamidinium-lead-halide–based perovskite layers for efficient solar cells," *Science,* vol. 356, no. 6345, pp. 1376-1379, 2017.
[123] H. Zhou *et al.*, "Interface engineering of highly efficient perovskite solar cells," *Science,* vol. 345, no. 6196, pp. 542-546, 2014.
[124] S. Rühle, "Tabulated values of the Shockley–Queisser limit for single junction solar cells," *Solar Energy,* vol. 130, pp. 139-147, 2016.
[125] NREL. "Best Research-Cell Efficiency Chart." (accessed.
[126] N. Tanaka, "Technology roadmap-solar photovoltaic energy," *International energy agency report. Paris/France,* 2010.
[127] S. Sharma, K. K. Jain, and A. Sharma, "Solar cells: in research and applications—a review," *Materials Sciences and Applications,* vol. 6, no. 12, p. 1145, 2015.
[128] K. Chopra, P. Paulson, and V. Dutta, "Thin-film solar cells: an overview," *Progress in Photovoltaics: Research and applications,* vol. 12, no. 2-3, pp. 69-92, 2004.
[129] Z. Liu *et al.*, "Efficient and stable FA-rich perovskite photovoltaics: from material properties to device optimization," *Advanced Energy Materials,* vol. 12, no. 18, p. 2200111, 2022.
[130] R. Corkish, "Solar cells. Encyclopedia of Energy Vol. 5," ed: Elsevier, 2004.
[131] J.-H. Im, C.-R. Lee, J.-W. Lee, S.-W. Park, and N.-G. Park, "6.5% efficient perovskite quantum-dot-sensitized solar cell," *Nanoscale,* vol. 3, no. 10, pp. 4088-4093, 2011.
[132] M. M. Lee, J. Teuscher, T. Miyasaka, T. N. Murakami, and H. J. Snaith, "Efficient hybrid solar cells based on meso-superstructured organometal halide perovskites," *Science,* vol. 338, no. 6107, pp. 643-647, 2012.

[133] T. Dai *et al.*, "Strategies for high-performance large-area perovskite solar cells toward commercialization," *Crystals,* vol. 11, no. 3, p. 295, 2021.
[134] P. Dey, H. Singh, R. K. Gupta, D. Goswami, and T. Maiti, "Organic-inorganic hybrid halide perovskites impregnated with Group 1 and 15 elements for solar cell application," *Journal of Physics and Chemistry of Solids,* vol. 144, p. 109518, 2020.
[135] S. Kadian, N. K. Tailor, N. Chaulagain, K. Shankar, S. Satapathi, and G. Manik, "Effect of sulfur-doped graphene quantum dots incorporation on morphological, optical and electron transport properties of CH3NH3PbBr3 perovskite thin films," *Journal of Materials Science: Materials in Electronics,* vol. 32, no. 13, pp. 17406-17417, 2021.
[136] R. Shukla, R. R. Kumar, D. Punetha, and S. K. Pandey, "Design perspective, fabrication, and performance analysis of formamidinium tin halide perovskite solar cell," *IEEE Journal of Photovoltaics,* 2023.
[137] Y. Liu *et al.*, "High efficiency tandem thin-perovskite/polymer solar cells with a graded recombination layer," *ACS applied materials & interfaces,* vol. 8, no. 11, pp. 7070-7076, 2016.
[138] W. S. Yang *et al.*, "High-performance photovoltaic perovskite layers fabricated through intramolecular exchange," *Science,* vol. 348, no. 6240, pp. 1234-1237, 2015.
[139] D. Bi *et al.*, "Polymer-templated nucleation and crystal growth of perovskite films for solar cells with efficiency greater than 21%," *Nature Energy,* vol. 1, no. 10, pp. 1-5, 2016.
[140] N. J. Jeon *et al.*, "A fluorene-terminated hole-transporting material for highly efficient and stable perovskite solar cells," *Nature Energy,* vol. 3, no. 8, pp. 682-689, 2018.
[141] M. Kim *et al.*, "Methylammonium chloride induces intermediate phase stabilization for efficient perovskite solar cells," *Joule,* vol. 3, no. 9, pp. 2179-2192, 2019.
[142] A. Abate *et al.*, "Supramolecular halogen bond passivation of organic–inorganic halide perovskite solar cells," *Nano letters,* vol. 14, no. 6, pp. 3247-3254, 2014.
[143] H.-J. Du, W.-C. Wang, and J.-Z. Zhu, "Device simulation of lead-free CH3NH3SnI3 perovskite solar cells with high efficiency," *Chinese Physics B,* vol. 25, no. 10, p. 108802, 2016.
[144] S. Do Sung, D. P. Ojha, J. S. You, J. Lee, J. Kim, and W. I. Lee, "50 nm sized spherical TiO 2 nanocrystals for highly efficient mesoscopic perovskite solar cells," *Nanoscale,* vol. 7, no. 19, pp. 8898-8906, 2015.
[145] T. Leijtens *et al.*, "Electronic properties of meso-superstructured and planar organometal halide perovskite films: charge trapping, photodoping, and carrier mobility," *ACS nano,* vol. 8, no. 7, pp. 7147-7155, 2014.
[146] B. A. Al-Asbahi, S. M. Qaid, M. Hezam, I. Bedja, H. M. Ghaithan, and A. S. Aldwayyan, "Effect of deposition method on the structural and optical properties of CH3NH3PbI3 perovskite thin films," *Optical Materials,* vol. 103, p. 109836, 2020.
[147] L. J. Phillips *et al.*, "Dispersion relation data for methylammonium lead triiodide perovskite deposited on a (100) silicon wafer using a two-step vapour-phase reaction process," *Data in brief,* vol. 5, pp. 926-928, 2015.
[148] A. Miyata *et al.*, "Direct measurement of the exciton binding energy and effective masses for charge carriers in organic–inorganic tri-halide perovskites," *Nature Physics,* vol. 11, no. 7, pp. 582-587, 2015.
[149] Z. Yang *et al.*, "Unraveling the exciton binding energy and the dielectric constant in single-crystal methylammonium lead triiodide perovskite," *The journal of physical chemistry letters,* vol. 8, no. 8, pp. 1851-1855, 2017.
[150] A. Karim, M. Khan, and M. Hossain, "Temperature dependency of excitonic effective mass and charge carrier conduction mechanism in CH3NH3PbI3− xClx thin films," *Scientific reports,* vol. 11, no. 1, pp. 1-10, 2021.
[151] L. M. Herz, "Charge-carrier dynamics in organic-inorganic metal halide perovskites," *Annual review of physical chemistry,* vol. 67, pp. 65-89, 2016.
[152] C. Motta, F. El-Mellouhi, and S. Sanvito, "Charge carrier mobility in hybrid halide perovskites," *Scientific reports,* vol. 5, no. 1, pp. 1-8, 2015.
[153] S. Kundu and T. L. Kelly, "In situ studies of the degradation mechanisms of perovskite solar cells," *EcoMat,* vol. 2, no. 2, p. e12025, 2020.
[154] G. J. A. Wetzelaer, M. Scheepers, A. M. Sempere, C. Momblona, J. Ávila, and H. J. Bolink, "Trap-assisted non-radiative recombination in organic–inorganic perovskite solar cells," *Advanced Materials,* vol. 27, no. 11, pp. 1837-1841, 2015.
[155] W. Tress, N. Marinova, O. Inganäs, M. K. Nazeeruddin, S. M. Zakeeruddin, and M. Graetzel, "Predicting the open-circuit voltage of CH3NH3PbI3 perovskite solar cells using electroluminescence and photovoltaic quantum efficiency spectra: the role of radiative and non-radiative recombination," *Advanced Energy Materials,* vol. 5, no. 3, p. 1400812, 2015.
[156] T. S. Sherkar, C. Momblona, L. Gil-Escrig, H. J. Bolink, and L. J. A. Koster, "Improving perovskite solar cells: insights from a validated device model," *Advanced Energy Materials,* vol. 7, no. 13, p. 1602432, 2017.

[157] Q. Zhuang *et al.*, "Tailoring multifunctional anion modifiers to modulate interfacial chemical interactions for efficient and stable perovskite solar cells," *Nano Energy,* p. 107747, 2022.
[158] Y. Luan *et al.*, "Dual-function interface engineering for efficient perovskite solar cells," *EcoMat,* vol. 3, no. 2, p. e12092, 2021.
[159] M. Wang, H. Wang, W. Li, X. Hu, K. Sun, and Z. Zang, "Defect passivation using ultrathin PTAA layers for efficient and stable perovskite solar cells with a high fill factor and eliminated hysteresis," *Journal of Materials Chemistry A,* vol. 7, no. 46, pp. 26421-26428, 2019.
[160] Y. Zhao *et al.*, "Inactive (PbI2) 2RbCl stabilizes perovskite films for efficient solar cells," *Science,* vol. 377, no. 6605, pp. 531-534, 2022.
[161] S. Mahjabin *et al.*, "Perceiving of defect tolerance in perovskite absorber layer for efficient perovskite solar cell," *IEEE Access,* vol. 8, pp. 106346-106353, 2020.
[162] B. Yang *et al.*, "Interfacial passivation engineering of perovskite solar cells with fill factor over 82% and outstanding operational stability on nip architecture," *ACS Energy Letters,* vol. 6, no. 11, pp. 3916-3923, 2021.
[163] H. Zhang *et al.*, "Synchronous Surface Reconstruction and Defect Passivation for High-Performance Inorganic Perovskite Solar Cells," *Small,* vol. 18, no. 33, p. 2202690, 2022.
[164] Q. Chen *et al.*, "Planar heterojunction perovskite solar cells via vapor-assisted solution process," *Journal of the American Chemical Society,* vol. 136, no. 2, pp. 622-625, 2014.
[165] Y. Raoui, H. Ez-Zahraouy, N. Tahiri, O. El Bounagui, S. Ahmad, and S. Kazim, "Performance analysis of MAPbI3 based perovskite solar cells employing diverse charge selective contacts: Simulation study," *Solar Energy,* vol. 193, pp. 948-955, 2019.
[166] C.-Y. Hsu *et al.*, "Experimental and theoretical study of improved mesoporous titanium dioxide perovskite solar cell: The impact of modification with graphene oxide," *Heliyon,* vol. 10, no. 4, 2024.
[167] I. M. De Los Santos *et al.*, "Optimization of CH3NH3PbI3 perovskite solar cells: A theoretical and experimental study," *Solar Energy,* vol. 199, pp. 198-205, 2020.
[168] K. R. Adhikari, S. Gurung, B. K. Bhattarai, and B. M. Soucase, "Comparative study on MAPbI3 based solar cells using different electron transporting materials," *physica status solidi (c),* vol. 13, no. 1, pp. 13-17, 2016.
[169] I. Ogundana and S. Foo, "Improving the morphology of the perovskite absorber layer in hybrid organic/inorganic halide perovskite MAPbI3 solar cells," *Journal of Solar Energy,* vol. 2017, no. 1, p. 8549847, 2017.
[170] S. Ghosh, S. Porwal, and T. Singh, "Investigation of the role of back contact work function for hole transporting layer free perovskite solar cells applications," *Optik,* vol. 256, p. 168749, 2022.
[171] J. W. Xiao, C. Shi, C. Zhou, D. Zhang, Y. Li, and Q. Chen, "Contact engineering: electrode materials for highly efficient and stable perovskite solar cells," *Solar RRL,* vol. 1, no. 9, p. 1700082, 2017.
[172] S. Gatz, T. Dullweber, and R. Brendel, "Evaluation of series resistance losses in screen-printed solar cells with local rear contacts," *IEEE Journal of Photovoltaics,* vol. 1, no. 1, pp. 37-42, 2011.
[173] E. Aydin, M. De Bastiani, and S. De Wolf, "Defect and contact passivation for perovskite solar cells," *Advanced Materials,* vol. 31, no. 25, p. 1900428, 2019.
[174] F. Gao, Y. Zhao, X. Zhang, and J. You, "Recent progresses on defect passivation toward efficient perovskite solar cells," *Advanced Energy Materials,* vol. 10, no. 13, p. 1902650, 2020.
[175] J. Kim, A. Ho-Baillie, and S. Huang, "Review of novel passivation techniques for efficient and stable perovskite solar cells," *Solar RRL,* vol. 3, no. 4, p. 1800302, 2019.
[176] Y. Cao *et al.*, "Defects passivation strategy for efficient and stable perovskite solar cells," *Advanced Materials Interfaces,* vol. 9, no. 21, p. 2200179, 2022.
[177] L. Fu, H. Li, L. Wang, R. Yin, B. Li, and L. Yin, "Defect passivation strategies in perovskites for an enhanced photovoltaic performance," *Energy & Environmental Science,* vol. 13, no. 11, pp. 4017-4056, 2020.
[178] D. Głowienka *et al.*, "Role of surface recombination in perovskite solar cells at the interface of HTL/CH3NH3PbI3," *Nano Energy,* vol. 67, p. 104186, 2020.
[179] N. Zarabinia, R. Rasuli, and E. Mohajerani, "New insight on the open-circuit voltage of perovskite solar cells: the role of defect-density distribution and electric field in the active layer," *International Journal of Energy Research,* vol. 45, no. 4, pp. 5190-5200, 2021.
[180] H. Huang *et al.*, "TiO2 surface oxygen vacancy passivation towards mitigated interfacial lattice distortion and efficient perovskite solar cell," *Applied Surface Science,* vol. 544, p. 148583, 2021.
[181] S. Tang *et al.*, "Simultaneous bulk and surface defect passivation for efficient inverted perovskite solar cells," *The Journal of Physical Chemistry Letters,* vol. 13, no. 23, pp. 5116-5122, 2022.
[182] F. Wang *et al.*, "Highly efficient and stable perovskite solar cells by interfacial engineering using solution-processed polymer layer," *The Journal of Physical Chemistry C,* vol. 121, no. 3, pp. 1562-1568, 2017.

[183] K. X. Steirer *et al.*, "Defect tolerance in methylammonium lead triiodide perovskite," *ACS Energy Letters,* vol. 1, no. 2, pp. 360-366, 2016.
[184] B. Hailegnaw, N. S. Sariciftci, and M. C. Scharber, "Impedance spectroscopy of perovskite solar cells: studying the dynamics of charge carriers before and after continuous operation," *physica status solidi (a),* vol. 217, no. 22, p. 2000291, 2020.
[185] S. Akin, N. Arora, S. M. Zakeeruddin, M. Grätzel, R. H. Friend, and M. I. Dar, "New strategies for defect passivation in high-efficiency perovskite solar cells," *Advanced Energy Materials,* vol. 10, no. 13, p. 1903090, 2020.
[186] Q. Wang, C. Bi, and J. Huang, "Doped hole transport layer for efficiency enhancement in planar heterojunction organolead trihalide perovskite solar cells," *Nano Energy,* vol. 15, pp. 275-280, 2015.
[187] B. Yang *et al.*, "Perovskite solar cells with near 100% internal quantum efficiency based on large single crystalline grains and vertical bulk heterojunctions," *Journal of the American Chemical Society,* vol. 137, no. 29, pp. 9210-9213, 2015.
[188] T. Duong *et al.*, "Rubidium multication perovskite with optimized bandgap for perovskite-silicon tandem with over 26% efficiency," *Advanced Energy Materials,* vol. 7, no. 14, p. 1700228, 2017.
[189] M. T. Hörantner *et al.*, "Shunt-blocking layers for semitransparent perovskite solar cells," *Advanced materials interfaces,* vol. 3, no. 10, p. 1500837, 2016.
[190] E. T. Hoke, D. J. Slotcavage, E. R. Dohner, A. R. Bowring, H. I. Karunadasa, and M. D. McGehee, "Reversible photo-induced trap formation in mixed-halide hybrid perovskites for photovoltaics," *Chemical Science,* vol. 6, no. 1, pp. 613-617, 2015.
[191] M. T. Islam *et al.*, "Investigation of non-Pb all-perovskite 4-T mechanically stacked and 2-T monolithic tandem solar devices utilizing SCAPS simulation," *SN Applied Sciences,* vol. 3, no. 4, pp. 1-12, 2021.
[192] R. RafieiRad and B. A. Ganji, "Efficiency Improvement of Perovskite Solar Cells by Utilizing $CuInS_2$ Thin Layer: Modeling and Numerical Study," *IEEE Transactions on Electron Devices,* vol. 68, no. 10, pp. 4997-5002, 2021.
[193] Y. Gan *et al.*, "Numerical investigation energy conversion performance of tin-based perovskite solar cells using cell capacitance simulator," *Energies,* vol. 13, no. 22, p. 5907, 2020.
[194] M. B. Johansson *et al.*, "Highly crystalline MAPbI3 perovskite grain formation by irreversible poor-solvent diffusion aggregation, for efficient solar cell fabrication," *Nano Energy,* vol. 78, p. 105346, 2020.
[195] A. S. Chouhan, N. P. Jasti, and S. Avasthi, "Effect of interface defect density on performance of perovskite solar cell: Correlation of simulation and experiment," *Materials Letters,* vol. 221, pp. 150-153, 2018.
[196] M. Feng, S. You, N. Cheng, and J. Du, "High quality perovskite film solar cell using methanol as additive with 19.5% power conversion efficiency," *Electrochimica Acta,* vol. 293, pp. 356-363, 2019.
[197] J. Lee and S. Baik, "Enhanced crystallinity of CH 3 NH 3 PbI 3 by the pre-coordination of PbI 2–DMSO powders for highly reproducible and efficient planar heterojunction perovskite solar cells," *RSC Advances,* vol. 8, no. 2, pp. 1005-1013, 2018.
[198] N. Mundhaas *et al.*, "Series resistance measurements of perovskite solar cells using Jsc–Voc measurements," *Solar RRL,* vol. 3, no. 4, p. 1800378, 2019.
[199] M. A. Green, "Solar cell fill factors: General graph and empirical expressions," *Solid State Electronics,* vol. 24, no. 8, pp. 788-789, 1981.
[200] M. Islam, A. Kumar, and A. Thakur, "Defect density control using an intrinsic layer to enhance conversion efficiency in an optimized SnS solar cell," *Journal of Electronic Materials,* vol. 50, no. 6, pp. 3603-3613, 2021.
[201] Y. M. Lee *et al.*, "Comprehensive understanding and controlling the defect structures: An effective approach for organic-inorganic hybrid perovskite-based solar-cell application," *Frontiers in Energy Research,* vol. 6, p. 128, 2018.
[202] S. Fonash, *Solar cell device physics*. Elsevier, 2012.
[203] Q. Deng, X. Han, Y. Gao, and G. Shao, "Remarkable optical red shift and extremely high optical absorption coefficient of V-Ga co-doped TiO2," *Journal of Applied Physics,* vol. 112, no. 1, p. 013523, 2012.
[204] F. Liu *et al.*, "Numerical simulation: toward the design of high-efficiency planar perovskite solar cells," *Applied Physics Letters,* vol. 104, no. 25, p. 253508, 2014.
[205] L. Lang, J.-H. Yang, H.-R. Liu, H. Xiang, and X. Gong, "First-principles study on the electronic and optical properties of cubic ABX3 halide perovskites," *Physics Letters A,* vol. 378, no. 3, pp. 290-293, 2014.
[206] J. Ryu, N. Noh, and Y. Jeon, "Chan Kim, WS Yang, J. Seo, and S. Il Seok," *Energy Environ. Sci,* vol. 7, p. 2614, 2014.

[207] F. Behrouznejad, S. Shahbazi, N. Taghavinia, H.-P. Wu, and E. W.-G. Diau, "A study on utilizing different metals as the back contact of CH 3 NH 3 PbI 3 perovskite solar cells," *Journal of Materials chemistry A,* vol. 4, no. 35, pp. 13488-13498, 2016.
[208] A. Morales-Acevedo, "Variable band-gap semiconductors as the basis of new solar cells," *Solar Energy,* vol. 83, no. 9, pp. 1466-1471, 2009.
[209] T. W. Jones *et al.*, "Lattice strain causes non-radiative losses in halide perovskites," *Energy & Environmental Science,* vol. 12, no. 2, pp. 596-606, 2019.
[210] S. D. Stranks, V. M. Burlakov, T. Leijtens, J. M. Ball, A. Goriely, and H. J. Snaith, "Recombination kinetics in organic-inorganic perovskites: excitons, free charge, and subgap states," *Physical Review Applied,* vol. 2, no. 3, p. 034007, 2014.
[211] E. M. Hutter, G. E. Eperon, S. D. Stranks, and T. J. Savenije, "Charge carriers in planar and meso-structured organic–inorganic perovskites: mobilities, lifetimes, and concentrations of trap states," *The journal of physical chemistry letters,* vol. 6, no. 15, pp. 3082-3090, 2015.
[212] Y. Yamada, M. Endo, A. Wakamiya, and Y. Kanemitsu, "Spontaneous defect annihilation in CH3NH3PbI3 thin films at room temperature revealed by time-resolved photoluminescence spectroscopy," *The journal of physical chemistry letters,* vol. 6, no. 3, pp. 482-486, 2015.
[213] Y. Lin *et al.*, "Metallic surface doping of metal halide perovskites," *Nature communications,* vol. 12, no. 1, pp. 1-8, 2021.
[214] J. Wang, W. Fu, S. Jariwala, I. Sinha, A. K.-Y. Jen, and D. S. Ginger, "Reducing surface recombination velocities at the electrical contacts will improve perovskite photovoltaics," *ACS Energy Letters,* vol. 4, no. 1, pp. 222-227, 2018.
[215] A. Kumar, "Efficiency enhancement of CZTS solar cells using structural engineering," *Superlattices and Microstructures,* vol. 153, p. 106872, 2021.
[216] Q. Liu *et al.*, "N and p-type properties in organo-metal halide perovskites studied by Seebeck effects," *Organic Electronics,* vol. 35, pp. 216-220, 2016.
[217] T. Shi, W.-J. Yin, and Y. Yan, "Predictions for p-type CH3NH3PbI3 perovskites," *The Journal of Physical Chemistry C,* vol. 118, no. 44, pp. 25350-25354, 2014.
[218] M. Islam *et al.*, "Investigation of non-Pb all-perovskite 4-T mechanically stacked and 2-T monolithic tandem solar devices utilizing SCAPS simulation," *SN Applied Sciences,* vol. 3, no. 4, pp. 1-12, 2021.
[219] W. Tress *et al.*, "Interpretation and evolution of open-circuit voltage, recombination, ideality factor and subgap defect states during reversible light-soaking and irreversible degradation of perovskite solar cells," *Energy & Environmental Science,* vol. 11, no. 1, pp. 151-165, 2018.
[220] T. S. Sherkar *et al.*, "Recombination in perovskite solar cells: significance of grain boundaries, interface traps, and defect ions," *ACS energy letters,* vol. 2, no. 5, pp. 1214-1222, 2017.
[221] Y. Shao *et al.*, "Grain boundary dominated ion migration in polycrystalline organic–inorganic halide perovskite films," *Energy & Environmental Science,* vol. 9, no. 5, pp. 1752-1759, 2016.
[222] X. Wu *et al.*, "Trap states in lead iodide perovskites," *Journal of the American Chemical Society,* vol. 137, no. 5, pp. 2089-2096, 2015.
[223] D. Luo, R. Su, W. Zhang, Q. Gong, and R. Zhu, "Minimizing non-radiative recombination losses in perovskite solar cells," *Nature Reviews Materials,* vol. 5, no. 1, pp. 44-60, 2020.
[224] D. Bi *et al.*, "Efficient luminescent solar cells based on tailored mixed-cation perovskites," *Science advances,* vol. 2, no. 1, p. e1501170, 2016.
[225] Y. Chen and H. Zhou, "Defects chemistry in high-efficiency and stable perovskite solar cells," *Journal of Applied Physics,* vol. 128, no. 6, p. 060903, 2020.
[226] W.-J. Yin, T. Shi, and Y. Yan, "Unusual defect physics in CH3NH3PbI3 perovskite solar cell absorber," *Applied Physics Letters,* vol. 104, no. 6, p. 063903, 2014.
[227] J. Kim, S.-H. Lee, J. H. Lee, and K.-H. Hong, "The role of intrinsic defects in methylammonium lead iodide perovskite," *The journal of physical chemistry letters,* vol. 5, no. 8, pp. 1312-1317, 2014.
[228] Q. Wang *et al.*, "Qualifying composition dependent p and n self-doping in CH3NH3PbI3," *Applied Physics Letters,* vol. 105, no. 16, p. 163508, 2014.
[229] B. Das, I. Aguilera, U. Rau, and T. Kirchartz, "Effect of Doping, Photodoping, and Bandgap Variation on the Performance of Perovskite Solar Cells," *Advanced Optical Materials,* vol. 10, no. 13, p. 2101947, 2022.
[230] R. Chen *et al.*, "Zinc ion as effective film morphology controller in perovskite solar cells," *Sustainable Energy & Fuels,* vol. 2, no. 5, pp. 1093-1100, 2018.
[231] N. K. Noel *et al.*, "Lead-free organic–inorganic tin halide perovskites for photovoltaic applications," *Energy & Environmental Science,* vol. 7, no. 9, pp. 3061-3068, 2014.
[232] J. Cao, S. X. Tao, P. A. Bobbert, C. P. Wong, and N. Zhao, "Interstitial occupancy by extrinsic alkali cations in perovskites and its impact on ion migration," *Advanced Materials,* vol. 30, no. 26, p. 1707350, 2018.

[233] J. T.-W. Wang *et al.*, "Efficient perovskite solar cells by metal ion doping," *Energy & Environmental Science,* vol. 9, no. 9, pp. 2892-2901, 2016.
[234] T. Zhou, M. Wang, Z. Zang, and L. Fang, "Stable dynamics performance and high efficiency of ABX3-type super-alkali perovskites first obtained by introducing H5O2 cation," *Advanced Energy Materials,* vol. 9, no. 29, p. 1900664, 2019.
[235] A. Kumar and A. D. Thakur, "Role of contact work function, back surface field, and conduction band offset in Cu2ZnSnS4 solar cell," *Japanese Journal of Applied Physics,* vol. 57, no. 8S3, p. 08RC05, 2018.
[236] S. Xiong *et al.*, "Surface charge-transfer doping for highly efficient perovskite solar cells," *Nano Energy,* vol. 79, p. 105505, 2021.
[237] N. K. Noel *et al.*, "Interfacial charge-transfer doping of metal halide perovskites for high performance photovoltaics," *Energy & environmental science,* vol. 12, no. 10, pp. 3063-3073, 2019.
[238] S. Pramchu, T. Cheiwchanchamnangij, Y. Laosiritaworn, and A. P. Jaroenjittichai, "Enhancing surface stabilization of CH3NH3PbI3 perovskite by Cl and Br doping: First-principles study," *Journal of Applied Physics,* vol. 125, no. 11, p. 115302, 2019.
[239] Y. Meng *et al.*, "Perovskite core–shell nanowire transistors: Interfacial transfer doping and surface passivation," *ACS nano,* vol. 14, no. 10, pp. 12749-12760, 2020.
[240] B. Das, I. Aguilera, U. Rau, and T. Kirchartz, "Effect of doping, photodoping and bandgap variation on the performance of perovskite solar cells," *arXiv preprint arXiv:2112.03445,* 2021.
[241] W. J. Yin, T. Shi, and Y. Yan, "Unique properties of halide perovskites as possible origins of the superior solar cell performance," *Advanced Materials,* vol. 26, no. 27, pp. 4653-4658, 2014.
[242] J. M. Ball and A. Petrozza, "Defects in perovskite-halides and their effects in solar cells," *Nature Energy,* vol. 1, no. 11, pp. 1-13, 2016.
[243] C. Ran, J. Xu, W. Gao, C. Huang, and S. Dou, "Defects in metal triiodide perovskite materials towards high-performance solar cells: origin, impact, characterization, and engineering," *Chemical Society Reviews,* vol. 47, no. 12, pp. 4581-4610, 2018.
[244] Q. A. Akkerman, G. Rainò, M. V. Kovalenko, and L. Manna, "Genesis, challenges and opportunities for colloidal lead halide perovskite nanocrystals," *Nature materials,* vol. 17, no. 5, pp. 394-405, 2018.
[245] S. Heo *et al.*, "Energy Environ. Sci. 10, 1128 (2017)," ed.
[246] Y. Shao, Y. Yuan, and J. Huang, "Correlation of energy disorder and open-circuit voltage in hybrid perovskite solar cells," *Nature Energy,* vol. 1, no. 1, pp. 1-6, 2016.
[247] L. K. Ono, S. Liu, and Y. Qi, "Reducing detrimental defects for high-performance metal halide perovskite solar cells," *Angewandte Chemie International Edition,* vol. 59, no. 17, pp. 6676-6698, 2020.
[248] J. Nelson, "Imperial College Press," *The physics of solar cells,* 2003.
[249] J. Simmons and G. Taylor, "Nonequilibrium steady-state statistics and associated effects for insulators and semiconductors containing an arbitrary distribution of traps," *Physical Review B,* vol. 4, no. 2, p. 502, 1971.
[250] G. N. Derry, M. E. Kern, and E. H. Worth, "Recommended values of clean metal surface work functions," *Journal of Vacuum Science & Technology A: Vacuum, Surfaces, and Films,* vol. 33, no. 6, p. 060801, 2015.
[251] A. Kumar and A. D. Thakur, "Role of contact work function, back surface field and conduction band offset in CZTS solar cell," *arXiv preprint arXiv:1807.02751,* 2018.
[252] A. Kumar and A. D. Thakur, "Improvement of efficiency in CZTSSe solar cell by using back surface field," in *IOP Conference Series: Materials Science and Engineering*, 2018, vol. 360, no. 1: IOP Publishing, p. 012027.
[253] M. K. Assadi, S. Bakhoda, R. Saidur, and H. Hanaei, "Recent progress in perovskite solar cells," *Renewable and Sustainable Energy Reviews,* vol. 81, pp. 2812-2822, 2018.
[254] T. J. Jacobsson *et al.*, "Exploration of the compositional space for mixed lead halogen perovskites for high efficiency solar cells," *Energy & Environmental Science,* vol. 9, no. 5, pp. 1706-1724, 2016.
[255] P. Fedeli *et al.*, "Influence of the synthetic procedures on the structural and optical properties of mixed-halide (Br, I) perovskite films," *The Journal of Physical Chemistry C,* vol. 119, no. 37, pp. 21304-21313, 2015.
[256] N. J. Jeon *et al.*, "Compositional engineering of perovskite materials for high-performance solar cells," *Nature,* vol. 517, no. 7535, pp. 476-480, 2015.
[257] L. Le, "Investigation on Stability of Cesium Lead Bromide quantum dots," 2016.
[258] J. H. Noh, S. H. Im, J. H. Heo, T. N. Mandal, and S. I. Seok, "Chemical management for colorful, efficient, and stable inorganic–organic hybrid nanostructured solar cells," *Nano letters,* vol. 13, no. 4, pp. 1764-1769, 2013.
[259] M. Zhu, G. Cao, and Z. Zhou, "Recent progress toward highly efficient tin-based perovskite (ASnX3) solar cells," *Nano Select,* vol. 2, no. 6, pp. 1023-1054, 2021.

[260] Y. Kawano, J. Chantana, T. Negami, T. Nishimura, A. Mavlonov, and T. Minemoto, "Theoretical impacts of single band gap grading of perovskite and valence band offset of perovskite/hole transport layer interface on its solar cell performances," *Solar Energy,* vol. 231, pp. 684-693, 2022.
[261] A. Kumar and A. D. Thakur, "Impurity photovoltaic and split spectrum for efficiency gain in Cu2ZnSnS4 solar cells," *Optik,* vol. 238, p. 166783, 2021.
[262] A. Morales-Acevedo, "A simple model of graded band-gap CuInGaSe2 solar cells," *Energy Procedia,* vol. 2, no. 1, pp. 169-176, 2010.
[263] A. Luque, "Will we exceed 50% efficiency in photovoltaics?," *Journal of applied physics,* vol. 110, no. 3, 2011.
[264] D. Ju *et al.*, "Tunable Band Gap and Long Carrier Recombination Lifetime of Stable Mixed CH3NH3Pb x Sn1–x Br3 Single Crystals," *Chemistry of Materials,* vol. 30, no. 5, pp. 1556-1565, 2018.
[265] O. Ergen *et al.*, "Graded bandgap perovskite solar cells," *Nature materials,* vol. 16, no. 5, pp. 522-525, 2017.
[266] G. M. Dalpian, X.-G. Zhao, L. Kazmerski, and A. Zunger, "Formation and composition-dependent properties of alloys of cubic halide perovskites," *Chemistry of Materials,* vol. 31, no. 7, pp. 2497-2506, 2019.
[267] Y. Liu *et al.*, "Two-inch-sized perovskite CH3NH3PbX3 (X= Cl, Br, I) crystals: growth and characterization," *Advanced materials,* vol. 27, no. 35, pp. 5176-5183, 2015.
[268] Y. Li *et al.*, "Bandgap tuning strategy by cations and halide ions of lead halide perovskites learned from machine learning," *RSC advances,* vol. 11, no. 26, pp. 15688-15694, 2021.
[269] S. A. Kulkarni, T. Baikie, P. P. Boix, N. Yantara, N. Mathews, and S. Mhaisalkar, "Band-gap tuning of lead halide perovskites using a sequential deposition process," *Journal of Materials Chemistry A,* vol. 2, no. 24, pp. 9221-9225, 2014.
[270] S. Karthick, S. Velumani, and J. Bouclé, "Experimental and SCAPS simulated formamidinium perovskite solar cells: A comparison of device performance," *Solar Energy,* vol. 205, pp. 349-357, 2020.
[271] A. Kumar, "Numerical modelling of ion-migration caused hysteresis in perovskite solar cells," *Optical and Quantum Electronics,* vol. 53, no. 4, p. 166, 2021.
[272] M. Tagreed, "Al-Saadi, Bushra H. Hussein, Alaa B. Hasan, AA Shehab, Study the Structural and Optical Properties of Cr doped SnO 2 Nanoparticles Synthesized by Sol-Gel Method," *Energy Procedia,* vol. 157, pp. 457-465, 2019.
[273] M. Bugelman, P. Nollet, and S. Degrave, "Modeling polycrystalline semiconductors solar cells," *Thin Solid Films,* vol. 3, pp. 89-94, 2000.
[274] M. Wiemer, V. Sabnis, and H. Yuen, "43.5% efficient lattice matched solar cells," in *High and Low Concentrator Systems for Solar Electric Applications VI*, 2011, vol. 8108: SPIE, pp. 29-33.
[275] T. K. Todorov *et al.*, "Ultrathin high band gap solar cells with improved efficiencies from the world's oldest photovoltaic material," *Nature communications,* vol. 8, no. 1, p. 682, 2017.
[276] Z. Hu, Z. Lin, J. Su, J. Zhang, J. Chang, and Y. Hao, "A review on energy band-gap engineering for perovskite photovoltaics," *Solar Rrl,* vol. 3, no. 12, p. 1900304, 2019.
[277] W. Shockley and H. Queisser, "Detailed balance limit of efficiency of p–n junction solar cells," in *Renewable energy*: Routledge, 2018, pp. Vol2_35-Vol2_54.
[278] Q. Cai *et al.*, "Improvement performance of planar perovskite solar cells by bulk and surface defect passivation," *ACS Sustainable Chemistry & Engineering,* vol. 9, no. 38, pp. 13001-13009, 2021.
[279] N. Parikh *et al.*, "Is machine learning redefining the perovskite solar cells?," *Journal of Energy Chemistry,* vol. 66, pp. 74-90, 2022.
[280] M.-H. Lee, "Robust random forest based non-fullerene organic solar cells efficiency prediction," *Organic Electronics,* vol. 76, p. 105465, 2020.
[281] Y. Zou, Y. Cui, H.-Y. Wang, Q. Cai, C. Mu, and J.-P. Zhang, "Highly efficient and stable 2D–3D perovskite solar cells fabricated by interfacial modification," *Nanotechnology,* vol. 30, no. 27, p. 275202, 2019.
[282] Y. Zhang *et al.*, "From 2D to 3D: a facile and effective procedure for fabrication of planar CH 3 NH 3 PbI 3 perovskite solar cells," *Journal of Materials Chemistry A,* vol. 6, no. 37, pp. 17867-17873, 2018.
[283] K. Amratisha *et al.*, "Layer-by-layer spray coating of a stacked perovskite absorber for perovskite solar cells with better performance and stability under a humid environment," *Optical Materials Express,* vol. 10, no. 7, pp. 1497-1508, 2020.
[284] R. Lu, Y. Liu, J. Zhang, D. Zhao, X. Guo, and C. Li, "Highly efficient (200) oriented MAPbI3 perovskite solar cells," *Chemical Engineering Journal,* vol. 433, p. 133845, 2022.
[285] S. Bhattarai, R. Pandey, J. Madan, D. Muchahary, and D. Gogoi, "A novel graded approach for improving the efficiency of Lead-Free perovskite solar cells," *Solar Energy,* vol. 244, pp. 255-263, 2022.

[286] A. Alsalme, M. F. Altowairqi, A. A. Alhamed, and R. A. Khan, "Optimization of Photovoltaic Performance of Pb-Free Perovskite Solar Cells via Numerical Simulation," *Molecules,* vol. 28, no. 1, p. 224, 2023.
[287] H. Zhu *et al.*, "Efficient and stable large bandgap MAPbBr3 perovskite solar cell attaining an open circuit voltage of 1.65 V," *ACS Energy Letters,* vol. 7, no. 3, pp. 1112-1119, 2022.
[288] B. Bachiri and K. Rahmoun, "Investigation and Improved Performance of MASnI 3 and MASnBr 3 Perovskites Solar Cells with Porous Silicon Layer," in *Advanced Computational Techniques for Renewable Energy Systems*: Springer, 2023, pp. 826-832.
[289] C. Lu *et al.*, "Efficient inverted CsPbI3 perovskite solar cells fabricated in common air," *Chemical Engineering Journal,* vol. 452, p. 139495, 2023.
[290] B. K. Ravidas, M. K. Roy, and D. P. Samajdar, "Investigation of photovoltaic performance of lead-free CsSnI3-based perovskite solar cell with different hole transport layers: First Principle Calculations and SCAPS-1D Analysis," *Solar Energy,* vol. 249, pp. 163-173, 2023.
[291] K. Deepthi Jayan, "Design and Comparative Performance Analysis of High-Efficiency Lead-Based and Lead-Free Perovskite Solar Cells," *physica status solidi (a),* vol. 219, no. 7, p. 2100606, 2022.
[292] J. Liu *et al.*, "Growing high-quality CsPbBr 3 by using porous CsPb 2 Br 5 as an intermediate: a promising light absorber in carbon-based perovskite solar cells," *Sustainable Energy & Fuels,* vol. 3, no. 1, pp. 184-194, 2019.
[293] T. Miyasaka, A. Kulkarni, G. M. Kim, S. Öz, and A. K. Jena, "Perovskite solar cells: can we go organic-free, lead-free, and dopant-free?," *Advanced Energy Materials,* vol. 10, no. 13, p. 1902500, 2020.
[294] S. H. Kareem, M. H. Elewi, A. M. Naji, D. S. Ahmed, and M. K. Mohammed, "Efficient and stable pure α-phase FAPbI3 perovskite solar cells with a dual engineering strategy: additive and dimensional engineering approaches," *Chemical Engineering Journal,* vol. 443, p. 136469, 2022.
[295] X. Meng *et al.*, "Highly reproducible and efficient FASnI3 perovskite solar cells fabricated with volatilizable reducing solvent," *The Journal of Physical Chemistry Letters,* vol. 11, no. 8, pp. 2965-2971, 2020.
[296] A. Raj, M. Kumar, H. Bherwani, A. Gupta, and A. Anshul, "Evidence of improved power conversion efficiency in lead-free CsGeI3 based perovskite solar cell heterostructure via scaps simulation," *Journal of Vacuum Science & Technology B,* vol. 39, no. 1, 2021.
[297] M. Mehrabian, E. N. Afshar, and S. A. Yousefzadeh, "Simulating the thickness effect of the graphene oxide layer in CsPbBr3-based solar cells," *Materials Research Express,* vol. 8, no. 3, p. 035509, 2021.
[298] S. Tao *et al.*, "Absolute energy level positions in tin-and lead-based halide perovskites," *Nature communications,* vol. 10, no. 1, p. 2560, 2019.
[299] J. M. Frost, "Calculating polaron mobility in halide perovskites," *Physical Review B,* vol. 96, no. 19, p. 195202, 2017.
[300] D. Stanić *et al.*, "Simulation and Optimization of FAPbI3 Perovskite Solar Cells with a BaTiO3 Layer for Efficiency Enhancement," *Materials,* vol. 15, no. 20, p. 7310, 2022.
[301] A. Tara, V. Bharti, S. Sharma, and R. Gupta, "Device simulation of FASnI3 based perovskite solar cell with Zn (O0. 3, S0. 7) as electron transport layer using SCAPS-1D," *Optical Materials,* vol. 119, p. 111362, 2021.
[302] X. Sun, R. Asadpour, W. Nie, A. D. Mohite, and M. A. Alam, "A physics-based analytical model for perovskite solar cells," *IEEE Journal of Photovoltaics,* vol. 5, no. 5, pp. 1389-1394, 2015.
[303] C. She, Q. Huang, C. Chen, Y. Jiang, Z. Fan, and J. Gao, "Machine learning-guided search for high-efficiency perovskite solar cells with doped electron transport layers," *Journal of Materials Chemistry A,* vol. 9, no. 44, pp. 25168-25177, 2021.
[304] J. Im, S. Lee, T.-W. Ko, H. W. Kim, Y. Hyon, and H. Chang, "Identifying Pb-free perovskites for solar cells by machine learning," *npj Computational Materials,* vol. 5, no. 1, p. 37, 2019.
[305] F. Häse, L. M. Roch, P. Friederich, and A. Aspuru-Guzik, "Designing and understanding light-harvesting devices with machine learning," *Nature Communications,* vol. 11, no. 1, p. 4587, 2020.
[306] A. O. Oliynyk and J. M. Buriak, "Virtual issue on machine-learning discoveries in materials science," vol. 31, ed: ACS Publications, 2019, pp. 8243-8247.
[307] A. Mahmood and J.-L. Wang, "Machine learning for high performance organic solar cells: current scenario and future prospects," *Energy & environmental science,* vol. 14, no. 1, pp. 90-105, 2021.
[308] M.-H. Lee, "Performance and matching band structure analysis of tandem organic solar cells using machine learning approaches," *Energy Technology,* vol. 8, no. 3, p. 1900974, 2020.
[309] R. Prasanna *et al.*, "Band gap tuning via lattice contraction and octahedral tilting in perovskite materials for photovoltaics," *Journal of the American Chemical Society,* vol. 139, no. 32, pp. 11117-11124, 2017.
[310] M. Pandey, K. W. Jacobsen, and K. S. Thygesen, "Band gap tuning and defect tolerance of atomically thin two-dimensional organic–inorganic halide perovskites," *The journal of physical chemistry letters,* vol. 7, no. 21, pp. 4346-4352, 2016.

[311] L.-B. Huang *et al.*, "Interface engineering of perovskite solar cells with multifunctional polymer interlayer toward improved performance and stability," *Journal of Power Sources,* vol. 378, pp. 483-490, 2018.
[312] J. Peng, Y. Chen, K. Zheng, T. Pullerits, and Z. Liang, "Insights into charge carrier dynamics in organo-metal halide perovskites: from neat films to solar cells," *Chemical Society Reviews,* vol. 46, no. 19, pp. 5714-5729, 2017.
[313] W. Zhang *et al.*, "Highly efficient perovskite solar cells with tunable structural color," *Nano letters,* vol. 15, no. 3, pp. 1698-1702, 2015.
[314] K. B. Lohmann *et al.*, "Control over crystal size in vapor deposited metal-halide perovskite films," *ACS energy letters,* vol. 5, no. 3, pp. 710-717, 2020.
[315] J. Lim *et al.*, "Elucidating the long-range charge carrier mobility in metal halide perovskite thin films," *Energy & Environmental Science,* vol. 12, no. 1, pp. 169-176, 2019.
[316] A. D. Wright, R. L. Milot, G. E. Eperon, H. J. Snaith, M. B. Johnston, and L. M. Herz, "Band-tail recombination in hybrid lead iodide perovskite," *Advanced Functional Materials,* vol. 27, no. 29, p. 1700860, 2017.
[317] D. P. Almond and C. R. Bowen, "An explanation of the photoinduced giant dielectric constant of lead halide perovskite solar cells," *The journal of physical chemistry letters,* vol. 6, no. 9, pp. 1736-1740, 2015.
[318] E. J. Juarez-Perez *et al.*, "Photoinduced giant dielectric constant in lead halide perovskite solar cells," *The journal of physical chemistry letters,* vol. 5, no. 13, pp. 2390-2394, 2014.
[319] T. Ouslimane, L. Et-Taya, L. Elmaimouni, and A. Benami, "Impact of absorber layer thickness, defect density, and operating temperature on the performance of MAPbI3 solar cells based on ZnO electron transporting material," *Heliyon,* vol. 7, no. 3, 2021.
[320] H. MallaHasan and Ö. Onay, "Investigation of the effect of different factors on the performance of several perovskite solar cells: a simulation study by SCAPS," *European Journal of Engineering Science and Technology,* vol. 5, no. 1, pp. 20-38, 2022.
[321] B. Turedi, V. Yeddu, X. Zheng, D. Y. Kim, O. M. Bakr, and M. I. Saidaminov, "Perovskite single-crystal solar cells: going forward," *ACS Energy Letters,* vol. 6, no. 2, pp. 631-642, 2021.
[322] C. Duan and J. Dai, "Improved pin MAPbI 3 perovskite solar cells via the interface defect density suppression by PEABr passivation," *Optics Express,* vol. 30, no. 21, pp. 38104-38114, 2022.
[323] M. T. Islam *et al.*, "Investigation of CsSn 0.5 Ge 0.5 I 3-on-Si tandem solar device utilizing SCAPS simulation," *IEEE Transactions on Electron Devices,* vol. 68, no. 2, pp. 618-625, 2021.
[324] A. Slami, M. Bouchaour, and L. Merad, "Numerical study of based perovskite solar cells by SCAPS-1D," *Int. J. Energy Environ,* vol. 3, pp. 17-21, 2019.
[325] A. K. Singh, M. S. Chauhan, S. P. Patel, R. S. Singh, and V. K. Singh, "MAPbI3-on-CuInSe2 two-terminal monolithically integrated and four-terminal mechanically stacked tandem solar cells: A Theoretical Investigation Using SCAPS-1D," *Results in Optics,* vol. 10, p. 100358, 2023.
[326] A. K. Singh, S. Srivastava, A. Mahapatra, J. K. Baral, and B. Pradhan, "Performance optimization of lead free-MASnI3 based solar cell with 27% efficiency by numerical simulation," *Optical Materials,* vol. 117, p. 111193, 2021.
[327] A. K. Al-Mousoi *et al.*, "Simulation and analysis of lead-free perovskite solar cells incorporating cerium oxide as electron transporting layer," *RSC advances,* vol. 12, no. 50, pp. 32365-32373, 2022.
[328] H. Sabbah, J. Arayro, and R. Mezher, "Numerical simulation and optimization of highly stable and efficient lead-free perovskite FA1− xCsxSnI3-based solar cells using SCAPS," *Materials,* vol. 15, no. 14, p. 4761, 2022.
[329] S. Srivastava, A. K. Singh, P. Kumar, and B. Pradhan, "Comparative performance analysis of lead-free perovskites solar cells by numerical simulation," *Journal of Applied Physics,* vol. 131, no. 17, 2022.
[330] P. K. Patel, "Device simulation of highly efficient eco-friendly CH3NH3SnI3 perovskite solar cell," *Scientific reports,* vol. 11, no. 1, p. 3082, 2021.
[331] S. Huang, Z. Rui, D. Chi, and D. Bao, "Influence of defect states on the performances of planar tin halide perovskite solar cells," *Journal of Semiconductors,* vol. 40, no. 3, p. 032201, 2019.
[332] J. Alzubi, A. Nayyar, and A. Kumar, "Machine learning from theory to algorithms: an overview," in *Journal of physics: conference series*, 2018, vol. 1142: IOP Publishing, p. 012012.
[333] A. L. Boulesteix, S. Janitza, J. Kruppa, and I. R. König, "Overview of random forest methodology and practical guidance with emphasis on computational biology and bioinformatics," *Wiley Interdisciplinary Reviews: Data Mining and Knowledge Discovery,* vol. 2, no. 6, pp. 493-507, 2012.
[334] A. M. Mahmood, N. Satuluri, and M. R. Kuppa, "An Overview of recent and traditional decision tree classifiers in machine learning," *International Journal of Research and Reviews in Ad Hoc Networks,* vol. 1, no. 1, p. 2011, 2011.

[335] M. Schonlau and R. Y. Zou, "The random forest algorithm for statistical learning," *The Stata Journal,* vol. 20, no. 1, pp. 3-29, 2020.
[336] D. Baron, "Machine learning in astronomy: A practical overview," *arXiv preprint arXiv:1904.07248,* 2019.

Publications

Journals:

1. Prasanna, J.L., Goel, E and Kumar, A., “Efficient modeling of double absorber layered structure in perovskite solar cells using machine learning techniques”, **Physica Scripta**, 2023, doi: 10.1088/1402-4896/acf535 **[SCI]**
2. Prasanna, J.L., Goel, E and Kumar, A., " Numerical investigation of MAPbI3 perovskite solar cells for performance limiting parameters," **Optical and Quantum Electronics**, 2023, doi: 10.1007/s11082-023-04876-9. **[SCI]**
3. Prasanna, J.L., Goel, E., Kumar, A and Kumar, A., “Reduced interfacial recombination in perovskite solar cells by structural engineering simulation,” **Journal of Optics**., November 2022, doi: 10.1088/2040-8986/ac95a8. **[SCI]**
4. Prasanna, J.L., Goel, E., Kumar, A and Kumar, A., “Review of nanomaterials impact on improving the performance of dye-sensitized and perovskite solar cells,” **Optical and Quantum Electronics**., November. 2022, doi: 10.1007/s11082-022-04147-z. **[SCI]**
5. Prasanna, J.L., Goel, E., Kumar, A., Laref, Amel., Santhosh, Chella., Ranjan, Pranay., and Kumar, A., “Bandgap graded perovskite solar cell for above 30% efficiency,” **Optik**, November. 2022, doi: 10.1016/j.ijleo.2022.169891. **[SCI]**
6. Prasanna, J.L., Goel, E and Kumar, A., “Defect Density-Dependent Dynamics of Double absorber layered Perovskite solar cell”, **IEEE Access [“Under Review”]**

Conferences:

1. Prasanna, J.L., Goel, E., Kumar, A and Kumar, A., “Computational Study of Double Absorber layer Perovskite Solar Cell Devices,” 2022 **IEEE Indian Conf. INDICON** 2022, doi: 10.1109/INDICON56171.2022.10039776.
2. Prasanna, J.L., Goel, E., Kumar, A and Kumar, A., “Computational Study of Perovskite/Perovskite Lead-free Tandem Solar Cell Devices,” 2022 **IEEE Indian Conf. ISES** 2022, doi: 10.1109/iSES54909.2022.00059.